



EDITE - ED 130

Doctorat ParisTech

THÈSE

pour obtenir le grade de docteur délivré par

TELECOM ParisTech

Spécialité « Signal et Images »

présentée et soutenue publiquement par

Yafei XING

le 27 Jan 2015

Méthodes de compression

pour les données holographiques numériques

Directeur de thèse : **Frédéric DUFAUX**

Co-encadrement de la thèse : **Béatrice PESQUET-POPESCU**

Jury

Mme. Christine Guillemot, INRIA

M. Peter Schelkens, VUB

M. Benoît Macq, UCL

M. Joel Jung, Orange

M. Mounir Kaaniche, Univ. Paris 13

M. Frédéric Dufaux, Télécom ParisTech

Mme. Béatrice Pesquet-Popescu, Télécom ParisTech

Rapporteur

Rapporteur

Examineur

Examineur

Invité

Directeur de thèse

Directrice de thèse

TELECOM ParisTech

école de l'Institut Mines-Télécom - membre de ParisTech

Acknowledgements

First of all, I would like to thank Dr. Frédéric Dufaux to give me this precious opportunity of doing a PhD in France. I am most grateful to the advising of my two supervisors Prof. Béatrice Pesquet-Popescu, Dr. Frédéric Dufaux. With their patience, encouragement and trust, my PhD career is very fruitful. It is a great honor to have worked with them.

This thesis would not have been completed without the kind helps from Mr. Mounir Kaaniche. He worked with me a lot during the important time. I am impressed by his patience, ability of inspiration, motivation of research and knowledge. Also, the feedback from my thesis committee members Prof. Christine Guillemot and Prof. Peter Schelkens is very precious. I would like to thank them for their constructive comments on my work.

I would also like to express my thanks to my colleagues at the Signal and Image processing Department of Telecom ParisTech (TSI, Télécom ParisTech). They are "weird" but preciously nice friends. Their company made my PhD life wonderful.

Finally, a special gratitude goes to Mr. Pierrick Milhorat, for his endless support and encouragement in my hard time. Moreover, without the support of my parents, I would never have been able to experience all these. I greatly acknowledge them for their tremendous support all the years of my study.

Abstract

Digital holography plays a crucial role in recent three dimensional imaging as well as microscopic applications. As a result, huge amounts of storage capacity will be involved for this kind of data. Therefore, it becomes necessary to develop efficient hologram compression schemes for storage and transmission purposes, which is the aim of this thesis. Particularly, the objective is the compression of digital holographic data obtained from phase-shifting interferometry.

Unlike conventional approaches which encode certain representation of phase-shifting holographic data independently, the proposed work first studies the possible representations of phase-shifting holographic data and analyzes the redundancies in each representation. A new representation, referred to as shifted distance information, is selected as the compression target. Then, a vector lifting schemes based compression method is proposed to jointly encode this data. We also show the benefits that can be drawn from improving a separable decomposition to a non-separable one within such joint coding schemes.

On the other hand, we also investigate the performance of mainstream video coding schemes and the effects of some parameters which are used in the design of different compression schemes. This may allow us to build content adaptive methods. More precisely, the prediction filter length used in vector lifting schemes or the transform unit size used in video coding schemes can be optimized according to different holographic structures. However, the optimization method will be the future work of this thesis.

Contents

Acknowledgements	ii
Abstract	iii
1 Introduction	1
1.1 Thesis Context	1
1.2 Objectives and Contributions	2
1.3 Thesis Outline	4
1.4 Publications	5
2 Main Concepts in Digital Holography	7
2.1 Introduction	7
2.2 Holography	8
2.2.1 Hologram Acquisition	8
2.2.2 Hologram Reconstruction	9
2.3 Digital Holography	10
2.3.1 Numerical Reconstruction	11
2.3.2 Computer Generated Hologram	13
2.4 Phase-shifting Digital Holography	15
2.4.1 Motivation	16
2.4.2 Principle of Phase-shifting digital holography	17
2.5 Computer Generated Phase-shifting Hologram	18
2.5.1 Ray tracing method	18
2.5.2 Fresnel Hologram	23
2.6 Conclusion	24

3	Representation and Compression of Digital Holographic Data	26
3.1	Introduction	26
3.2	Representation of Interference Patterns	27
3.2.1	Motivation and introduction	27
3.2.2	Intensity based representation	27
3.2.3	Complex amplitude based representation	28
3.3	Compression of Digital Holographic Data: State-of-the-art	31
3.3.1	Basic compression tools	31
3.3.2	Overview of compression schemes for digital holographic data	34
3.3.3	Limitations in the state-of-the-art	38
3.4	Basic Analysis of Different Representation Data	39
3.4.1	Motivation	39
3.4.2	Analyzing tools: quantization	39
3.4.3	Comparative study	40
3.5	Conclusion	46
4	Separable Vector Lifting Scheme on Digital Phase-shifting Holographic Data	51
4.1	Introduction	51
4.2	Vector Lifting Scheme	51
4.2.1	Introduction: Lifting schemes	51
4.2.2	Basic concepts of lifting schemes	52
4.2.3	VLS decomposition	53
4.3	Proposed Compression Scheme based on VLS	56
4.3.1	Motivation	56
4.3.2	Applied procedures	56
4.4	Experimental results	59
4.4.1	Comparative study	59
4.4.2	Evaluations and discussions	60
4.5	Conclusion	62
5	Non Separable Vector Lifting Scheme on Digital Phase-shifting Holographic Data	70
5.1	Introduction	70

5.2	Proposed compression scheme based on NS-VLS	71
5.2.1	Motivation	71
5.2.2	Principle of NS-VLS decomposition	71
5.3	Design of prediction and update filters	75
5.3.1	Optimization techniques	75
5.3.2	Definition of the spatial supports	76
5.3.3	Transmission cost of the filter coefficients	78
5.4	Experimental results	78
5.4.1	Comparative study	78
5.4.2	Results of different encoding schemes	79
5.4.3	Results of NS-VLS with different filter lengths	80
5.5	Conclusion	82
6	Investigation of Compressing Phase-shifting Holographic Data by Video Coding Schemes	89
6.1	Introduction	89
6.2	Investigation of AVC and HEVC on hologram sequences generated from image sequences	90
6.2.1	Overview of compression schemes for digital holographic sequences	90
6.2.2	Generation and processing of phase-shifting digital hologram sequence	91
6.2.3	Experimental results	92
6.3	Investigation of AVC and HEVC on shifted distance data obtained from still images	95
6.3.1	Motivation	95
6.3.2	Experimental results	95
6.4	Conclusion	97
	Conclusions and Future Work	101
	Bibliography	104
	Appendix A Résumé en français	111
A.1	Introduction: Contexte de la thèse	111
A.2	Etat de l'art	113
A.3	Contributions	115

A.3.1	Analyse de base de données de représentation différente	115
A.3.2	Schéma de lifting vectoriel séparable	120
A.3.3	Schéma de lifting vectoriel non séparable	123
A.3.4	Etude de Compression des données holographiques à déphasage à l'aide de schémas de codage vidéo	127
A.4	Conclusion et perspectives	128

List of Tables

2.1	Parameters of CGPSH	24
3.1	Parameters of CGPSH	41
3.2	PSNR obtained from quantizing amplitude-phase information of “Luigi” object by USQ	43
3.3	PSNR obtained from quantizing real-imaginary information of “Luigi” object by USQ	43
3.4	PSNR obtained from quantizing shifted distance information of “Luigi” object by USQ	43
3.5	PSNR obtained from ASQ and USQ on amplitude-phase (Am,Ph) and D1, D2 information of three objects	45
3.6	PSNR obtained from LBG-VQ on amplitude-phase (Am,Ph) and shifted distance information of three objects	46
4.1	Entropy measure on $D^{(2)}$, $D^{(2)} - D^{(1)}$ and $D^{(2)} - Pred(D^{(1)}, D^{(2)})$ of “Luigi-1”, “Luigi-2” and “Girl” objects	57
4.2	Entropy measure of three different compression schemes on “Luigi-1”, “Luigi-2” and “Girl” objects	61
4.3	Entropy measure of three different compression schemes on “Luigi-1”, “Luigi-2” and “Girl” objects	62
5.1	The average PSNR, SSIM and bitrate saving gains of NS-VLS(2,2) with respect to SEP-VLS(2,2) using Bjontegaard metric.	80
5.2	The average PSNR, SSIM and bitrate saving gains of NS-VLS(12,2) with respect to NS-VLS(2,2) using Bjontegaard metric.	81

5.3	The average PSNR, SSIM and bitrate saving gains of NS-VLS(20,2) with respect to NS-VLS(2,2) using Bjontegaard metric.	82
6.1	Bitrate (kbps), PSNR (dB) and MSSIM obtained by AVC	92
6.2	Bitrate (kbps), PSNR (dB) and MSSIM obtained by HEVC	93
6.3	Bjontegaard Metrics for each sequence	95

List of Figures

2.1	Hologram recording setup: BS: Beam splitter.	8
2.2	Hologram reconstruction.	9
2.3	Coordinate geometry of hologram reconstruction.	10
2.4	Model example of 3D objects: (a) polygonal mesh model, and (b) raster graphic model.	15
2.5	Setup for phase-shifting digital holography: PZT, piezoelectric transducer mirror.	16
2.6	Example of zero order image in the reconstruction: (a) recorded object, (b) reconstructed object with zero order image	17
2.7	Coordinate system of wave propagation	18
2.8	Object images	19
2.9	CGPSH with $\phi = \pi$ (contrast adjusted)	20
2.10	Reconstructed intensity in the real image plane $d = 2m$	21
2.11	Reconstructed intensity in the real image plane $d = 2.1m$	22
2.12	Reconstructed amplitude in the virtual image plane $d = 2.1m$	23
2.13	Example of CGPSH by Fresnel transform: (a) original object of “bunny”; (b) A Fresnel hologram of “bunny” with reference wave $\phi = 0$; (c) A Fresnel hologram of “bunny” with reference wave $\phi = \frac{\pi}{2}$; (d) A Fresnel hologram of “bunny” with reference wave $\phi = \pi$	25
3.1	Example of two difference data $D^{(1)}$ and $D^{(2)}$ for the “Bunny” object.	28
3.2	Example of real part and imaginary part distributions for the “Bunny” object.	29
3.3	Example of amplitude-phase distributions for the “Bunny” object.	30
3.4	Generic compression scheme	31

3.5	Quantization process: Q represents the encoding or quantization stage and Q^{-1} represents the decoding or inverse quantization stage	32
3.6	Schematic of JPEG 2000	34
3.7	Testing objects: “Luigi”, “Girl” and “Bunny”.	42
3.8	Corresponding figure of Table. 3.2	43
3.9	Corresponding figure of Table. 3.3	43
3.10	Corresponding figure of Table. 3.4	43
3.11	Probability distribution of different representations.	44
3.12	Reconstructed images at bit levels of 2, 3 and 4 from amplitude-phase information (left column) and shifted distance information (right column) of “Luigi” object	48
3.13	Reconstructed images at bit levels of 2, 3 and 4 from amplitude-phase information (left column) and shifted distance information (right column) of “Girl” object	49
3.14	Reconstructed images at bit levels of 2, 3 and 4 from amplitude-phase information (left column) and shifted distance information (right column) of “Bunny” object	50
4.1	Generic lifting structure.	52
4.2	Principle of the VLS decomposition.	54
4.3	3D test objects	60
4.4	Rate-distortion performance of the different hologram compression schemes applied on $D^{(1)}$ and $D^{(2)}$ for the objects: (a) “Bunny-1”, (b) “Bunny-2”, (c) “Girl”.	64
4.5	Rate-distortion performance of the different hologram compression schemes applied on $D^{(1)}$ and $D^{(2)}$ for the objects: (a) “Luigi-1”, (b) “Luigi-2”, (c) “Teapot”.	65
4.6	Reconstructed “Bunny-1” object at 0.5 bpp using: (a) Independent-I, (b) Standard-I, (c) VLS-I.	66
4.7	Reconstructed “Bunny-1” object at 0.7 bpp using: (a) Independent-I, (b) Standard-I, (c) VLS-I.	66
4.8	Reconstructed “Luigi-1” object at 0.6 bpp using: (a) Independent-I, (b) Standard-I, (c) VLS-I.	67

4.9	Reconstructed “Luigi-1” object at 0.9 bpp using: (a) Independent-I, (b) Standard-I, (c) VLS-I.	67
4.10	Rate-distortion performance of the different hologram compression schemes applied on $I^{(1)}$ and $I^{(2)}$ for the objects: (a) “Bunny-1”, (b) “Bunny-2”, (c) “Girl”.	68
4.11	Rate-distortion performance of the different hologram compression schemes applied on $I^{(1)}$ and $I^{(2)}$ for the objects: (a) “Luigi-1”, (b) “Luigi-2”, (c) “Teapot”.	69
5.1	Proposed NS-VLS decomposition structure.	72
5.2	Rate-distortion performance of the different hologram compression schemes for the objects: (a) “Luigi-1”, (b) “Luigi-2”, (c) “Bunny-1”, (d) “Bunny-2”, (e) “Girl”, (f) “Teapot”.	83
5.3	Reconstructed “Luigi-1” object at 0.9 bpp using: (a)SEP-VLS(2,2), (b) NS-VLS(2,2).	84
5.4	Reconstructed “Bunny-1” object at 0.5 bpp (upper) and 0.7 bpp (lower) using: (a)SEP–VLS, (b) NS–VLS.	84
5.5	Rate-distortion performance of the proposed NS-VLS with different prediction filter lengths for the objects: (a) “Luigi-1”, (b) “Luigi-2”, (c) “Bunny-1”, (d) “Bunny-2”, (e) “Girl”, (f) “Teapot”.	85
5.6	Rate-distortion performance of the proposed NS-VLS with different prediction filter lengths for the objects: (a) “Bunny-1”, (b) “Bunny-2”. An example where the overhead coding cost of the filter coefficients is not taken into account.	86
5.7	Reconstructed “Girl” objects at 0.6 bpp by using (b) NS-VLS(2,2), (c) NS-VLS(6,2), (d) NS-VLS(12,2), (e) NS-VLS(20,2), (f) NS-VLS(32,2).	87
5.8	Reconstructed “Teapot” objects at 0.8 bpp by using: (b) NS-VLS(2,2), (c) NS-VLS(6,2), (d) NS-VLS(12,2), (e) NS-VLS(20,2), (f) NS-VLS(32,2).	88
6.1	Over scheme for digital holographic video processing	91
6.2	Some basic encoder configurations for (a)JM and (b) HM	93
6.3	Rate-distortion performance of AVC and HEVC for the objects: (a) “Bunny”, (b) “CONE”	94

6.4	Reconstructed “Bunny” object by: (a)AVC and (b) HEVC with different QP parameters.	98
6.5	Reconstructed “CONE” object by: (a)AVC and (b) HEVC with different QP parameters.	99
6.6	(a)PSNR and (b) SSIM measurement obtained from compressing shifted distance information of “Luigi” object by different video coding schemes . . .	100
A.1	Setup for phase-shifting digital holography: PZT, piezoelectric transducer mirror.	116
A.2	Exemple de données de distance décalé $D^{(1)}$ and $D^{(2)}$	117
A.3	Exemple de partie réelle et imaginaire distributions partielles.	118
A.4	Exemple de distributions d’amplitude et phase.	119
A.5	Principe du schéma de lifting vectoriel séparable.	120
A.6	Principe de la structure d’analyse du schéma de lifting vectoriel non séparable.	123
A.7	Over scheme for digital holographic video processing	128

Chapter 1

Introduction

1.1 Thesis Context

Holography has been considered as the ultimate three dimensional (3D) technology since invented by Gabor in 1948 [1]. Flawless 3D images of recorded objects can be optically reconstructed with all depth cues by illuminating holograms using the reference wave in the recording procedure. On the other hand, with the growing expectation of three-dimensional experience, interest for 3D video is steadily gaining momentum. Current 3D techniques are mainly based on stereoscopic and multiview representations, which only exploit limited depth cues. Furthermore, they lack inherent accommodation-vergence conflict, which may induce headache, nausea or visual fatigue. Consequently, holography can be considered as a perfect 3D technology. In addition, giving the advantages of CCD sensor and computer calculation, digital holography (DH) [2,3] and computer generated holography (CGH) [4,5], have also been developed with promising features.

However, either traditional holography or DH, demands a very stable system for the optical recording holograms of real 3D objects. The laser beam illuminating the objects must be highly coherent with the reference laser beam. These constraints, together with the long time cost of film exposure and spatial resolution constraints, limit the application of optical holography. An alternative solution is using CGH, which can simulate the whole recording and reconstruction procedure by computer. No matter how the digital holograms are obtained, the fact that digital holographic data represents a huge amount of information makes a significant technological hurdle for its practical use. To overcome this problem, the use of compression techniques is mandatory for storage and transmission of digital

holographic data.

Nevertheless, compression methods should be developed on the basis of compression targets. In other words, a suitable representation of the interference patterns is required for a certain compression method. Directly, intensity of the interference patterns, which is also defined as hologram, should be the first option. Unfortunately, the reconstruction quality from one single hologram is badly influenced by the zero-order image or twin image due to the lost of phase information, which leads to the application of phase-shifting digital holography (PSDH) [6].

In PSDH, the complex amplitude of object wave at hologram plane can be fully reconstructed by recording at least three digital holograms. By phase-shifting algorithm, some other representations of the interference pattern consisting of two sets of data, instead of three sets of intensity information, can be extracted. In this case, other representations are more suitable as compression objects than three sets of intensity data. On the other hand, comparing with single in-line/off-axis hologram, the extra set of phase-shifting holographic data makes the compression of digital holographic data even harsher. Thus, in this thesis, the attention is more specifically focused on the representation and compression of digital holographic data based on PSDH.

1.2 Objectives and Contributions

As previously mentioned, there are two main objectives in this thesis. One is to investigate and find a suitable representation of the interference pattern. Then based on this representation, the other objective is to investigate and develop efficient compression methods.

More precisely, in order to focus on the compression part, digital holograms, which are generated in single view point, are simply used. It could be adapted to the application of compressing full parallax digital hologram. Different representations of the interference patterns are obtained, consisting of at least two sets of digital holographic data. Consequently, using inter compression on such a representation could be more efficient if significant redundancy exists in that representation. So the redundancy analysis is conducted firstly to find a suitable representation. With that, inter compression methods mainly based on vector lifting scheme (VLS) [7] are adapted and investigated in this thesis.

A detailed list of the main contributions is as follows:

- First, due to the physical limitations of recording holograms, a simple Fresnel Transform based scheme for CGH is constructed and subsequently applied throughout our work. Based on it, the general understanding of compressing phase-shifting digital holograms is exploited by standard still image compression methods JPEG [8] and JPEG 2000 [9] on the representation of intensity. Moreover, the comparative study of compressing phase-shifting digital hologram sequences is also investigated by standard digital video compression methods: Advanced Video Coding (AVC) [10] and High Efficiency Video Coding (HEVC) [11].
- Then, the redundancy analysis of two main representations of digital holographic data is conducted. One representation is the amplitude and phase information obtained by phase-shifting algorithm. Then we propose a second representation, referred to as shifted distance information. This representation appears to have more visual redundant structures than amplitude and phase information. Based on that, the further analysis by vector quantization based on Linde-Buzo-Gray (VQ-LBG) algorithm is conducted to investigate redundancies in different representations.
- Based on the conclusion that there are more redundancies existing in shifted distance information, we propose a new joint multiscale separable decomposition based on vector lifting scheme and adapt the coding scheme to the contents of shifted distance information. Unlike most of other work using intra compression methods in state-of-the-art, the proposed method encodes two sets of holographic data jointly. Also, different from standard joint coding schemes, instead of generating a residual image, two compact multiresolution representations of two input images are encoded. The advantages of the proposed scheme are further exploited by comparing with an independent encoding scheme, i.e. JPEG 2000, and standard joint coding scheme.
- Next, a non separable decomposition based on VLS (NS-VLS) [12] is designed based on the observation that the shifted distance information presents rather isotropic structures. The decomposition in the separable VLS is handled simply by applying a one dimensional (1D)-VLS along the lines, then along the columns of the holographic data. Therefore it is not optimal to cope with the shifted distance data. In contrast, NS-VLS is much better adapted to the isotropic data structure. In addition, the performance of the decomposition with different prediction filter lengths is also studied for two aspects: the special repetitive circular structure of the holographic data and

exploiting the inter redundancies through the inter-prediction stage.

- Finally, a performance comparison is carried out among inter/intra modes of HEVC with different sizes of coding units and separable VLS.

1.3 Thesis Outline

This thesis is organized as follows.

In Chapter 2, the main concepts of DH including CGH and PSDH are introduced. The basic optical principles of hologram recording are first explained, which includes the theories of diffraction and interference. Based on it, the recording configuration and optical reconstruction are then formally described, which are the basis of numerical modeling. The concepts of PSDH are reviewed at the end.

In Chapter 3, an overview of state-of-the-art digital holographic data coding schemes is given. To this end, the concept of different representations of interference patterns is first reminded. The state-of-the-art work is then reviewed according to different representations. In addition, a comparative study by using scalar and vector quantization methods is introduced to exploit redundancies in different representations of phase-shifting holographic data. The performance is analyzed in terms of reconstruction quality and bitrate.

In Chapter 4, we propose a new joint multiscale separable decomposition of phase-shifting holographic data based on VLS. The motivation is first addressed by considering the specificity of VLS, followed with the description of the main principle of VLS. A statistical analysis of the proposed scheme is conducted in terms of reconstruction quality and bitrate.

In Chapter 5, a non separable decomposition based on VLS is proposed considering the isotropic structures of shifted distance data. The decomposition details of NS-VLS are first explained along with the specific design of the prediction and update filters. A statistical analysis of the proposed scheme is also conducted in terms of reconstruction quality and bitrate.

In Chapter 6, a preliminary investigation of compressing phase-shifting digital holographic data is provided by applying video coding schemes. First, phase-shifting hologram sequences are compressed by inter mode of AVC and HEVC. The basic scheme of applying AVC and HEVC to hologram sequences is described, followed by the reported comparison results in terms of reconstruction quality and bitrate. Then, the influence of one parameter used in HEVC- the size of the transform unit (TU)-is mainly investigated on shifted

distance information.

At the end, some relevant conclusions and possible future work of this research are addressed in Chapter 7.

1.4 Publications

The following publications are the direct outcome of this research work.

International Journal papers

- Y. Xing, M. Kaaniche, B. Pesquet-Popescu, and F. Dufaux, “Vector lifting scheme for phase-shifting holographic data compression,” *Optical Engineering, Special issue on Practical Holography: New Procedures, Materials, and Applications*, 53(11), 2014.
- Y. Xing, M. Kaaniche, B. Pesquet-Popescu, and F. Dufaux, “Adaptive non separable vector lifting scheme for digital holographic data compression,” *Applied Optics*, Vol. 54, Issue 1, pp. A98-A109 (2015)

International Conference papers

- Y. Xing, B. Pesquet-Popescu, and F. Dufaux, “Comparative study of scalar and vector quantization on different phase-shifting digital holographic data representations,” *3DTV-Conference: The True Vision - Capture, Transmission and Display of 3D Video (3DTV-CON), 2014*, pp.1,4, 2-4 July, Budapest, Hungary ,2014.
- Y. Xing, B. Pesquet-Popescu, and F. Dufaux, “Vector quantization for computer generated phase-shifting holograms,” *Signals, Systems and Computers, 2013 Asilomar Conference on* , pp.709,713, 3-6 Nov, Pacific Grove, CA, 2013.
- Y. Xing, B. Pesquet-Popescu, and F. Dufaux, “Compression of computer generated phase-shifting hologram sequence using AVC and HEVC,” in *Proc. SPIE, Applications of Digital Image Processing XXXVI*, 8856, San Diego, California, USA, 2013.
- Y. Xing, B. Pesquet-Popescu, and F. Dufaux, “Compression of computer generated hologram based on phase-shifting algorithm,” in *European Workshop on visual information Processing*, 172-177, Paris, 2013.

Book

- Y. Xing, B. Pesquet-Popescu, and F. Dufaux, “Digital Holographic Data Representation and Compression,” *Academic Press* (in preparation, to appear 2015)

Chapter 2

Main Concepts in Digital Holography

2.1 Introduction

The word **Holography**, meaning “total recording”, gives a direct understanding of the significant technique invented by Dennis Gabor [1, 13]. With holography, the full information about both the amplitude and phase of the diffracted or scattered object waves can be totally recorded. Consequently, the object image can be reconstructed with all depth cues. With the development of recording devices and computers, DH makes possible the optical recording through digital processing [14–16]. One step further, with CGH the whole procedure is performed numerically [17–19]. As a result, holography is more practical and easier to be processed. Moreover, the design of PSDH gives a good solution for suppressing the bothering images in the reconstruction procedure [20, 21].

Note that even though the term **Digital Holography** has been commonly accepted for the method of optical recording to numerical processing, CGH is included in DH within the scope of this thesis. In both cases, the processing is based on digital holograms and they share similar recording principles which are derived by the same mathematical models.

This chapter outlines the main aspects relevant for understanding the imaging principles of DH. The fundamental principles of holography are first introduced in Section 2.2 with the description of hologram acquisition and its reconstruction. In Section 2.3, numerical reconstruction with different mathematical approximations for DH are provided. Section 2.4 describes the motivation and the algorithm for applying PSDH. Based on the introduced

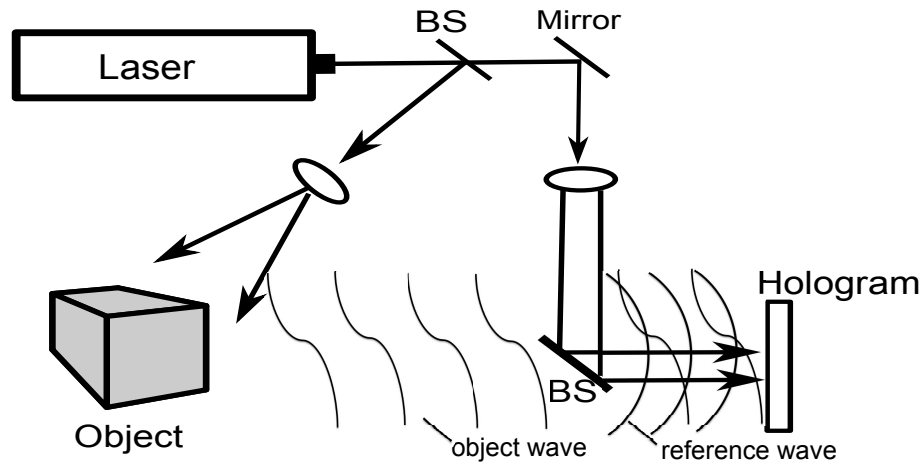


Figure 2.1: Hologram recording setup: BS: Beam splitter.

concepts, two examples of computer generated phase-shifting hologram (CGPSH) are given in Section 2.5. Finally, a summary is provided in Section 2.6.

2.2 Holography

The traditional hologram is defined by the interference patterns between the diffracted or scattered wave from the objects (object wave) and another coherent wave (reference wave). The real or virtual image of recorded objects can be observed by illuminating from different sides of the hologram with same reference wave. The principles are explained in the following.

2.2.1 Hologram Acquisition

Fig. 2.1 depicts a typical geometry for recording holograms. A laser beam is split into two paths by a beam splitter, one of which illuminating the object forms the diffracted or scattered object wave and the other one, which is the reference wave, is led to interfere with the object wave at the hologram plane.

Interference

In accordance with Maxwell equations, the complex amplitude of the object wave U_O

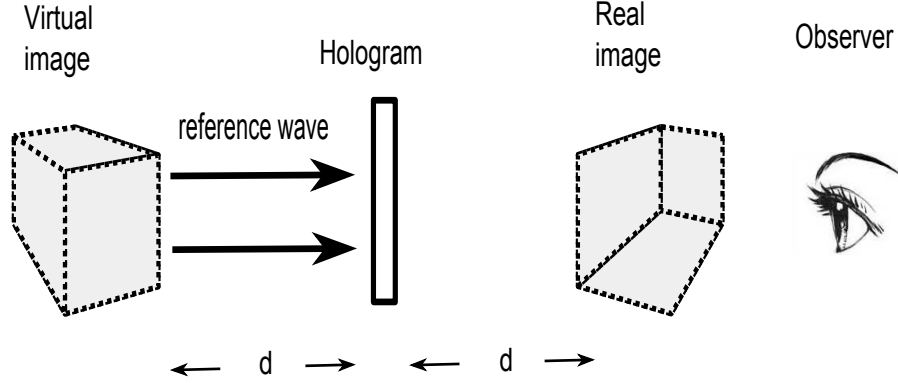


Figure 2.2: Hologram reconstruction.

and the reference wave U_R at the hologram plane can be represented by

$$\begin{aligned} U_O &= A_O e^{i\varphi_O}, \\ U_R &= A_R e^{i\varphi_R}, \end{aligned} \quad (2.1)$$

respectively, where (A_O, φ_O) and (A_R, φ_R) are the amplitude and phase distribution pairs of the object wave and reference wave, respectively. The resultant intensity of the interference patterns is expressed as

$$\begin{aligned} I_H &= |U_R + U_O|^2 \\ &= |A_R|^2 + |A_O|^2 + 2|A_R||A_O|\cos(\varphi_R - \varphi_O). \end{aligned} \quad (2.2)$$

Thus the amplitude and phase information of the object wave is recorded.

2.2.2 Hologram Reconstruction

The object image is optically reconstructed as illustrated in Fig. 2.2 by illuminating the hologram. The virtual image appears at the position of the original object while the real image is also observed at a distance d from the hologram but in the opposition direction. If the hologram is illuminated by the conjugate reference wave, the real and virtual images can be observed in the opposite positions of where they are observed in Fig. 2.2. The coordinate geometry of Fig. 2.2 can be explained in Fig. 2.3.

The reconstruction procedure is considered as a diffraction phenomenon which happens when a light wave (the reference wave) illuminates an aperture (the hologram) in an opaque

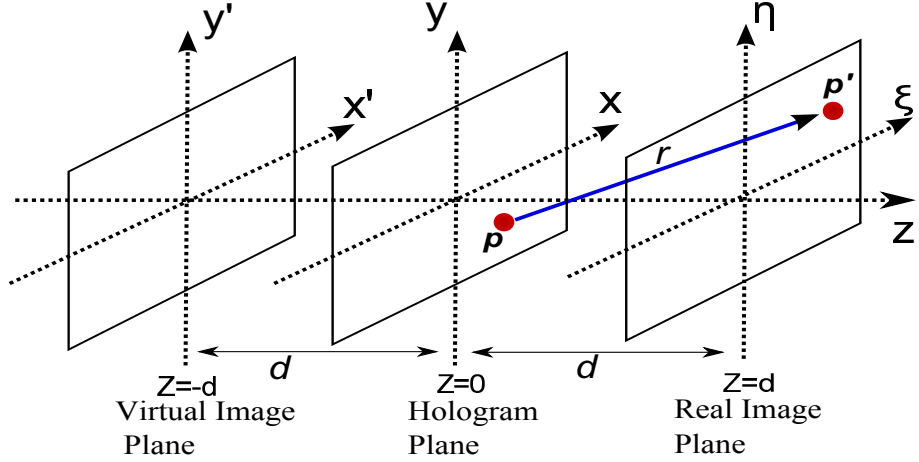


Figure 2.3: Coordinate geometry of hologram reconstruction.

plane. It can be explained by scalar diffraction theory if two conditions are met [22] (1) the diffracting aperture must be large compared with the wavelength, and (2) the diffracting fields must not be observed too close to the aperture. Suppose that the reference wave is perpendicular to the hologram plane as shown in Fig. 2.2. The resulting diffraction can be described by the Fresnel-Kirchhoff integral under the scalar diffraction theory [22]:

$$U(\xi, \eta) = -\frac{i}{\lambda} \int_{-\infty}^{+\infty} \int_{-\infty}^{+\infty} I_H(x, y) U_R(x, y) \frac{e^{ikr}}{r} dx dy \quad (2.3)$$

with

$$r = \sqrt{(x - \xi)^2 + (y - \eta)^2 + d^2} \quad (2.4)$$

where $U(\xi, \eta)$ is the complex amplitude of the real image, λ is the wavelength, $I_H(x, y)$ is the hologram function in the hologram plane ($Z = 0$) at point P with coordinate (x, y) , r is the distance between point P in the hologram plane to point P' with coordinate (ξ, η) in the real image plane ($Z = d$) and d is the distance between the two planes (real image and hologram plane, resp. virtual image and hologram plane).

2.3 Digital Holography

With the development of electronic recording devices, a Charged Coupled Device (CCD) is more commonly used to capture digital holograms than traditional photographic films. On the other hand, specially in CGH, the advanced computations by a computer nowadays make

possible the whole holographic processing fully released from strict physical limitations. The utilization of virtual objects not existing in the real life is even yielding more expectations on holography. But no matter how the digital holograms are obtained, DH definitely facilitates the processing of holograms.

In the following of this section, the basic digital processing of digital holograms, named numerical reconstruction, is first described with Fresnel and Fraunhofer approximations. Then the main concepts of CGH are introduced.

2.3.1 Numerical Reconstruction

Certain approximations have been introduced to scalar diffraction theory, which reduce the diffraction pattern calculations to simpler mathematical manipulations. In this thesis, the commonly used Fresnel and Fraunhofer approximations are introduced to deal with wave propagation. Based on these approximations, numerical processing can be easily conducted.

Reconstruction by Fresnel approximation

The Fresnel approximation is obtained by approximations for distance r introduced in Eq. (2.4). The expression can be expanded to a Taylor series:

$$r = d + \frac{(x - \xi)^2}{2d} + \frac{(y - \eta)^2}{2d} - \frac{1}{8} \frac{[(x - \xi)^2 + (y - \eta)^2]^2}{d^3} + \dots \quad (2.5)$$

Then it is approximated to

$$r \approx d + \frac{(x - \xi)^2}{2d} + \frac{(y - \eta)^2}{2d}, \quad (2.6)$$

if the fourth term is very small compared to the wavelength:

$$\frac{1}{8} \frac{[(x - \xi)^2 + (y - \eta)^2]^2}{d^3} \ll \lambda. \quad (2.7)$$

Moreover, given the acceptable small error introduced by dropping all terms in approximated r but d for the r appearing in the denominator and substituting Eq. (2.6) into r in the exponent in Eq. (2.3), the resulting complex amplitude of the real image

is expressed as follows:

$$U(\xi, \eta) = -\frac{i}{\lambda d} e^{ikd} \int_{-\infty}^{+\infty} \int_{-\infty}^{+\infty} I_H(x, y) U_R(x, y) e^{\frac{ik}{2d}[(x-\xi)^2 + (y-\eta)^2]} dx dy \quad (2.8)$$

Factor the multiplications $e^{\frac{ik}{2d}(\xi^2 + \eta^2)}$ in the exponential term outside the integral, yielding

$$U(\xi, \eta) = -\frac{i}{\lambda d} e^{ik(d + \frac{\xi^2 + \eta^2}{2d})} \int_{-\infty}^{+\infty} \int_{-\infty}^{+\infty} I_H(x, y) U_R(x, y) e^{\frac{ik}{2d}(x^2 + y^2)} e^{-\frac{ik}{d}(x\xi + y\eta)} dx dy, \quad (2.9)$$

where the mathematical similarity with the Fourier Transform can be easily recognized. This formulation is named Fresnel approximation, where the observer is in the near field of the aperture.

Reconstruction by Fraunhofer approximation

The stronger Fraunhofer approximation is in addition to the Fresnel approximation. If the condition

$$d \gg \frac{k(x^2 + y^2)}{2} \quad (2.10)$$

is satisfied, then the quadratic phase factor $e^{\frac{ik}{2d}(x^2 + y^2)}$ under the integral sign in Eq. (2.9) is approximately equal to unity. The reconstructed complex amplitude of the real image is consequently substituted by

$$U(\xi, \eta) = -\frac{i}{\lambda d} e^{ik(d + \frac{\xi^2 + \eta^2}{2d})} \int_{-\infty}^{+\infty} \int_{-\infty}^{+\infty} I_H(x, y) U_R(x, y) e^{-\frac{ik}{d}(x\xi + y\eta)} dx dy, \quad (2.11)$$

which can also be obtained similarly from the Fourier transform of the aperture distribution $I_H(x, y) U_R(x, y)$. It is named Fraunhofer approximation where the observer is located in the far field of the aperture.

Reconstruction digitization

For digitizing the reconstruction formulas, the following substitutions are introduced:

$$\nu = \frac{\xi}{\lambda d}; \mu = \frac{\eta}{\lambda d} \quad (2.12)$$

The Fresnel approximation becomes

$$U(\nu, \mu) = -\frac{i}{\lambda d} e^{ikd} e^{i\pi\lambda d(\nu^2 + \mu^2)} \int_{-\infty}^{+\infty} \int_{-\infty}^{+\infty} I_H(x, y) U_R(x, y) e^{\frac{ik}{2d}(x^2 + y^2)} e^{-i2\pi(x\nu + y\mu)} dx dy, \quad (2.13)$$

which shows that the Fresnel approximation is the Fourier transformation of the term $I_H(x, y) U_R(x, y) e^{\frac{ik}{2d}(x^2 + y^2)}$.

Suppose that the hologram function $I_H(x, y)$ is sampled on a rectangular raster of $N \times N$ points, Δx and Δy are the distances between neighboring pixels in horizontal and vertical direction. In accordance with the theory of Fourier transform, re-substitute

$$\Delta\xi = \frac{\lambda d}{N\Delta x}; \Delta\eta = \frac{\lambda d}{N\Delta y} \quad (2.14)$$

to Eq. (2.13), the discrete Fresnel transform is calculated as follows:

$$U(k, l) = -\frac{i}{\lambda d} \exp(ikd) \exp\left[i\pi\lambda d\left(\frac{k^2}{N^2\Delta x^2} + \frac{l^2}{N^2\Delta y^2}\right)\right] \\ \times \sum_{m=0}^{N-1} \sum_{n=0}^{N-1} I_H(m, n) U_R(m, n) \exp\left[\frac{ik}{2d}(m^2\Delta x^2 + n^2\Delta y^2)\right] \exp\left[-i2\pi\left(\frac{km}{N} + \frac{ln}{N}\right)\right] \quad (2.15)$$

where $k = 1, 2, \dots, N$ and $l = 1, 2, \dots, N$ are the discrete dimensions' indices of the reconstructed image plane, $n = 1, 2, \dots, N$ and $m = 1, 2, \dots, N$ are the discrete dimensions' indices of the hologram plane. Similarly, one can obtain the discrete Fraunhofer approximation:

$$U(k, l) = -\frac{i}{\lambda d} \exp(ikd) \exp\left[i\pi\lambda d\left(\frac{k^2}{N^2\Delta x^2} + \frac{l^2}{N^2\Delta y^2}\right)\right] \\ \times \sum_{m=0}^{N-1} \sum_{n=0}^{N-1} I_H(m, n) U_R(m, n) \exp\left[-i2\pi\left(\frac{km}{N} + \frac{ln}{N}\right)\right]. \quad (2.16)$$

2.3.2 Computer Generated Hologram

CGH is a technique allowing to create digital holograms by mathematical means of calculating the optical wave propagation. It is released from physical recording limitations by approximating the wave propagation with less complexity, as light propagation is affected by

several phenomenas like reflection, refraction, interference, diffraction and so on. Normally, the basic stages for synthesizing a computer generated hologram can be listed as follows:

1. Selecting 3D objects from real or virtual life and designing a mathematical model of the objects;
2. Defining the geometry of wave propagation from objects to the hologram plane;
3. Computing the object wave at the hologram plane by carrying out the discrete transform on the representation of wave propagation
4. Computing intensities of the interference patterns.

Object models

In CGH, both real objects and virtual objects can be chosen for recording. For real objects, it has been achieved to calculate holograms using their multi-view projection images captured by a camera array. However, a big advantage of CGH is that it is able to create holograms of virtual objects. To this end, CGH is very promising in 3D technology.

There are two types of object models commonly used: (1) “geometrical models” which represent objects as compositions of elementary diffracting elements, e.g., polygonal mesh model, as illustrated in Fig. 2.4(a), and (2) “bitmap models” or “raster graphic models” which represent objects as 2D or 3D arrays of points, as shown in Fig. 2.4(b). The elementary components of each model specify the amplitude and phase distribution of the object wave when the object is illuminated. However, they can share the same mathematical calculation principle by computing the superposition of elemental holograms.

Geometry of wave propagation

The geometry of wave propagation is related to the chosen objects. Currently, ray-oriented methods [18] and wave-oriented methods [23] are two mainstream methods. Generally speaking, ray-oriented methods are commonly applied on virtual objects consisting of source points by tracing the ray from a source point to a sampling point on the hologram. These methods are also called point-based methods. Wave-oriented methods are mainly for “objects” represented by elemental surfaces, such as interpolated projection images or multi-view images of real or virtual objects [24, 25],

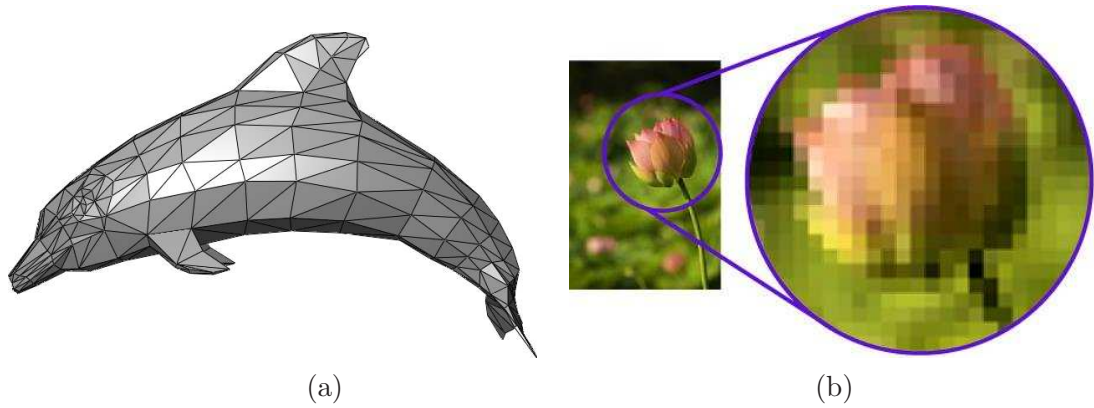


Figure 2.4: Model example of 3D objects: (a) polygonal mesh model, and (b) raster graphic model.

virtual objects constituted of polygonal meshes [26, 27] and so on. Each surface can be regarded as a surface source light, accordingly a “surface” field is formed. The field of an object, which is the sum of the sub “surface” fields, then propagates to the hologram plane.

Practical discrete transform

For the geometries of wave propagation mentioned above, the wave propagation can be calculated based on the diffraction theory which is explained in Sec. 2.3.1. Consequently, the Fresnel approximation or Fraunhofer approximation could be applied if the source points or the fields are sampled in planes parallel to the hologram plane. Both approximations work by taking the discrete Fourier transform.

2.4 Phase-shifting Digital Holography

Phase shifting interferometry was proposed to improve reconstruction quality in DH. The complex amplitude in the hologram plane can be completely calculated, thus the complex amplitude in any plane, e.g., the virtual or real image plane, is able to be reconstructed by using the Fresnel-Kirchhoff diffraction formulation. The object image can consequently be reconstructed without bothering images. In this section, the motivation of applying PSDH and the principle of phase-shifting algorithm are described.

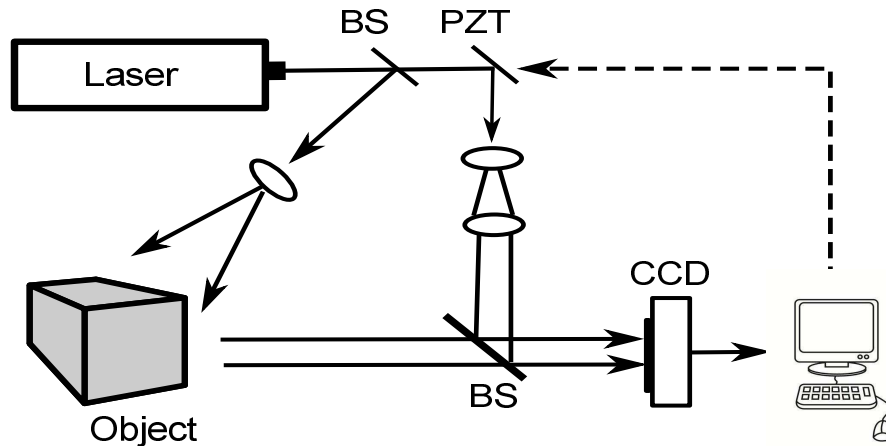


Figure 2.5: Setup for phase-shifting digital holography: PZT, piezoelectric transducer mirror.

2.4.1 Motivation

For the holograms recorded by the geometry shown in Fig. 2.1, a bright square would appear in the center of the reconstructed image and cover the object image as shown in Fig. 2.6(b) (an example from Ref. [22], Fig. 2.6(a) depicts the image of the recorded object). It is called zero order image due to the undiffracted reconstruction wave which is expressed by the first two terms in Eq. (2.2). That kind of setup is called in-line setup, which means there is no offset angle between the object wave and the reference wave when they are introduced to the hologram plane. On the other hand, with the same geometry, the real image and virtual image are located in one line as shown in Fig. 2.2. Normally only one image is visible in the reconstruction, however, in some cases, e.g., if the recording distance is very short, the other out of focus image (twin image) might disturb the reconstructed one. For these two reasons, Leith and Upatnieks proposed an off-axis setup where a tilted reference wave is introduced [28], by which the reconstructed image is spatially separated from the zero order image and twin image. However, this setup requires much higher spatial frequencies on the CCD than in-line setup. Meanwhile, in order to alleviate this problem, Yamaguchi *et al* [6] proposed PSDH based on in-line setup.

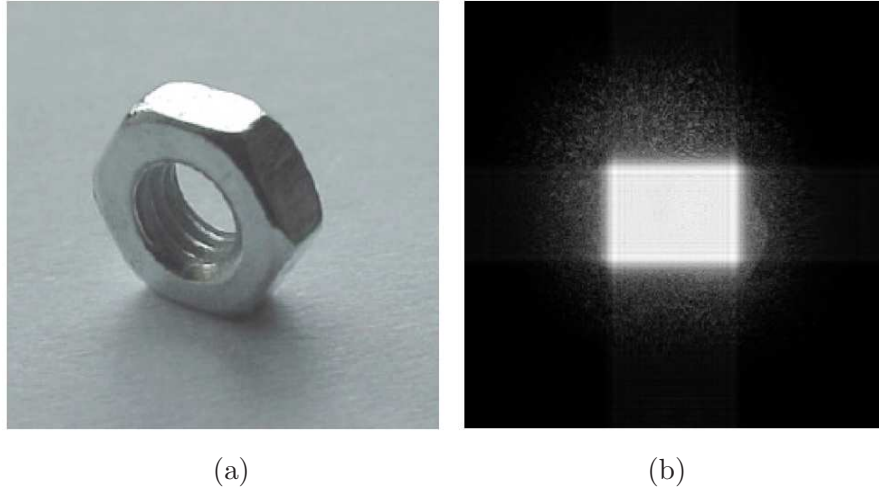


Figure 2.6: Example of zero order image in the reconstruction: (a) recorded object, (b) reconstructed object with zero order image

2.4.2 Principle of Phase-shifting digital holography

The basic geometry of PSDH is illustrated in Fig. A.1. Similar to the classic setup shown in Fig. 2.1, one branch of the split laser beam illuminates the object and interferes with the other beam (the reference beam) at the CCD device. The reference beam is reflected at the piezoelectric transducer (PZT) mirror that phase modulates the beam. By shifting a constant phase to the reference beam, different holograms are obtained to derive the complex amplitude of the object wave.

In the simplest application of PSDH, the initial phase ϕ of the reference wave is zero and changes by $\frac{\pi}{2}$ at each step, the intensity of the interference patterns expressed in Eq. (2.2) is then updated as

$$I_H(x, y; \phi) = |U_R(x, y; \phi) + U_O(x, y)|^2, \quad \phi \in \{0, \frac{\pi}{2}, \pi\} \quad (2.17)$$

The complex amplitude of the object wavefront at the hologram plane can be calculated directly using recorded holograms in the case of a three-step algorithm:

$$\widehat{U}_O(x, y) = \frac{1 - \imath}{4U_R^*} \{I_H(x, y; 0) - I_H(x, y; \frac{\pi}{2}) + \imath[I_H(x, y; \frac{\pi}{2}) - I_H(x, y; \pi)]\} \quad (2.18)$$

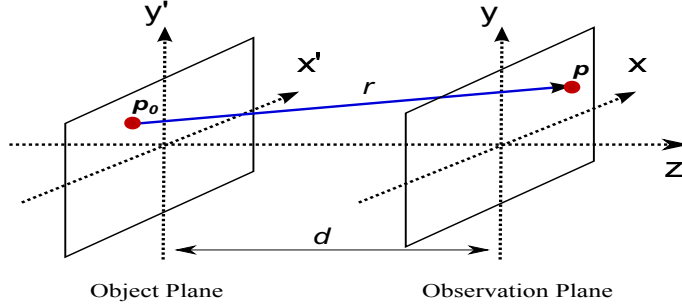


Figure 2.7: Coordinate system of wave propagation

where U_R^* is the conjugate of the reference wave with $\phi = 0$. Then the complex amplitude in the image plane, $I_H(x, y)$, can be reconstructed by using the Fresnel-Kirchhoff diffraction formulation.

2.5 Computer Generated Phase-shifting Hologram

In this section, two examples of generating phase-shifting holograms are described based on ray tracing method and Fresnel transform. Since the generation of high quality holograms is not the main concern in this thesis, a simple application of Fresnel Hologram is derived from ray tracing method using “bitmap models” of small size virtual objects. Meanwhile, for the sake of simplicity, some physical phenomena for reconstructing 3D images, such as occlusions, transparency and so on, are not considered in this thesis. Thus objects represented by bitmap images are selected as the object model, also considering the convenience of model acquisition.

2.5.1 Ray tracing method

Given the coordinate system of wave propagation by ray tracing method in Fig. 2.7, each point P_0 on the object surface can be considered as a source of the spherical wave which is represented as

$$E(P_0) = A_0 e^{i\varphi_0} \quad (2.19)$$

where $E(P_0)$ is the complex amplitude with the real-valued amplitude A_0 and the initial phase φ_0 at point P_0 . With the design of $\varphi_0 = 0$, the wave representation at point P in

space can be approximated by satisfying the scalar Helmholtz equations as

$$E(P) = A_0 \frac{e^{ikr}}{r} \quad (2.20)$$

where $E(P)$ is the complex amplitude of the wave at point P generated by point P_0 , and r is the distance between point P to point P_0 . Then, the object wave at the hologram plane is represented by

$$U(x, y) = \int_{-\infty}^{+\infty} \int_{-\infty}^{+\infty} A(x', y') \frac{e^{ikr}}{r} dx' dy'. \quad (2.21)$$

In the discrete form, we obtain

$$U(m, n) = \sum_{k=0}^{N-1} \sum_{l=0}^{N-1} A(k, l) \frac{e^{ikr_{mk, nl}}}{r} \quad (2.22)$$

$k = 1, 2, \dots, N$ and $l = 1, 2, \dots, N$ are the discrete dimensions' indices of the object plane, $n = 1, 2, \dots, N$ and $m = 1, 2, \dots, N$ are the discrete dimensions' indices of the hologram plane, $r_{mk, nl}$ is the distance between the pixel (m, n) in the hologram plane and the pixel (k, l) in the object plane. The intensity of the phase-shifting holograms can be expressed by

$$I_H(m, n; \phi) = |U_R(\phi) + U(m, n)|^2 \quad (2.23)$$

Example

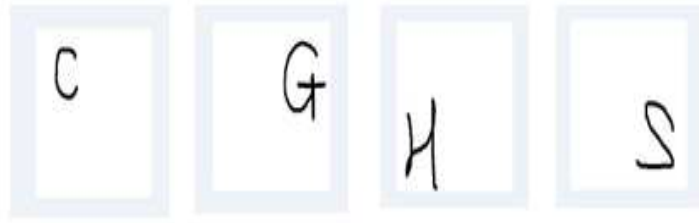


Figure 2.8: Object images

A simple example is given in the following. The virtual 3D objects are defined by four different gray images shown in Fig. 2.8 with four different letters (C, G, H, S, respectively) in the depths of $d = 2m, 2.1m, 2.2m, 2.3m$. The pixels with higher gray value are counted

as the object points emanating for calculating CGPSHs with original amplitude assigned as one, others are set to 0. The wavelength is set to 630nm and its initial phase is 0. The hologram plane is 600×600 pixels with a spacing of $1/600$ in between each adjacent pixel. In Fig. 2.9, an interference pattern of the virtual 3D object corresponding to phase-shifting step $\phi = \pi$ is shown, the other patterns are visually similar. Fig. 2.10 and 2.11 give the numerically reconstructed intensity in the real image planes where $d = 2m$, $2.1m$, respectively. Different objects are focused by the change of focus depth. The numerically reconstructed real amplitude in the virtual image plane where $d = 2.1m$ is shown in Fig. 2.12. In the amplitude image, one can observe that the object in the focused plane is focused while other objects are blurred.

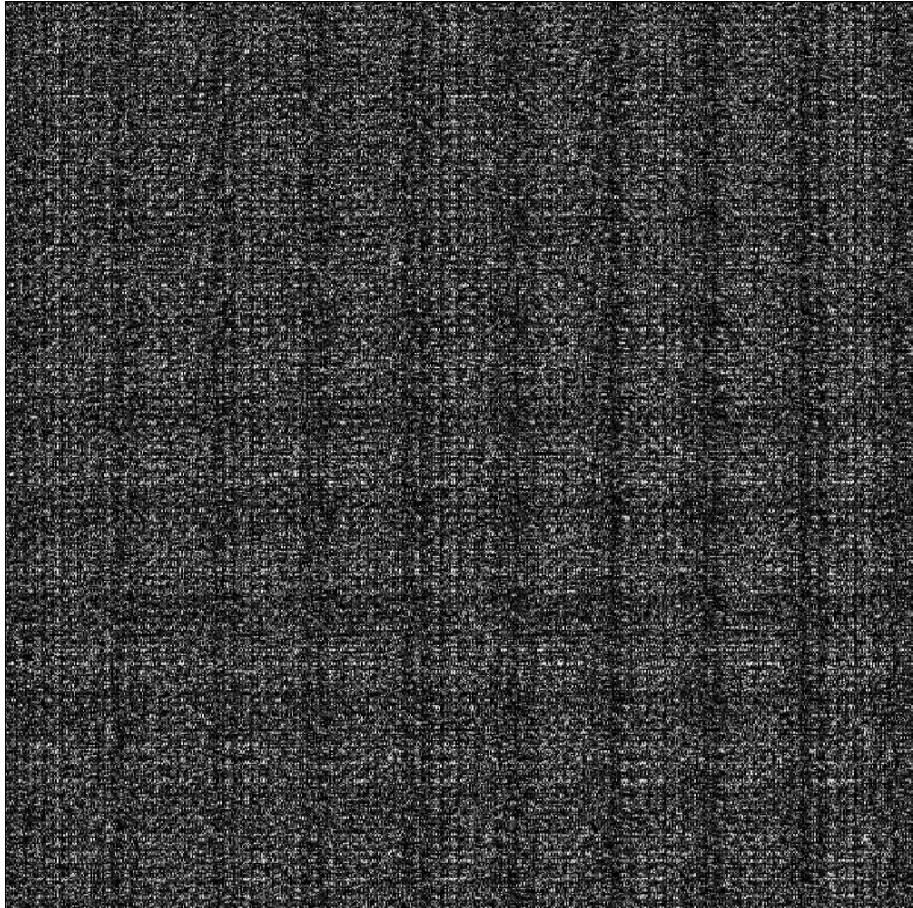


Figure 2.9: CGPSH with $\phi = \pi$ (contrast adjusted)

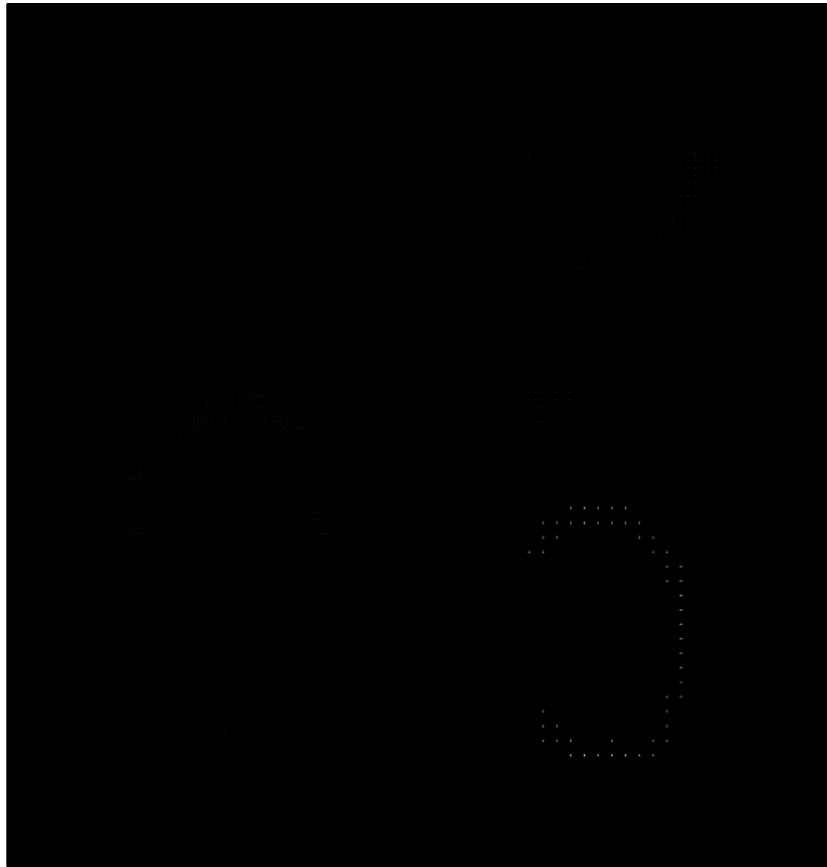


Figure 2.10: Reconstructed intensity in the real image plane $d = 2m$.

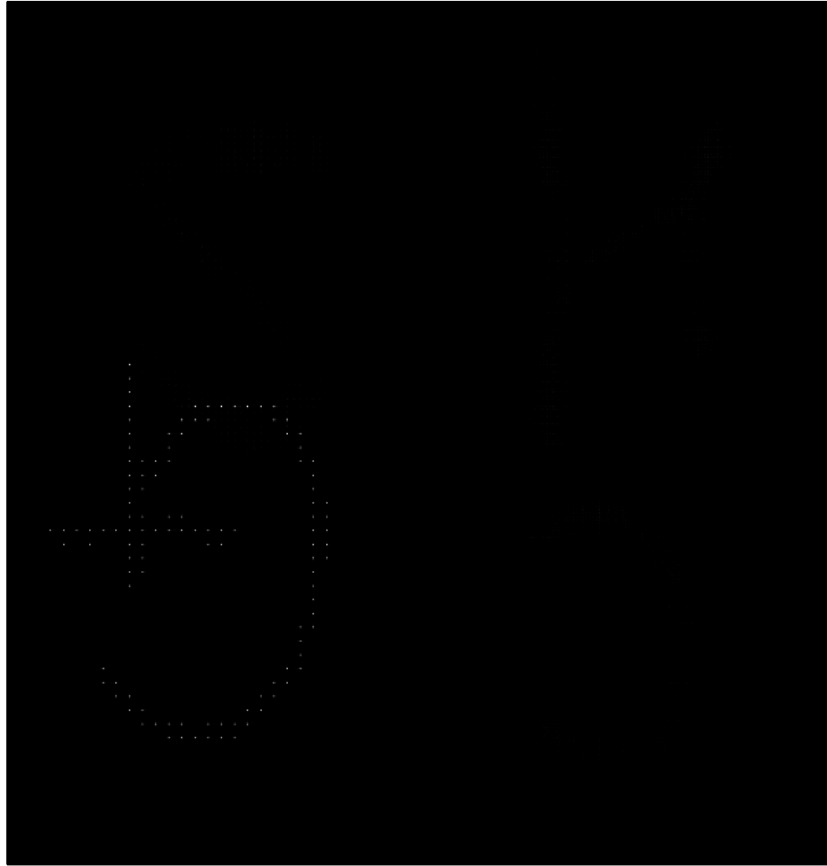


Figure 2.11: Reconstructed intensity in the real image plane $d = 2.1m$.

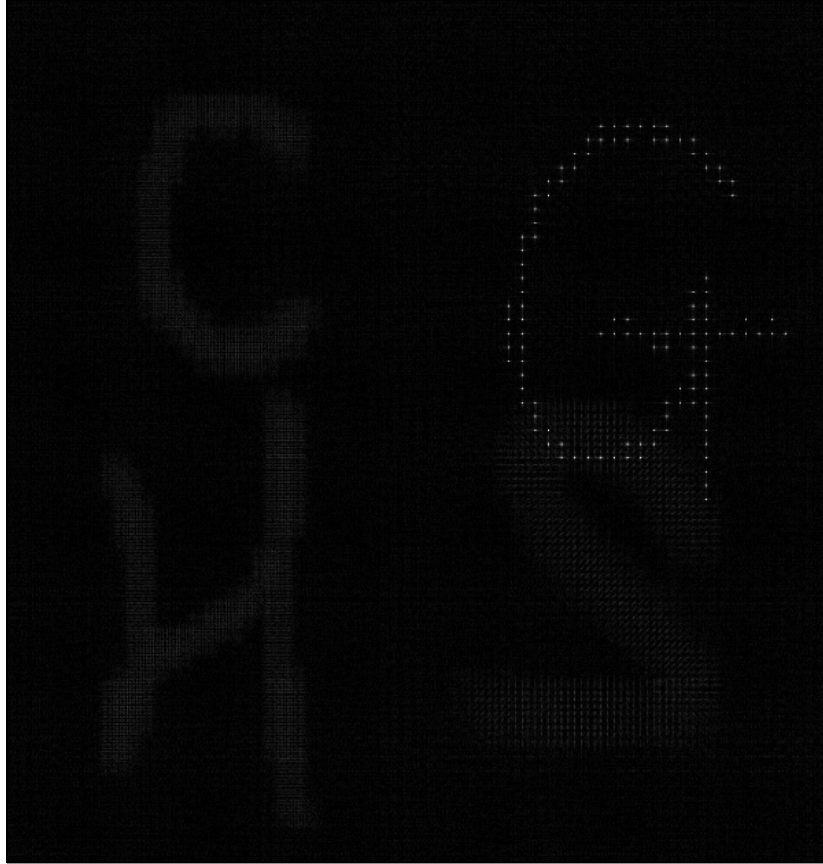


Figure 2.12: Reconstructed amplitude in the virtual image plane $d = 2.1m$.

2.5.2 Fresnel Hologram

According to Goodman [22], the wave propagation from the object plane to the hologram plan can be treated as Fresnel diffraction with a Fourier transform, when a planar transparent object in an opaque plane is illuminated. Similar to Sec. 2.3.1, the diffraction pattern or the complex amplitude of the object wave at the hologram plane can be mathematically expressed as

$$U(x, y) = -\frac{i}{\lambda d} e^{ik(d + \frac{x^2 + y^2}{2d})} \int_{-\infty}^{+\infty} \int_{-\infty}^{+\infty} U_O(x', y') e^{[\frac{ik}{2d}(x'^2 + y'^2)]} e^{[-\frac{ik}{d}(xx' + yy')] } dx' dy', \quad (2.24)$$

Considering the same substitution as Eq. (2.14), the discrete complex amplitude is discretized as

$$\begin{aligned}
 U(m, n) = & -\frac{i}{\lambda d} \exp(ikd) \exp[i\pi \lambda d (\frac{m^2}{N^2 \Delta x^2} + \frac{n^2}{N^2 \Delta y^2})] \\
 & \times \sum_{m=0}^{N-1} \sum_{n=0}^{N-1} U_O(k, l) \exp[\frac{ik}{2d} (k^2 \Delta x'^2 + l^2 \Delta y'^2)] \exp[-i2\pi (\frac{km}{N} + \frac{ln}{N})]
 \end{aligned} \tag{2.25}$$

The application of Fresnel hologram is given in the following example.

Example

Assume that the depth of an 3D object is very small comparing with its distance to the recording plane, then the object points could be modeled in one plane parallel to the recording plane. Thus in this example, a projection image of a virtual 3D object (shown in Fig. 2.13(a)) in bitmap format is used from the software Blender. The basic setup for CGPSH is described in Table. 6.1. Three CGPSHs calculated with different phased reference wave $\phi = 0, \frac{\pi}{2}$ and π are shown in Fig. 2.13(b), (c) and (d), respectively. Different interference patterns can be observed with some potential inter correlations.

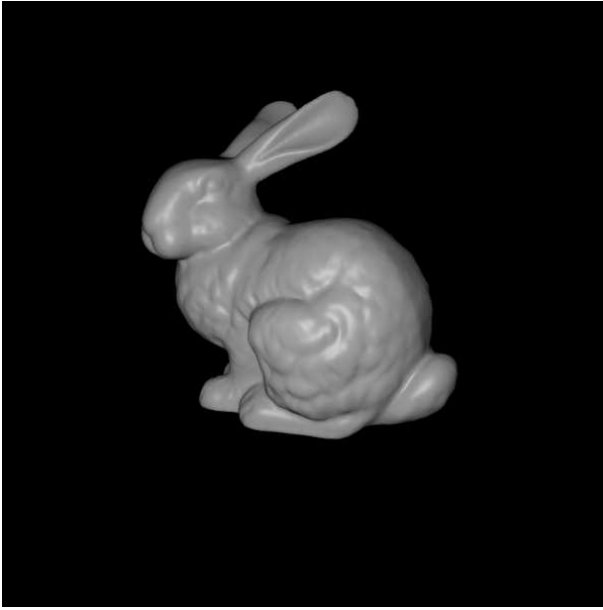
Table 2.1: Parameters of CGPSH

laser wavelength	$\lambda = 630nm$
distance of two planes	$d = 0.55m$
dimension of hologram plane	$L_x \times L_y = 5.5mm \times 5.5mm$
number of samples	$N_x \times N_y = 600 \times 600$

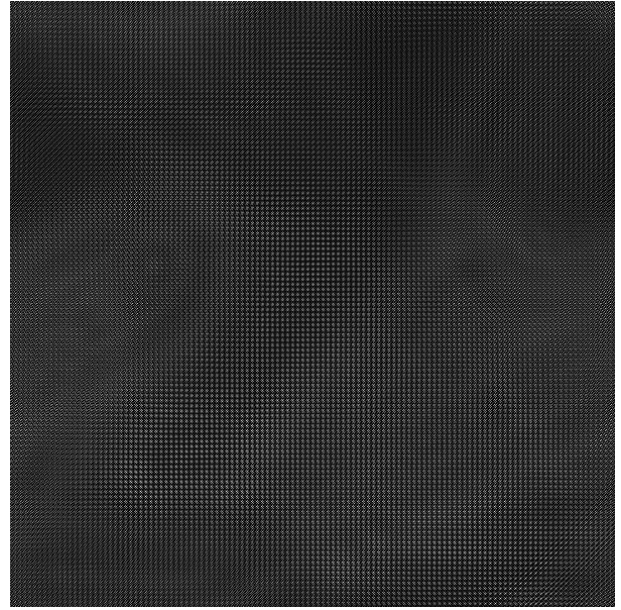
2.6 Conclusion

In this chapter, the main concepts of DH have been explained in detail including optical and numerical hologram acquisition and reconstruction. Combining with phase-shifting scheme, the reconstructed image yields good quality. On the other hand, considering the convenience of CGH for both real objects and virtual objects, PSDH is a very promising 3D technology for practical usage.

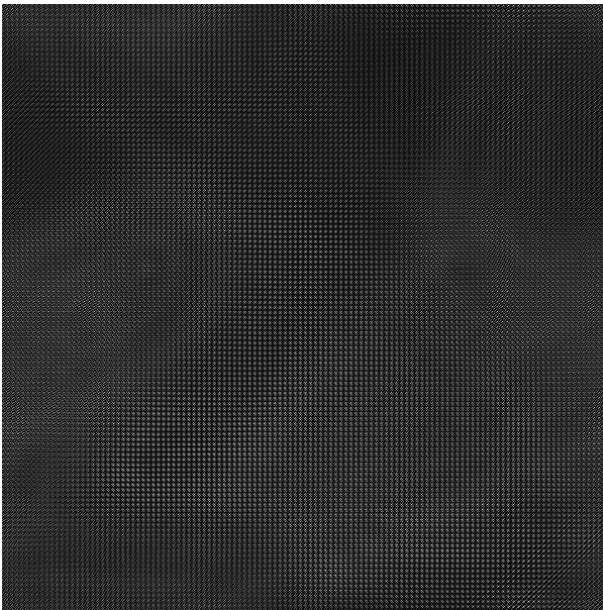
Meanwhile, two examples for obtaining CGPSHs have been given. The ray tracing methods become very time consuming with the increase of object points' number. Thus, Fresnel transform has been selected to generate holograms in this thesis.



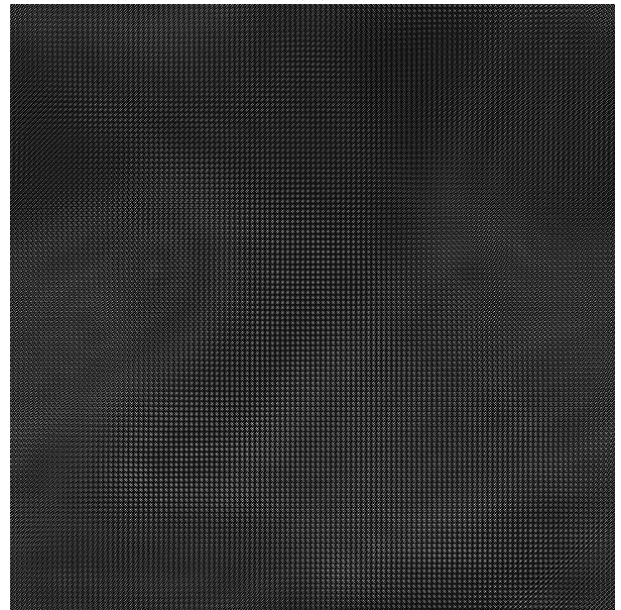
(a)



(b)



(c)



(d)

Figure 2.13: Example of CGPSH by Fresnel transform: (a) original object of “bunny”; (b) A Fresnel hologram of “bunny” with reference wave $\phi = 0$; (c) A Fresnel hologram of “bunny” with reference wave $\phi = \frac{\pi}{2}$; (d) A Fresnel hologram of “bunny” with reference wave $\phi = \pi$.

Chapter 3

Representation and Compression of Digital Holographic Data

3.1 Introduction

In order to make PSDH more practical, some processing on digital holographic data becomes very necessary. The digital procedures in CGH can be generalized as generation of interference patterns, transmission of digital holographic data and display reconstructed image. Due to the experimental limitations, the processing between transmission and display steps is not directly addressed in this thesis.

Considering the case of holographic video streaming by optical recording, each digital hologram encodes multi-views of the object by different windows of pixels. A 12-bit 2028×2044 pixel CCD camera requires around 18 Mbytes of storage for three sets of interference patterns. It takes 1.5 s of transmission time over a 100 Mbit/s network connection for reconstructing the object by phase-shifting interferometry (PSI) algorithm, which is slow for real-time display. In the case of CGPSH, it is even more space consuming. Consequently, investigating efficient compression schemes for digital holograms obtained by PSI is crucial. The aim of this thesis is to develop an efficient holographic compression scheme.

In this chapter, the motivation of using different representations of interference patterns is described in Section 3.2 with the introduction of different representations. The state-of-the-art of existing compression methods are summarized in Section 3.3, based on different representations. Followed in Section 3.4, the analysis of these different representations is conducted by using different quantization methods, giving a basic conclusion on

the redundancy characteristic of each representation. Some conclusions are addressed in Section 3.5.

3.2 Representation of Interference Patterns

3.2.1 Motivation and introduction

Before designing a compression scheme, several problems have to be considered. In order to obtain reconstructed object images with good quality, PSI is necessary for the recording steps. However, three sets of intensity data is not a good compression target. Therefore, reduced data sets are necessary to mitigate the compression burden at the beginning. On the other hand, the data should keep all the useful information for reconstruction. For the solution, it is important to analyze the PSI algorithm.

According to PSI algorithm, the most important information for reconstruction is the complex object field at the hologram plane. If this field can be obtained or expressed by a lower amount of information, this information can be considered as a representation of interference patterns. So far, a few representations have been mainly used in accordance with the PSI algorithm or the expressions of complex numbers, which are introduced in the following.

3.2.2 Intensity based representation

The intensity based representations are obtained from the PSI algorithm. From Eq. (2.18), there are two options:

Intensity information

The intensity information is the direct representation, which has been explained in the previous section. As mentioned above, compressing three sets of data is not the optimal solution. Therefore, it is not encouraged to conduct compression directly on this information.

Shifted distance information

To this end, we introduce the difference data $D^{(1)}$ and $D^{(2)}$ given by:

$$\begin{cases} D^{(1)}(x, y) = I_H(x, y; 0) - I_H(x, y; \frac{\pi}{2}) \\ D^{(2)}(x, y) = I_H(x, y; \frac{\pi}{2}) - I_H(x, y; \pi), \end{cases} \quad (3.1)$$

only two sets of data are necessary to reconstruct the complex field in Eq. (2.18). Since it is less space consuming and obtained straightly from the difference of intensity information, the definition of $D^{(1)}$ and $D^{(2)}$ is highly optimal as one representation of interference patterns. Since this representation is defined by the difference of phase-shifted holograms, hence, we referred to it as “shifted distance information”. Fig. A.2 shows an example of the representation $(D^{(1)}, D^{(2)})$ for the “Bunny” object.

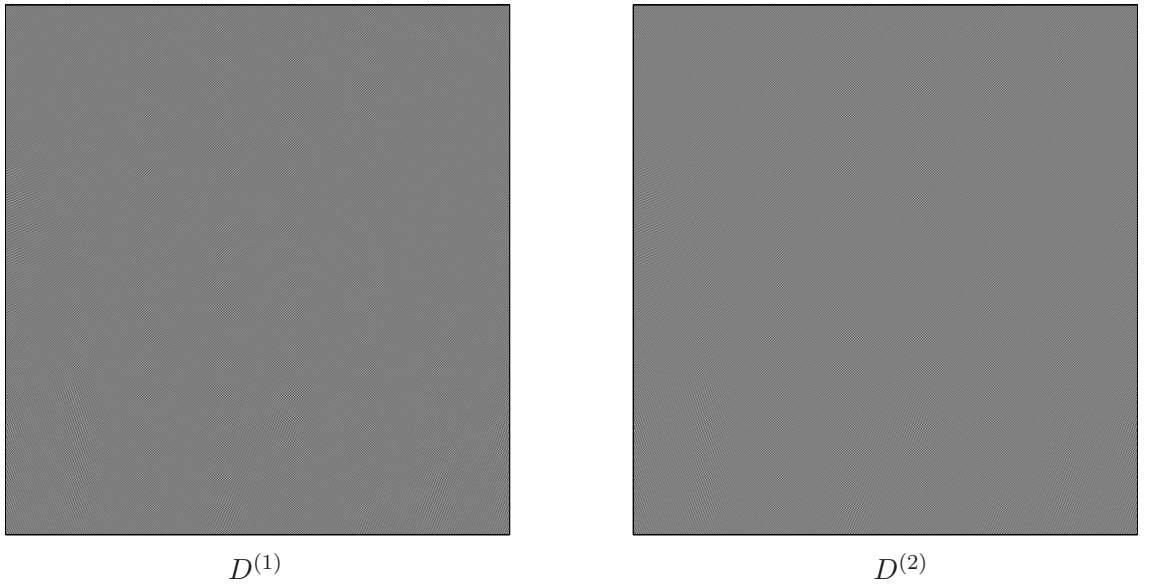


Figure 3.1: Example of two difference data $D^{(1)}$ and $D^{(2)}$ for the “Bunny” object.

3.2.3 Complex amplitude based representation

Complex amplitude based representations are derived from different expressions of the complex field. Noted that a complex number has two kinds of expressions, one is defined in Cartesian coordinate system and the other one in polar coordinate system. Thus, two other kinds of representations for interference patterns are available.

Real-imaginary information

In Cartesian coordinate system, a complex number can be expressed in the form $a+bi$, where a and b are the real part and imaginary part, respectively. Thus, the complex

field obtained by Eq. (2.18) can be expressed as:

$$\widehat{U}_O(x, y) = \text{real}(\widehat{U}_O(x, y)) + i \cdot \text{imag}(\widehat{U}_O(x, y)), \quad (3.2)$$

where $\text{real}(\widehat{U}_O)$ and $\text{imag}(\widehat{U}_O)$ are respectively the real and imaginary part distribution of the complex object field at the hologram plane. Two sets of real and imaginary data is also an optimal representation. Fig. A.3 shows an example of this representation for the “Bunny” object. Similar patterns can be observed compared with the example shown in Fig. A.2.

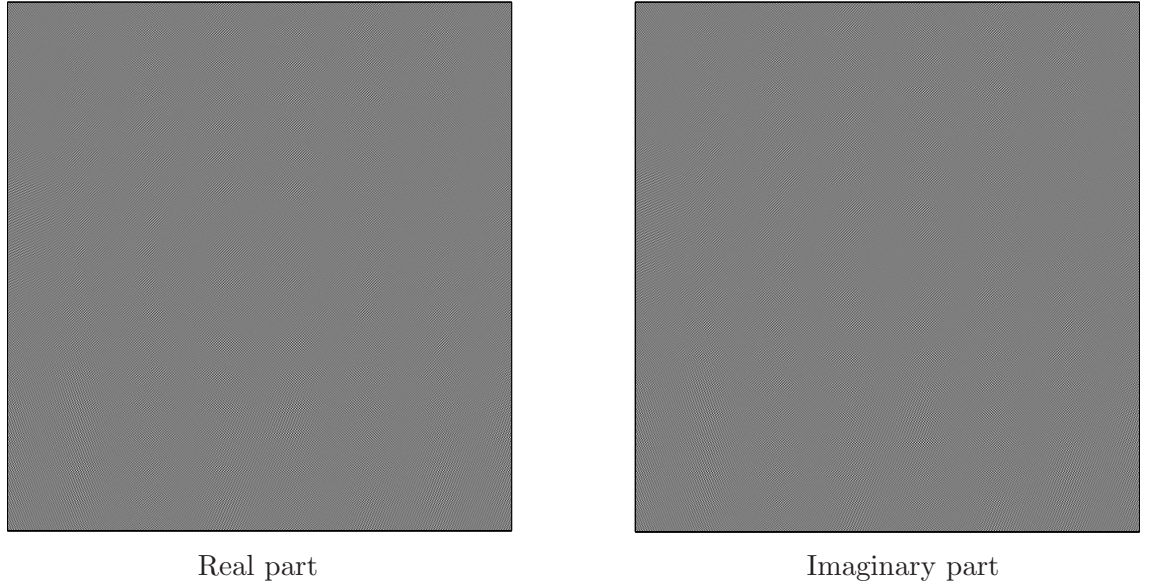


Figure 3.2: Example of real part and imaginary part distributions for the “Bunny” object.

Amplitude-phase information

An alternative way to express a complex number is by polar coordinate system, where the complex field can be written by Euler’s formula as

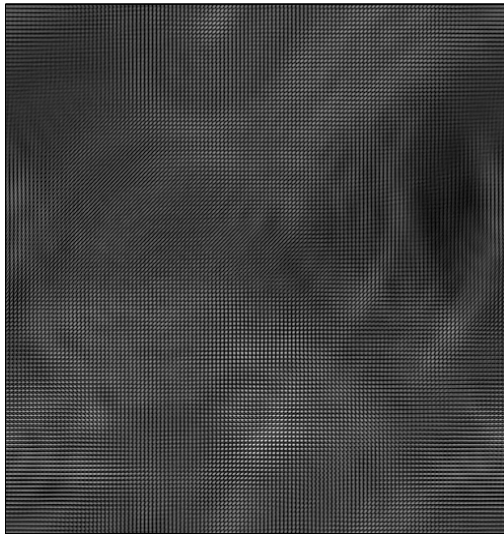
$$\widehat{U}_O(x, y) = \widehat{A}_O(x, y) \cdot e^{i\widehat{\psi}_O(x, y)}, \quad (3.3)$$

where

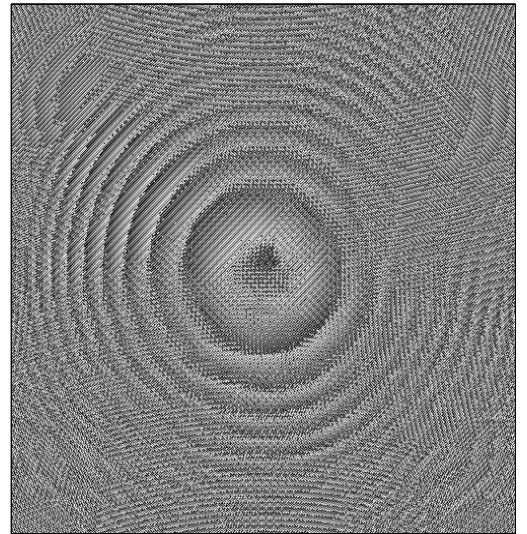
$$\widehat{A}_O(x, y) = |\widehat{U}_O(x, y)| = \sqrt{\text{real}^2(\widehat{U}_O(x, y)) + \text{imag}^2(\widehat{U}_O(x, y))}, \quad (3.4)$$

$$\widehat{\psi}_O(x, y) = \begin{cases} \arctan \frac{\text{imag}(\widehat{U}_O(x, y))}{\text{real}(\widehat{U}_O(x, y))} & \text{if } \text{real}(\widehat{U}_O(x, y)) > 0 \\ \arctan \frac{\text{imag}(\widehat{U}_O(x, y))}{\text{real}(\widehat{U}_O(x, y))} + \pi & \text{if } \text{real}(\widehat{U}_O(x, y)) < 0 \text{ and } \text{imag}(\widehat{U}_O(x, y)) \geq 0 \\ \arctan \frac{\text{imag}(\widehat{U}_O(x, y))}{\text{real}(\widehat{U}_O(x, y))} - \pi & \text{if } \text{real}(\widehat{U}_O(x, y)) < 0 \text{ and } \text{imag}(\widehat{U}_O(x, y)) < 0 \\ \frac{\pi}{2} & \text{if } \text{real}(\widehat{U}_O(x, y)) = 0 \text{ and } \text{imag}(\widehat{U}_O(x, y)) > 0 \\ -\frac{\pi}{2} & \text{if } \text{real}(\widehat{U}_O(x, y)) = 0 \text{ and } \text{imag}(\widehat{U}_O(x, y)) < 0 \end{cases} \quad (3.5)$$

The 3D information of the recorded object is fully contained in this representation, especially the phase information which has a significant influence on reconstruction (explained in later section). Some particular compression schemes could be suitable for this representation. Fig. A.4 shows an example for the “Bunny” object.



Amplitude



Phase

Figure 3.3: Example of amplitude-phase distributions for the “Bunny” object.

3.3 Compression of Digital Holographic Data: State-of-the-art

Even though holography has been invented for more than sixty years, it has received more attention recently thanks to the tremendous achievements in computer technology and digital technology. Numerous work have been attempted on recording using different principles or techniques to generate more practical digital holograms with higher resolution. However, compression of digital holographic data is still a new field of research.

3.3.1 Basic compression tools

Generally, compression techniques are classified into two categories: lossy techniques and lossless ones, to reduce the number of bits. Same as other image compression techniques, a typical coding scheme for digital holographic data incorporating three fundamentals steps of transformation, quantization and lossless coding/entropy coding, is shown in Fig. 3.4. Indeed, the JPEG 2000 image coding framework is commonly used for holographic compression because of its modular and extendable architecture. So the architecture of JPEG 2000 will be introduced, following some other methods utilized for transformation, quantization and entropy coding.

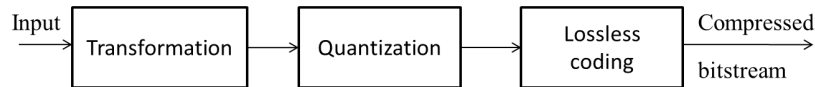


Figure 3.4: Generic compression scheme

Transformation: wavelet based transform

Wavelets have been adapted for the field of image compression for its good property of spatial-frequency localization. This is also essential for compressing holographic data. The classical 1D Discrete Wavelet Transform (1D-DWT) can be simply summarized as applying a pair of lowpass and highpass filters to the input signal, followed by a downsampling to the output of each filter. A multiresolution decomposition can be continued by further decomposing the low frequency subband. For an image, by applying the one dimensional transform once along the rows and once along the columns, the 1D-DWT is extended

to a 2D-DWT. Consequently, four subbands can be obtained by one decomposition: an approximation subband named LL and three detail subbands named HL, LH, and HH corresponding respectively to the horizontal, vertical and diagonal orientations. Moreover, many different filters can be used, for example, the simplest Haar 5/3 filter bank, has the “perfect reconstruction” property while the well-known Daubechies 9/7 filter bank has high compression efficiency [31].

Quantization

Quantization divides a quantity (either continuous or discrete) into a discrete number of small sets, generally, to reach the goal of reducing the storage cost by encoding data samples with fewer levels (and reduced accuracy). The general quantization process is shown in Fig. 3.5.

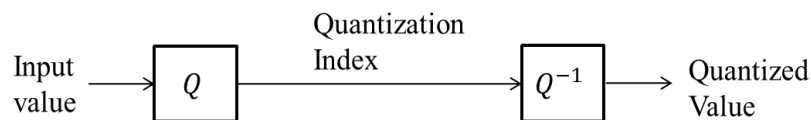


Figure 3.5: Quantization process: Q represents the encoding or quantization stage and Q^{-1} represents the decoding or inverse quantization stage

Generally speaking, two kinds of quantization methods can be distinguished: the scalar quantization (SQ) and the vector quantization (VQ). As the name implies, the primary difference between them is the format of input or output values: scalars or vectors. Simple explanations of uniform SQ (USQ), adaptive SQ (ASQ) based on Lloyd-Max algorithm [32,33] and VQ based on Linde-Buzo-Gray algorithm (VQ-LBG) [34] are described in the following.

Uniform scalar quantization

The simplest example of SQ is uniform SQ, by which an input sample x_i is mapped to an quantized value \hat{x}_i by

$$\hat{x}_i = \lfloor \frac{x_i}{Q_{step}} \rfloor Q_{step}, \quad (3.6)$$

where Q_{step} is the quantization step size and $\lfloor \cdot \rfloor$ is the rounding operator.

Adaptive scalar quantization

The mean squared quantization error (MSQE) is an average loss measurement of

information introduced by quantization. AQ has been proposed to reduce this error for input values which are not uniformly distributed, by reducing the quantization error in densely distributed regions. Lloyd-Max algorithm leads to minimize MSQE.

Vector quantization

The LBG-VQ method is also designed to iteratively minimize MSQE, but on multi-dimensional input. Two criteria should be satisfied: (1) the nearest neighbor condition which means that all vectors that are closer to one certain centroid than any other centroid should be contained in one region and approximated to the centroid as output; and (2) a centroid should be the average of all the vectors in one region.

Entropy coding

After the transformation and quantization step, the generated coefficients need to be encoded. Besides the entropy coding scheme used in JPEG 2000, the embedded zerotree wavelet (EZW) coding [35] and its extended one named the Set Partitioning In Hierarchical Trees (SPIHT) [36] have been proven to be very effective for image compression. Particularly, SPIHT encoding algorithm is commonly used for compressing holographic data because of its good performance. Both of them are based on three principles: partial ordering by magnitude with a set partitioning sorting algorithm, ordered bit plan transmission and exploitation of cross-scale similarities of the wavelet coefficients. However, the big difference between them is the way subsets of coefficients are partitioned. Simply speaking, the zerotree (newly named spatial-orientation tree) concept is improved by using sorted lists in SPIHT instead of the raster scan in EZW. Meanwhile, the partitioning algorithm used in SPIHT is so effective that the arithmetic coding used in EZW is unnecessary.

JPEG 2000

Fig. 3.6 depicts the typical schematic of JPEG 2000 [29], which consists of five main steps in the codec: image tiling (rarely used except the target image is too large), wavelet transform, quantization (applied for lossy case), embedded encoding of code-blocks and rate-distortion optimization. Typically, the input image is first decomposed to different subbands by applying wavelet transform. Then, each transform subband is partitioned into small codeblocks, which are typically of size 32×32 or 64×64 pixels. Each codeblock is separately encoded by embedded block coding, which employs bit-plane scanning and

context-based adaptive arithmetic coding to independently generate embedded bitstreams. Before assembling the individual bitstreams into a single, final bitstream, each codeblock bitstream is truncated by the Lagrangian rate-distortion optimal technique. The truncated bitstreams are then concatenated together to form the final bitstream. This technique is named Embedded Block Coding with Optimal Truncation (EBCOT) [30].

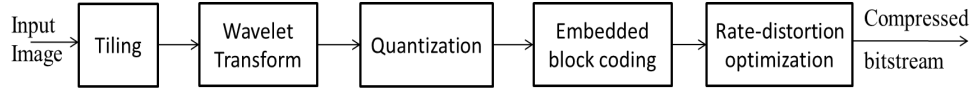


Figure 3.6: Schematic of JPEG 2000

3.3.2 Overview of compression schemes for digital holographic data

Both lossless and lossy compression methods have been attempted in compressing digital holographic data. In the early phase, the performance of lossless coding and quantization methods were mainly investigated, while recent research work are more focused on lossy compression with wavelets transform. As summarized in the following, we categorize most of the research work on compressing holographic data into two kinds of methods: quantization-based methods and transform-based methods.

Compression tool: quantization

Some lossless and lossy data compression methods are applied to real-imaginary information obtained by PSI in [37]. Lossless techniques such as Lempel-Ziv, Lempel-Ziv-Welch, Huffman and Burrows-Wheeler are used to code separated real and imaginary components of data streams. However, due to the low spatial redundancies of hologram's speckle nature, lossless compression methods are usually inefficient [38]. So the lossy compression of holographic data seems essential.

Lossy compression techniques such as subsampling and quantization are applied as well in [37]. Hologram resampling resulted in a high degradation in reconstructed image quality, but for resizing to a side length of 0.5, a compression rate of 18.6 could be achieved with a high degree of median filtering. Quantization proved to be a very effective technique. Each real and imaginary component could be reduced to 4 bits with an acceptable reconstruction error, resulting in a compression rate of 16.

Mills and Yamaguchi [39] also confirmed the effectiveness of quantization in both numerical simulation and optical experiments. The influence of bit-depth limitation in quantization has been demonstrated for by applying to the spot-array patterns (the intensity information). They also pointed out that the use of 4 bits appear to be adequate for visual recognition. However, as the number of bits decreases, the resulting quality falls rapidly by only applying quantization.

Furthermore, Naughton *et al.* improved the quantization of real-imaginary information with a bit packing operation for real-time networking application [40]. A speedup metric is also defined, which combines space gains due to compression with temporal overheads due to the compression routine and the transmission serialization. It has been reported that quantization at 4 bits results in a compression rate of 16, for low normalized root mean square (NRMS) errors in the reconstructed object intensity of less than 0.06.

Later, they applied a companding histogram approach for nonuniform quantization [41, 42]. The companding approach combines the efficiency of uniform quantization with the improved performance of nonuniform quantization. It exploits a priori knowledge of the distribution of the values in the data. The cluster centers from histogram plots of the real and imaginary data are first extracted, as well as from histogram plots of the amplitude and phase digital hologram data. Then, the holographic data is quantized with the resulting cluster centers. The improvements over previous results have been demonstrated and the compression ratios in the range [18, 78] are obtained with good reconstruction quality.

Differently, based on SQ, a multiple description coding (MDC) method is applied on amplitude-phase information using maximum-a-posteriori in [43]. It takes advantage of MDC for optimally coding data between available channels and mitigate channel errors. It turns out to be a powerful mechanism to mitigate channel errors on DHs.

However, being limited in quantization for compressing holographic data can not be efficient enough. Recent work contribute on developing a wavelet-based compression scheme for digital holographic data.

Compression tool: transform-based methods

Shortt *et al.* [44] introduced wavelet analysis for the compression of real-imaginary information. 1D-DWT is applied to each information with different resolution levels. The wavelet coefficients are then quantized in each level. It has been found that 3 levels performed

best on average. In addition, compression of phase-shifting interference patterns by standard JPEG and JPEG 2000 compression techniques is addressed in [45], with reported compression ratios in the range 20 to 27 at acceptable reconstruction levels.

However, standard wavelets are typically designed to process piecewise smooth signals, while holograms contain features which are spread out from the objects. Therefore, applying standard wavelets directly to the hologram is not efficient enough. So Liebling *et al.* [46] developed a family of wavelet bases-Fresnelets-obtained by applying the Fresnel transform operator to b-spline bases, which is specially tailored to the specificities of DH. The multiresolution properties (translation, dilation) of the Fresnel transform are first studied to construct the new wavelet. Differently, the convolution approach in the following is used in the Fresnel reconstruction (Eq. (2.3)) instead of approximation methods introduced previously:

$$\begin{aligned} U(\xi, \eta) &= -\frac{i}{\lambda} \int_{-\infty}^{+\infty} \int_{-\infty}^{+\infty} I_H(x, y) U_R(x, y) \frac{e^{ikr}}{r} dx dy \\ &= (U * G)(\xi, \eta), \end{aligned} \quad (3.7)$$

where

$$G = \frac{1}{\lambda d} \exp\left[\frac{i\pi}{\lambda d}(x^2 + y^2)\right], \quad (3.8)$$

* denotes convolution, and the constant part has been neglected for simplicity. Moreover, a Heisenberg-like uncertainty relation giving a bound on the spatial spreading in the Fresnel domain is derived, which guides to the definition of Fresnelets. The Fresnelet basis is the Fresnel transform of a B-spline. 1D B-splines of degree n are defined as the $(n + 1)$ -fold convolution of a rectangular pulse [47]

$$\beta^n(x) = \underbrace{\beta^0 * \dots * \beta^0}_{n+1 \text{ times}}(x), \quad (3.9)$$

where

$$\beta^0(x) = \begin{cases} 1, & -\frac{1}{2} < x < \frac{1}{2} \\ \frac{1}{2}, & |x| = \frac{1}{2} \\ 0, & \text{otherwise.} \end{cases} \quad (3.10)$$

The F-splines is then obtained by convolving $G(x)$ with the B-spline $\beta^n(x)$. It can be extended to 2D and used as the decomposition bases to the object wavefront at different distances by extending B-splines to 2D as

$$\beta^n(x, y) = \beta^n(x) \cdot \beta^n(y), \quad (3.11)$$

where \cdot denotes the tensor product. The particular suitability of the Fresnel B-splines has been concluded. However, it was only used for reconstruction of off-axis digital holograms which are limited by some unwanted terms.

Darakis *et al.* [48] introduced the use of Fresnelets into PSDH for holographic data compression. They first separately decompose the real-imaginary information to Fresnelet coefficients to a required scale depth. The real and imaginary Fresnelet coefficients are then fed to the SPIHT algorithm. Experimental results verified its extensive flexibility for the compression of PSI holographic data.

However, Viswanathan *et al.* [49] analyzed that Fresnelets have limitations for showing localization in frequency regarding a viewpoint-based degraded reconstruction. Instead, they proposed to use Gabor wavelets which is suitable for measuring the local spatial frequencies so that coefficients can be pruned corresponding to a viewpoint selection. Also differently, the Angular Spectrum method is used to perform the reconstruction instead of the Fresnel transform. The experimental results prove that Gabor wavelet is able to suppress the unwanted orders created in the reconstruction for off-axis holograms and have better time-frequency localization for view-dependent compression techniques. Moreover, they proposed to use Morlet wavelets for transforming a hologram and partly reconstructing a scene by using a sparse set of Morlet transformed coefficients in [50]. It has been shown that view-dependent representation along with Morlet wavelets form a good starting step for compressing holographic data for next generation 3DTV applications.

On the other hand, Blinder *et al.* [51] also investigated wavelet coding on off-axis holograms. Differently, the properties of the off-axis holograms are first examined by independent component analysis, which reveals the importance of orientation and high frequencies in off-axis holograms. For this reason, standard decomposition schemes are not very suitable for compressing holograms. They proposed some alternative decomposition schemes that further decompose the high-frequency subbands and direction-adaptive wavelets [52] are combined to improve the compression performance with standard JPEG 2000 algorithm.

Significant improvement has been reported for lossy compression compared with the standard DWT using the Mallat decomposition. Furthermore, they proposed a wavelet packet decomposition scheme combined with directional wavelet transforms for compressing microscopic off-axis holograms in [53]. Still, the JPEG 2000 standard is modified to cope with holograms by applying the new wavelet decomposition with directional wavelet transforms. The extended JPEG 2000 algorithm shows higher compression efficiency improvements.

3.3.3 Limitations in the state-of-the-art

Above all, what in common can be summarized. First, there is no standard metrics for evaluating the efficiency of compression schemes. Some metrics used on natural images, such as compression ratio, NRMS, PSNR and so on, have been applied to either the compressed holograms or reconstructed images. However, different works are not strictly comparable due to the complicated system of DH. Typically, the fringes appearing on the holograms can be very different according to different setups (the object numbers, the recording distance and so on), especially between CGH and optical recorded hologram. Normally, more patterns present in CGH than real recorded hologram. Moreover, the compression targets are also different. Except for the different representations represented in PSDH, off-axis holograms are considered as well. Consequently, the evaluations on different targets are not strictly comparable. Unfortunately, there isn't public holographic data base. As a result, the comparisons in most of the work have been done based on their private data.

In this thesis, performance is assessed on the image numerically reconstructed from the complex field. The main point is that the quality of the reconstructed image is one of two key concerns (recording and reconstruction) in holography. In most following part of this thesis, two quality measurements used in standard images, the peak signal-to-noise ratio (PSNR) and the structural similarity (SSIM) indexes [54], are applied to measure the reconstruction quality. The image reconstructed from compressed holographic information is measured based on the initial one without compression.

Second, wavelets based methods are considered effective for compressing holographic data. However, all the coding schemes described above encode different holographic data independently. It could be more efficient to combine wavelet transform and joint encoding methods to compress phase-shifting holographic data. In this thesis, it is more focused on developing a wavelet-based joint encoding scheme for a specific holographic representation. Thus, the basis analysis on different holographic representations are first studied in the

following.

3.4 Basic Analysis of Different Representation Data

3.4.1 Motivation

In this section, basic redundancy analysis between the information in accordance with each representation is conducted for better designing compression schemes. So far, except the pure intensity representation, three other representations are available with a lower amount of raw data. Then the following questions could be asked:

1. Which representation should be chosen? What characteristics does it have?
2. In one representation, is it possible that one set of information affects more on the reconstruction than the other one?
3. How to design a compression scheme? Should it be specifically designed for a given representation?

Apparently, only on the basis of well understanding the essence of these holographic data, it is closer to answer these questions. It is worth noting that, observed from Fig. A.2, A.3 and A.4, the patterns between the shifted distance information are similar, so as those between the real-imaginary information. However, in the amplitude-phase representation, patterns are rather dissimilar. It can be inferred that more redundancies exist in shifted distance information or real-imaginary information than in amplitude-phase information. Consequently, inter compression methods can effectively be applied on representations with more redundancies. However, these observations need to be verified by experiments.

Based on the above considerations, some basic analysis of different holographic data are conducted in the following.

3.4.2 Analyzing tools: quantization

The main analyzing tools used to study the characteristics of different representations are some common methods of quantization. Considered as a basic tool used in lossy compression schemes, quantization methods can also be applied with the aim of compressing CGPSHs. It is known that SQ processes input values individually while VQ processes them

simultaneously. The different processing ways make possible the comparative analysis of input data, which is addressed in the following.

Impact analysis

By processing two kinds of information individually, the impact of each information on reconstructions can be learned. For instance, there are two kinds of information $I^{(1)}$ and $I^{(2)}$. In case 1, $I^{(1)}$ is only quantized by a very low bit level, while $I^{(2)}$ is quantized by different bit levels (suppose that the bit levels change incrementally); a converse processing on $I^{(1)}$ and $I^{(2)}$ is conducted in case 2. If case 1 outperforms case 2 at all bit levels or levels bigger than a certain one, it can be concluded that $I^{(2)}$ impacts more on reconstructions than $I^{(1)}$.

By visually analyzing all the representations, only the distributions of amplitude-phase information are rather different. It means that they probably behave very differently on reconstructions.

Redundancy analysis

The simultaneous processing by VQ is able to prejudge the redundancy between two kinds of information in each representation. For example, two representations are processed as input in vector format (I_1, I_2) and (I'_1, I'_2) . By VQ, if (I_1, I_2) outperforms (I'_1, I'_2) at any bit level, it implies higher redundancy existing between information I_1 and I_2 .

As noted above, the shifted distance information, also the real-imaginary information, has similar patterns between two kinds of information. Hence, the redundancy should be verified in them.

Therefore, both SQ and VQ methods are applied in the analysis.

3.4.3 Comparative study

Before the comparative study, several comparison design issues should be stated first.

- The “bitmap” model which only contains one object, is selected to generate CGPSHs because of the fast calculation speed and simple setup. The digital hologram example has been shown in section 2.5.2. The basic setup is given in Table 6.2.

Table 3.1: Parameters of CGPSH

laser wavelength	$\lambda = 630nm$
distance of two planes	$d = 0.55m$
dimension of hologram plane	$L_x \times L_y = 5.5mm \times 5.5mm$
number of samples	$N_x \times N_y = 512 \times 512$

- For the sake of simplicity, only PSNR index is reported in this study, whose definition is given as follows:

$$PSNR = 10 * \log_{10}\left(\frac{\max(I_{ref})^2 - \min(I_{ref})^2}{MSE}\right), \quad (3.12)$$

$$MSE = \frac{1}{MN} \sum_{m=1}^M \sum_{n=1}^N [I_{ref}(m, n) - I_{rec}(m, n)]^2.$$

where I_{ref} is the $M \times N$ reference image (or the image reconstructed from uncompressed holographic data), $\max(I_{ref})$ and $\min(I_{ref})$ are the maximum and minimum pixel values of the reference image, respectively. I_{rec} is the approximated image reconstructed from compressed holographic data and MSE is the mean square error. The reference image and approximated image are the reconstructed intensity images instead of amplitude images.

Based on the designs described above, three virtual objects (“Luigi”, “Girl” and “Bunny”) shown in Fig. 3.7 are selected in the experiments. Comparative studies are conducted separately in each representation and between different representations for different purposes. The experimental results and discussions are described in the following.

Comparative study in each representation

In the first set of experiments, three representations are separately quantized by USQ and each information is quantized with bit levels from 2 to 7. Table. 3.2, 3.3 and 3.4 evaluate the reconstruction quality of “Luigi” object (Am: amplitude, Ph: phase, Re: real part, Im: imaginary part). Fig. 3.8, 3.9 and 3.10 show corresponding illustrations.

- From Fig. 3.8, the different contributions of amplitude information and phase information can be easily observed. At a certain bit level of amplitude information, the change of PSNR value is sharper than that at the same bit level of phase information. Similarly, it is implied in the numbers in Table. 3.2, that the



Figure 3.7: Testing objects: “Luigi”, “Girl” and “Bunny”.

phase information contributes more on the reconstruction than the amplitude information. For example, when the bit level of amplitude information is 4, the PSNR difference reaches 22 dB as the bit level of phase information changes from 2 to 7; on the other hand, however, only a difference of 13 dB is obtained when the bit level of phase information is 4.

- A quite balanced contribution of real-imaginary information and shifted distance information can be observed from Fig. 3.9 and Fig. 3.10, respectively. The numerical evaluation in Table. 3.3 and 3.4 also proves the balance.

In the second set of experiments, ASQ is applied to improve the performance of all the representations by analyzing their probability distributions. It is shown in Fig. 3.11 that, except for the phase information, all channels have obvious non-uniform distributions. The real-imaginary information shares very similar distributions with the shifted distance information. Moreover, the reconstruction results of both representations are also very similar. So the real-imaginary information is considered having similar characteristics as the shifted distance information. It subsequently is not considered again in this comparative study because the shifted distance information has priority in practice, which can be more directly obtained before applying phase-shifting algorithm. Further comparison between the two similar representations will be addressed in next chapter.

Table 3.2: PSNR obtained from quantizing amplitude-phase information of “Luigi” object by USQ

number of bits		Ph					
		2	3	4	5	6	7
Am	2	24.66	30.79	31.27	31.22	31.26	31.27
	3	25.14	35.06	38.45	39.04	39.47	39.58
	4	25.24	36.43	42.71	44.79	46.76	47.34
	5	25.25	36.67	44.00	47.29	51.89	54.15
	6	25.26	36.72	44.25	47.85	53.80	58.10
	7	25.26	36.73	44.30	47.97	54.38	59.80

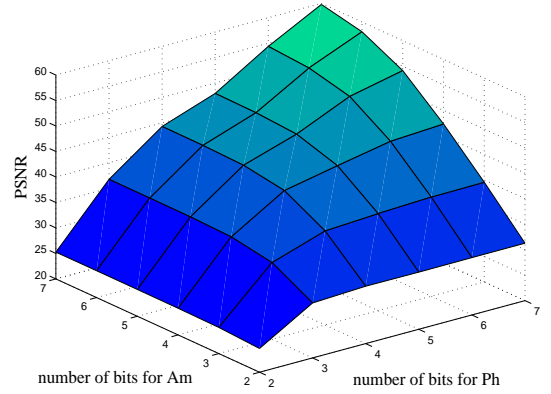


Figure 3.8: Corresponding figure of Table. 3.2

Table 3.3: PSNR obtained from quantizing real-imaginary information of “Luigi” object by USQ

number of bits		Im					
		2	3	4	5	6	7
Re	2	20.24	25.30	26.70	26.91	26.93	26.94
	3	25.26	32.05	35.50	36.27	36.42	36.47
	4	26.63	35.51	40.42	42.70	43.38	43.56
	5	26.82	36.29	42.67	46.74	48.77	49.50
	6	26.85	36.46	43.37	48.83	52.75	54.85
	7	26.86	36.51	43.57	49.56	54.77	58.81

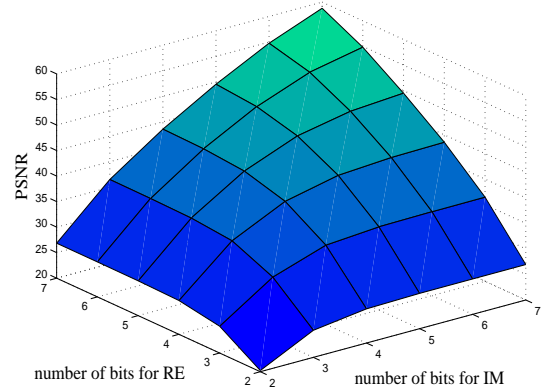


Figure 3.9: Corresponding figure of Table. 3.3

Table 3.4: PSNR obtained from quantizing shifted distance information of “Luigi” object by USQ

number of bits		D_2					
		2	3	4	5	6	7
D_1	2	20.43	25.45	26.86	27.06	27.09	27.10
	3	25.48	32.22	35.66	36.45	36.63	36.68
	4	26.84	35.62	40.47	42.73	43.45	43.66
	5	27.02	36.35	42.70	46.77	48.85	49.57
	6	27.05	36.52	43.40	48.82	52.85	54.93
	7	27.06	36.57	43.61	49.55	54.89	58.88

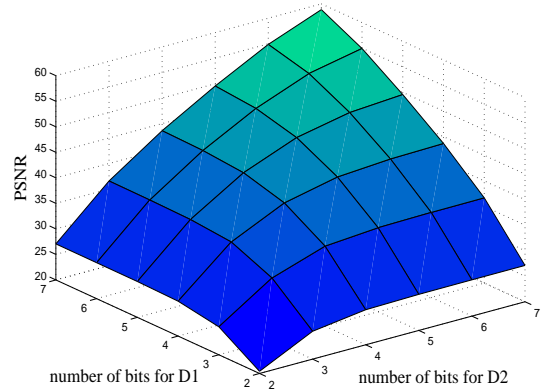


Figure 3.10: Corresponding figure of Table. 3.4

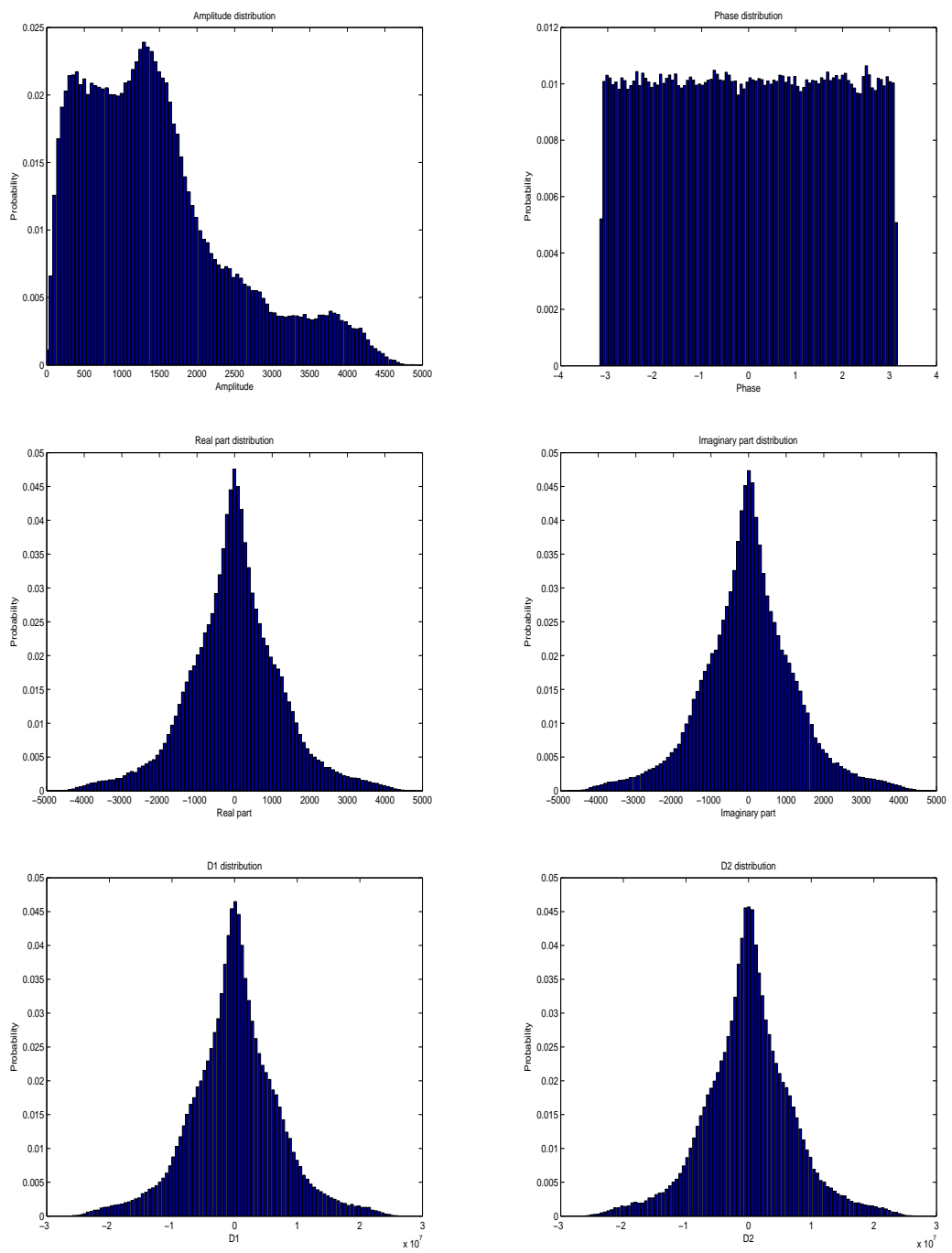


Figure 3.11: Probability distribution of different representations.

Table 3.5: PSNR obtained from ASQ and USQ on amplitude-phase (Am,Ph) and D1, D2 information of three objects

bit level	PSNR of Luigi				PSNR of Girl				PSNR of Bunny			
	Am,Ph		D1,D2		Am,Ph		D1,D2		Am,Ph		D1,D2	
	ASQ	USQ	ASQ	USQ	ASQ	USQ	ASQ	USQ	ASQ	USQ	ASQ	USQ
2	24.74	24.66	25.63	20.43	25.82	26.01	26.71	19.71	19.36	18.77	22.81	15.65
3	35.12	35.06	34.61	32.22	35.73	35.67	34.53	31.63	28.69	28.28	29.71	25.38
4	42.83	42.71	42.44	40.47	43.61	43.32	42.51	40.36	35.26	34.83	36.23	32.33
5	47.27	47.29	48.77	46.77	48.16	48.09	49.35	47.07	41.11	40.82	41.85	38.51
6	53.82	53.80	53.71	52.85	54.72	54.72	54.02	53.04	46.91	46.82	45.73	44.51
7	59.80	59.80	58.89	58.88	60.54	60.57	59.15	59.08	52.90	52.90	50.53	50.52

Back to the consideration of the probability distributions, the quality of the reconstructions from quantizing shifted distance information by ASQ shows big improvements. Contrarily, due to the less contribution of the amplitude information, few gains can be obtained when applying ASQ to amplitude-phase information. These conclusions are confirmed in Table. 3.5. In the table, each information set is quantized with the same bit level.

Comparative study between different representations

In the third set of experiments, the investigation of redundancy is conducted between the representations of amplitude-phase information and shifted distance information. As mentioned above, it is necessary to investigate the redundancy between two sets of information in each representation, especially the shifted distance one because of the similar inter appearance. For this reason, 2D inter vector quantization is applied to each representation, where an input vector consists of one element from one information and the corresponding element from the other information.

Before applying LBG-VQ, normalizing amplitude-phase information is necessary to obtain the input vector of VQ due to the huge difference of the ranges between amplitude-phase information. In the encoding process, the codebook is produced by training all vectors until the mean square error is lower than a threshold $\tau = 0.001$. Table. 6.3 evaluates the performance of LBG-VQ on amplitude-phase and shifted distance information of three objects. The average bit level varies from 1 to 5.

- It is verified that with the increasing size of the codebook, shifted distance information outperforms amplitude-phase information, which further implies the

Table 3.6: PSNR obtained from LBG-VQ on amplitude-phase (Am,Ph) and shifted distance information of three objects

number of bits	PSNR of Luigi		PSNR of Girl		PSNR of Bunny	
	Am,Ph	D1,D2	Am,Ph	D1,D2	Am,Ph	D1,D2
1	16.15	19.54	16.40	16.99	13.92	16.05
2	17.97	27.61	27.64	29.56	22.39	23.38
3	34.10	35.75	36.36	37.36	29.17	30.52
4	40.62	43.18	42.90	45.15	35.46	37.54
5	46.72	50.26	49.12	52.47	41.58	44.07

potential correlation between the two sets of shifted distance information.

- Comparing with the evaluations of ASQ in Table. 3.5, the difference of LBG-VQ on amplitude-phase information is rather limited to less than 1dB, while the improvement on shifted distance information could reach around 3dB. Higher redundancy existing in shifted distance information (also in real-imaginary information) is experimentally confirmed.
- The better performance of shifted distance information is also verified by the visual difference of reconstructed intensities in Fig. 3.12, 3.13 and 3.14. Reconstruction images from amplitude-phase information and shifted distance information are given in the left and right column, respectively, at bit levels of 2, 3 and 4. Different from the distortions which could appear in normal images by VQ, the intensity of reconstructed objects from quantized holographic information shows surface roughness at high compression.

As a conclusion, the amplitude-phase information is better encoded separately. However, jointly encoding, or inter compression methods can bring more benefits on representations with higher redundancy, such as real-imaginary information and shifted distance information.

3.5 Conclusion

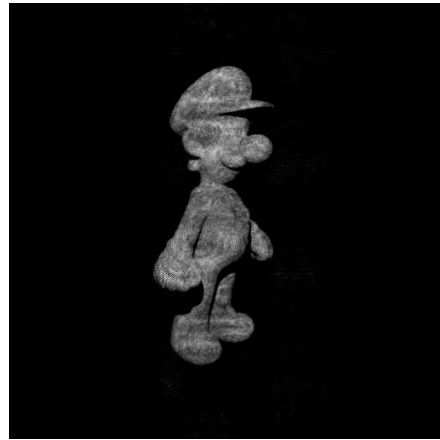
In this chapter, different representations obtained from PSI have been described for generating complex amplitude at the hologram plane: the intensity of interference patterns, the shifted distance information, the amplitude-phase information and the real-imaginary information. For the targeted selection of compression objects, some basic characteristics of

different representations have been investigated by different quantization methods. It has been confirmed that the amplitude-phase information is more suitable to be encoded independently, while the shifted distance information or real-imaginary information fits better in inter compression.

The state-of-the-art of compressing digital holographic data has been overviewed at the end. In addition to the introduced independent encoding schemes, our following work will contribute to introduce joint encoding schemes considering the effectiveness of wavelet transform.



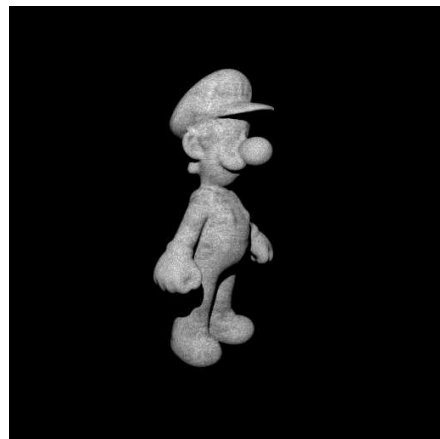
bit level=2, PSNR=17.97



bit level=2, PSNR=27.61



bit level=3, PSNR=34.10



bit level=3, PSNR=35.75



bit level=4, PSNR=40.62



bit level=4, PSNR=43.18

Figure 3.12: Reconstructed images at bit levels of 2, 3 and 4 from amplitude-phase information (left column) and shifted distance information (right column) of “Luigi” object



number of bits=2, PSNR=27.64dB



number of bits=2, PSNR=29.56dB



number of bits=3, PSNR=36.36dB



number of bits=3, PSNR=37.36dB



number of bits=4, PSNR=42.90dB



number of bits=4, PSNR=45.15dB

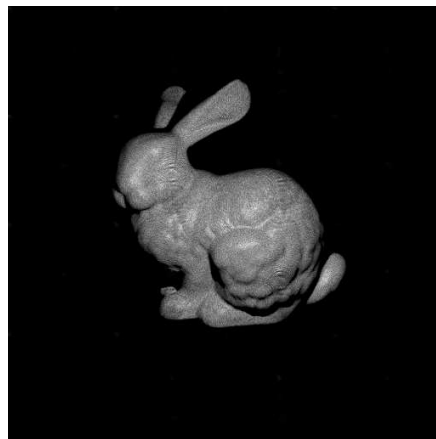
Figure 3.13: Reconstructed images at bit levels of 2, 3 and 4 from amplitude-phase information (left column) and shifted distance information (right column) of “Girl” object



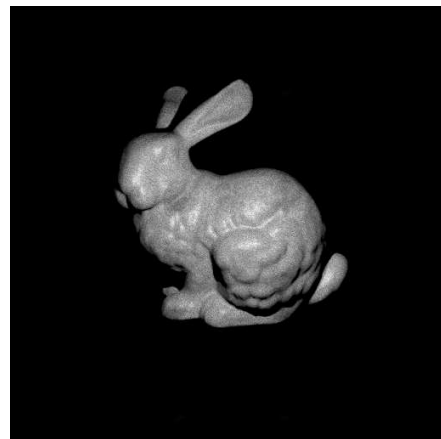
bit level=2, PSNR=22.39



bit level=2, PSNR=23.38



bit level=3, PSNR=29.17



bit level=3, PSNR=30.52



bit level=4, PSNR=35.46



bit level=4, PSNR=37.54

Figure 3.14: Reconstructed images at bit levels of 2, 3 and 4 from amplitude-phase information (left column) and shifted distance information (right column) of “Bunny” object

Chapter 4

Separable Vector Lifting Scheme on Digital Phase-shifting Holographic Data

4.1 Introduction

The conclusion at the end of last chapter gives some solutions for the design of digital holographic data compression schemes. In this chapter, a novel approach based on Vector Lifting Scheme (VLS) is proposed for jointly encoding redundant holographic representations by taking advantage of multiresolution analysis.

This chapter is organized as follows. In Section 4.2, some basic knowledge about lifting scheme (LS) and separable VLS are first presented. Then, in Section 4.3, the proposed compression scheme based on VLS is addressed. Finally, the experimental results are given in Section 4.4 and some conclusions are drawn in Section 4.5.

4.2 Vector Lifting Scheme

4.2.1 Introduction: Lifting schemes

LS [55–58] is an alternative method for computing DWT, which is simpler and faster than the classical one (introduced in last chapter). The original signal can also be easily obtained by the inverse transform. With these advantages, LS has been proven to be an efficient tool

for still image coding. Many extensions have been applied to LS. Particularly, one of them known as Quincunx lifting scheme has been found useful for coding satellite images by using a quincunx grid [59]. Moreover, some directional transforms, such as oriented wavelet transform [60] and grouplet [61], have also been developed with LS for image processing.

4.2.2 Basic concepts of lifting schemes

Fig. 4.1 shows a generic separable LS structure for 1D signal with one level resolution. Biorthogonal wavelets can be constructed by a series of operators including *split*, *predict* and *update* in the forward transform (analysis step).

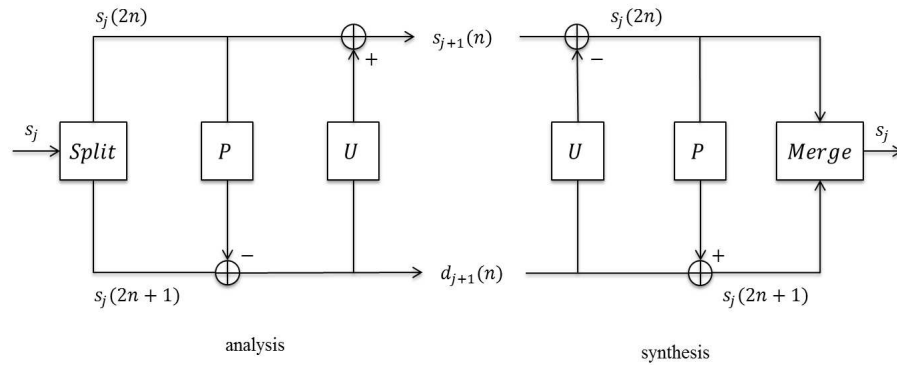


Figure 4.1: Generic lifting structure.

Split : First, the input 1D signal s_j is partitioned into two sample sets: the even samples $s_j(2n)$ and the odd samples $s_j(2n + 1)$.

Predict : Next, predict each sample in one of the subsets by the neighboring samples in the other subset. A prediction error or detail signal, for the case of predicting odd sample (the same for the following contents), can be computed:

$$d_{j+1}(n) = s_j(2n + 1) - \mathbf{p}^\top \mathbf{s}_j(n) \quad (4.1)$$

where \mathbf{p} is the prediction vector containing the prediction weights, $\mathbf{s}_j(n) = (s_j(2n - 2k))_{k \in \mathcal{P}}$ is the reference vector containing the even samples for predicting the odd sample, and \mathcal{P} is the support of the predictor.

Update : Then, a coarser approximation of the original signal is generated by a smoothing

operation on the even samples using the detail coefficients:

$$s_{j+1}(n) = s_j(2n) + \mathbf{u}^\top \mathbf{d}_{j+1}(n) \quad (4.2)$$

where similarly, \mathbf{u} is the update vector containing the weights of update operator, $\mathbf{d}_{j+1}(n) = (d_{j+1}(n-k))_{k \in \mathcal{U}}$ is the reference vector containing the detail coefficients, and \mathcal{U} is the support of the update operator.

It is obvious that the two sample subsets can be easily reconstructed from the forward transform by two inverse operators:

Undo update :

$$s_j(2n) = s_{j+1}(n) - \mathbf{u}^\top \mathbf{d}_{j+1}(n) \quad (4.3)$$

Undo predict :

$$s_j(2n+1) = d_{j+1}(n) + \mathbf{p}^\top \mathbf{s}_j(n) \quad (4.4)$$

Then, they are merged to obtain the original signal. Above all, the LS is easier to implement than the filter bank based method.

Similarly, the separable 2D-DWT can also be implemented by applying the 1D case to the lines and columns. Also, one can obtain a multiresolution representation by recursively repeating the analysis steps to the approximation coefficients.

4.2.3 VLS decomposition

Based on LS, VLS has been developed to jointly encode two sets of dependent signals with multiscale decomposition [7, 62]. For the sake of simplicity, a separable vector lifting structure, whose block diagram is illustrated in Fig. A.5, is tentatively investigated in this chapter.

The principle of this multiscale decomposition are described for a given line x . In what follows, $S_j^{(1)}$ and $S_j^{(2)}$ designate the approximation coefficients of 2D signals $S^{(1)}$ and $S^{(2)}$ at each resolution level j . While $j = 0$ corresponds to the initial (full resolution) signal $S^{(1)}$ and $S^{(2)}$, note that the dimensions of $S_j^{(1)}$ and $S_j^{(2)}$ ($j \geq 1$) are divided by 2^j along the horizontal and vertical directions.

Decomposition of reference signal

As it can be seen in Fig. A.5, the reference signal $S^{(1)}$ is firstly encoded using a

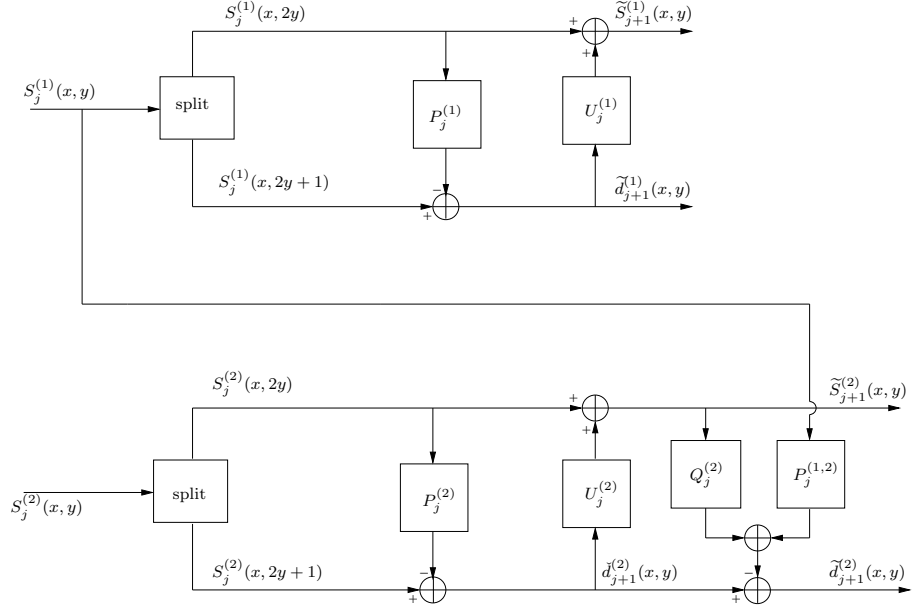


Figure 4.2: Principle of the VLS decomposition.

classical lifting structure composed of a prediction and an update stage. To this end, for a given line x , the input signal $S_j^{(1)}(x, y)$ is firstly partitioned into two data sets formed by the even $S_j^{(1)}(x, 2y)$ and odd samples $S_j^{(1)}(x, 2y + 1)$, respectively. Then, during the prediction step, each sample of one of the two subsets (say the odd ones) is predicted from the neighboring even samples, yielding the detail coefficients $\tilde{d}_{j+1}^{(1)}$ at the resolution $(j + 1)$:

$$\tilde{d}_{j+1}^{(1)}(x, y) = S_j^{(1)}(x, 2y + 1) - \sum_{k \in \mathcal{P}_j^{(1)}} p_{j,k}^{(1)} S_j^{(1)}(x, 2y - 2k) \quad (4.5)$$

where the coefficients $p_{j,k}^{(1)}$ and the set $\mathcal{P}_j^{(1)}$ represent respectively the weights and the support of the predictor of the odd samples $S_j^{(1)}(x, 2y + 1)$. After that, the update step aims at computing a coarser approximation $\tilde{S}_{j+1}^{(1)}$ of the original signal by smoothing the even sample $S_j^{(1)}(x, 2y)$ as follows:

$$\tilde{S}_{j+1}^{(1)}(x, y) = S_j^{(1)}(x, 2y) + \sum_{k \in \mathcal{U}_1^{(1)}} u_{j,k}^{(1)} \tilde{d}_{j+1}^{(1)}(x, y - k), \quad (4.6)$$

where the set $\mathcal{U}_1^{(1)}$ denotes the spatial support of the update operator whose coefficients

are $u_{j,k}^{(1)}$.

Decomposition of target signal

Once the reference signal $S^{(1)}$ is encoded in intra mode, the attention will be paid now to the target signal $S^{(2)}$. It is important to note that the main difference between a basic lifting scheme and the vector lifting scheme is that for the target signal $S^{(2)}$, the prediction step uses samples from itself and *also* their corresponding samples taken from the reference signal $S^{(1)}$.

As shown in Fig. A.5, a P-U-P structure is used for the target signal $S^{(2)}$. More precisely, a first intra-prediction step is applied to generate an intermediate detail signal $\check{d}_{j+1}^{(2)}$, which serves to compute the approximation signal $\tilde{S}_{j+1}^{(2)}$ through the update step. After that, an hybrid prediction is performed by exploiting *simultaneously* the intra and inter redundancies in order to compute the final detail signal $\tilde{d}_{j+1}^{(2)}$. Thus, the resulting decomposition implies the following equations:

$$\check{d}_{j+1}^{(2)}(x, y) = S_j^{(2)}(x, 2y + 1) - \sum_{k \in \mathcal{P}_j^{(2)}} p_{j,k}^{(2)} S_j^{(2)}(x, 2y - 2k), \quad (4.7)$$

$$\tilde{S}_{j+1}^{(2)}(x, y) = S_j^{(2)}(x, 2y) + \sum_{k \in \mathcal{U}_j^{(2)}} u_{j,k}^{(2)} \check{d}_{j+1}^{(2)}(x, y - k), \quad (4.8)$$

$$\tilde{d}_{j+1}^{(2)}(x, y) = \check{d}_{j+1}^{(2)}(x, y) - \left(\sum_{k \in \mathcal{Q}_j} q_{j,k} \tilde{S}_{j+1}^{(2)}(x, y - k) + \sum_{k \in \mathcal{P}_j^{(1,2)}} p_{j,k}^{(1,2)} S_j^{(1)}(x, 2y + 1 - k) \right) \quad (4.9)$$

where $\mathcal{P}_j^{(2)}$ (resp. $\mathcal{P}_j^{(1,2)}$) is the spatial support of the intra-signal (resp. inter-signals) whereas its weights are designated by $p_{j,k}^{(2)}$ (resp. $p_{j,k}^{(1,2)}$), and \mathcal{Q}_j (resp. $q_{j,k}$) is the support (resp. weights) of the second intra-signal predictor.

Since a separable decomposition has been considered, these steps are iterated on the columns y of the resulting subbands $\tilde{S}_{j+1}^{(1)}$, $\check{d}_{j+1}^{(1)}$, $\tilde{S}_{j+1}^{(2)}$ and $\check{d}_{j+1}^{(2)}$ in order to produce the approximation subbands $S_{j+1}^{(1)}$ and $S_{j+1}^{(2)}$ as well as three details subbands, for each signal, oriented horizontally, vertically and diagonally. This decomposition is again repeated on the approximation subbands over J resolution levels, yielding the multiresolution representation of the two input signals.

Finally, at the last resolution level J , instead of encoding the approximation subband of the target signal $S_J^{(2)}$, it is proposed to encode the residual subband given by:

$$e_J^{(2)}(x, y) = S_J^{(2)}(x, y) - \sum_{k \in \mathcal{P}_J^{(1,2)}} p_{J,k}^{(1,2)} S_J^{(1)}(x, y - k). \quad (4.10)$$

4.3 Proposed Compression Scheme based on VLS

4.3.1 Motivation

Since the interference patterns are generated from the wavefronts emanating from the same 3D object, the resulting holograms present similar visual contents. Thus, it is expected that these kinds of data show redundancies, and from this point of view, efficient hologram compression schemes can be designed by exploiting the dependencies between these patterns.

Moreover, most of the existing joint coding schemes, which have been developed in the literature for video and stereo/multiview data compression purpose, consist of two steps. First, one image (for example $S^{(1)}$) is selected as a reference image and encoded independently of the other one. Then, the second image $S^{(2)}$, selected as a target image, is predicted from the first one $S^{(1)}$, and the difference between the two images, called the residual, is encoded. Typically, DCT or DWT can be used for encoding both the reference and residual images [63, 64].

Contrary to this standard scheme, the main feature of VLS is that it does not generate a residual image, but two compact representations of the images $S^{(1)}$ and $S^{(2)}$. To this end, it is proposed here to apply the Vector Lifting concept to the phase-shifting holographic data.

4.3.2 Applied procedures

Procedure-1

The first method aims at encoding the shifted distance data $D^{(1)}$ and $D^{(2)}$. It has been noticed in Fig.3.1 that the obtained difference data presents visually similar patterns. To confirm this, Table 6.1 provides for some objects (shown in Fig. 4.3) the entropy measure [65] computed on the original image $D^{(2)}$, the residual one $D^{(2)} - D^{(1)}$, and the error resulting from a joint prediction similar to VLS, which is denoted in Table 6.1 by $D^{(2)} - Pred(D^{(1)}, D^{(2)})$. Thus, by generating the prediction error, the entropy has been decreased

which confirms the redundancies existing between $D^{(1)}$ and $D^{(2)}$. For this reason, it is proposed to encode $D^{(1)}$ and $D^{(2)}$ using VLS.

Table 4.1: Entropy measure on $D^{(2)}$, $D^{(2)} - D^{(1)}$ and $D^{(2)} - \text{Pred}(D^{(1)}, D^{(2)})$ of “Luigi-1”, “Luigi-2” and “Girl” objects

Objects	$D^{(2)}$	$D^{(2)} - D^{(1)}$	$D^{(2)} - \text{Pred}(D^{(1)}, D^{(2)})$
Luigi-1	27.32	27.31	23.65
Luigi-2	25.99	25.85	18.77
Girl	25.98	26.11	13.29

More precisely, $D^{(1)}$ will be encoded in intra-mode by using Eqs. A.6 and A.7 to compute the wavelet coefficients. To this end, a prediction and update filters with spatial supports $\mathcal{P}_j^{(1)} = \{-1, 0\}$ and $\mathcal{U}_j^{(1)} = \{0, 1\}$ are considered. In addition, the weights of the update filter are set for all the resolution levels to: $u_{j,0}^{(1)} = u_{j,1}^{(1)} = \frac{1}{4}$. However, it is proposed to optimize the prediction weights $p_{j,-1}^{(1)}$ and $p_{j,0}^{(1)}$ in order to design a coding scheme well adapted to the content of the hologram data. Since the detail coefficients can be viewed as prediction errors, the prediction filter coefficients can be optimized at each resolution level j by minimizing the variance of the detail signal $\tilde{d}_{j+1}^{(1)}$. More specifically, the well-known Yule-Walker equations are applied to solve the optimization problem:

$$\mathbf{E}[\mathbf{S}_j(x, y)\mathbf{S}_j(x, y)^\top]\mathbf{p}_j = \mathbf{E}[S_j^{(1)}(x, 2y + 1)\mathbf{S}_j(x, y)], \quad (4.11)$$

where

$$\mathbf{S}_j(x, y) = (S_j^{(1)}(x, 2y), S_j^{(1)}(x, 2y + 2))^\top \quad (4.12)$$

$\mathbf{p}_j = (p_{j,0}^{(1)}, p_{j,-1}^{(1)})^\top$ is the prediction weighting vector and $\mathbf{E}[\cdot]$ denotes the mathematical expectation.

Concerning the second signal $D^{(2)}$, the same intra-prediction and update filters used with $D^{(1)}$ will be employed to generate the signals $\check{d}_{j+1}^{(2)}$ and $\tilde{D}_{j+1}^{(2)}$. Then, the second prediction stage is performed by setting $\mathcal{Q}_j = \{-1, 0\}$ and $\mathcal{P}_j^{(1,2)} = \{-1, 0, 1\}$ for $j \in \{0, \dots, J-1\}$ and $\mathcal{P}_j^{(1,2)} = \{0\}$. The coefficients $q_{j,k}$ and $p_{j,k}^{(1,2)}$ are also optimized by minimizing the variance of the detail signal $\tilde{d}_{j+1}^{(2)}$ by Yule-Walker equations.

Procedure-2

In order to further confirm the similar characteristics between the shifted distance representation and real-imaginary representation, VLS is also applied to the real-imaginary data. Instead of encoding the real-imaginary data directly, the mathematical analysis between two representations is firstly explored.

Indeed, by further exploring the intensity information $I_H(x, y; \phi)$, it can be noticed that the third term of Eq. (2.2), $2|A_R||A_O|\cos(\varphi_R - \varphi_O)$, contains all effective information in the sense that the first and second terms of Eq. (2.2) will be eliminated during the subtraction operations in Eq. (3.1). Thus, by only retaining the third term, three signals can be defined as follows:

$$\begin{aligned} I^{(1)}(x, y) &= 2|A_R||A_O|\cos(0 - \varphi(x, y)) \\ &= 2|A_R||A_O|\cos(\varphi(x, y)) \end{aligned} \quad (4.13)$$

$$= 2|A_R|\text{real}(\widehat{U}_O(x, y)) \quad (4.14)$$

$$\begin{aligned} I^{(2)}(x, y) &= 2|A_R||A_O|\cos\left(\frac{\pi}{2} - \varphi(x, y)\right) \\ &= 2|A_R||A_O|\sin(\varphi(x, y)) \end{aligned} \quad (4.15)$$

$$= 2|A_R|\text{imag}(\widehat{U}_O(x, y)) \quad (4.16)$$

$$\begin{aligned} I^{(3)}(x, y) &= 2|A_R||A_O|\cos(\pi - \varphi(x, y)) \\ &= -I^{(1)}(x, y) \end{aligned} \quad (4.17)$$

Note that $D^{(1)}$ and $D^{(2)}$ given by Eq. (3.1) can be re-expressed as follows:

$$\begin{cases} D^{(1)}(x, y) = I^{(1)}(x, y) - I^{(2)}(x, y) \\ D^{(2)}(x, y) = I^{(1)}(x, y) + I^{(2)}(x, y) \end{cases} \quad (4.18)$$

Therefore, instead of encoding $D^{(1)}$ and $D^{(2)}$, one can also directly encode $I^{(1)}$ and $I^{(2)}$, which can be respectively considered as real and imaginary information, by using VLS. While the same spatial supports of the prediction and update filters used previously to encode $D^{(1)}$ and $D^{(2)}$ are considered, it is important to note that the prediction weights are re-optimized and adapted to the contents of $I^{(1)}$ and $I^{(2)}$.

Obviously, at the decoder side, the decoded images $\widehat{I}^{(1)}$ and $\widehat{I}^{(2)}$ are firstly determined for a given bitrate, and then, the associated difference signals used for the object wave

reconstruction can be deduced:

$$\begin{cases} \widehat{D}^{(1)}(x, y) = \widehat{I}^{(1)}(x, y) - \widehat{I}^{(2)}(x, y) \\ \widehat{D}^{(2)}(x, y) = \widehat{I}^{(1)}(x, y) + \widehat{I}^{(2)}(x, y) \end{cases} \quad (4.19)$$

It should be noted that the resulting distortions of $D^{(1)}$ and $D^{(2)}$ can be obtained from that of $I^{(1)}$ and $I^{(2)}$ as follows:

$$\begin{aligned} & \mathbf{E}\{(I^{(1)} - \widehat{I}^{(1)})^2\} + \mathbf{E}\{(I^{(2)} - \widehat{I}^{(2)})^2\} \\ &= \mathbf{E}\{(I^{(1)} - \frac{1}{2}(\widehat{D}^{(1)} + \widehat{D}^{(2)}))^2\} + \mathbf{E}\{(I^{(2)} - \frac{1}{2}(\widehat{D}^{(2)} - \widehat{D}^{(1)}))^2\} \\ &= \frac{1}{4} \left(\mathbf{E}\{(D^{(1)} + D^{(2)} - \widehat{D}^{(1)} - \widehat{D}^{(2)})^2\} + \mathbf{E}\{(D^{(2)} - D^{(1)} - \widehat{D}^{(2)} + \widehat{D}^{(1)})^2\} \right) \\ &= \frac{1}{2} \left(\mathbf{E}\{(D^{(1)} - \widehat{D}^{(1)})^2\} + \mathbf{E}\{(D^{(2)} - \widehat{D}^{(2)})^2\} \right) \end{aligned} \quad (4.20)$$

where $\mathbf{E}\{\cdot\}$ denotes the mathematical expectation.

4.4 Experimental results

4.4.1 Comparative study

In order to show the benefit of the proposed hologram compression scheme based on VLS, the following methods are considered:

- The first one corresponds to the state-of-the-art hologram compression method where the inputs $D^{(1)}$ and $D^{(2)}$ (or $I^{(1)}$ and $I^{(2)}$) are separately encoded by using existing still image coders [45]. To this end, JPEG2000 [29] is used in its lossy compression mode with the 9/7 wavelet transform. In what follows, these schemes will be designated by Independent-I (resp. Independent-II for the input $I^{(1)}$ and $I^{(2)}$)
- The second one is the standard joint coding scheme, explained at the beginning of Section 4.3, where a reference and a residual image are also encoded using JPEG2000 and the 9/7 transform. Note that this technique has been considered in most of joint coding schemes developed in the context of stereo and video data compression [64]. It will be designated by Standard-I for the inputs $D^{(1)}$ and $D^{(2)}$ (resp. Standard-II for $I^{(1)}$ and $I^{(2)}$).

- The third one corresponds to the proposed joint coding scheme based on the vector lifting concept, applied either to the pair of correlated differences $(D^{(1)}, D^{(2)})$ or to the pair $(I^{(1)}, I^{(2)})$. It will be designated by VLS-I (resp. VLS-II) when $D^{(1)}$ and $D^{(2)}$ (resp. $I^{(1)}$ and $I^{(2)}$) are encoded.

All these decompositions are carried out over three resolution levels. Simulations are performed on 6 virtual 3D objects which have been already illustrated in Fig. 4.3. The parameters used for generating holograms are the same as those in Table 2.1.

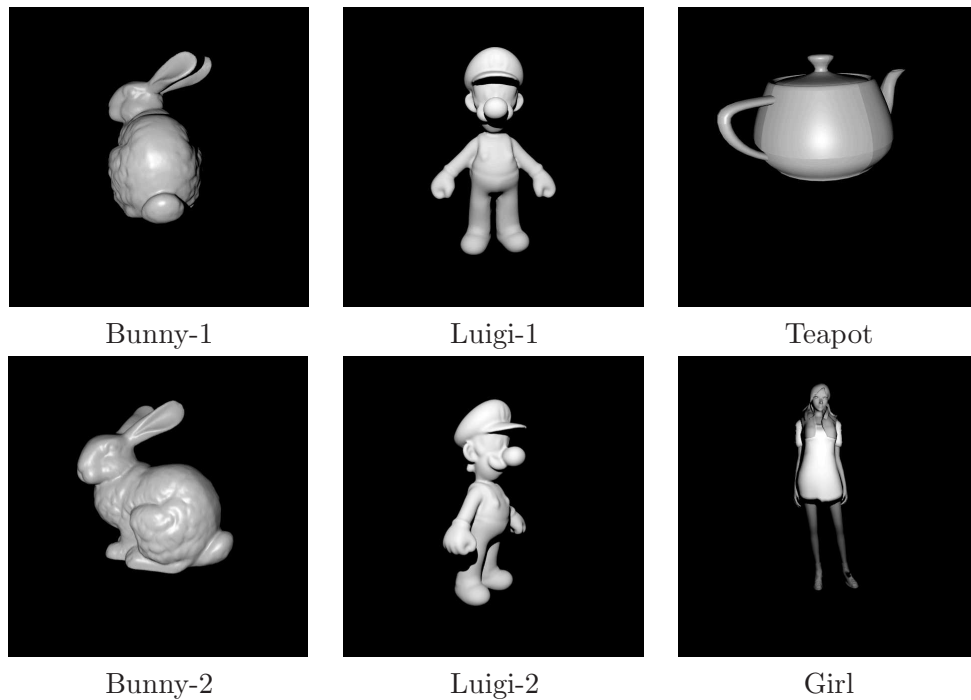


Figure 4.3: 3D test objects

4.4.2 Evaluations and discussions

Procedure-1

Entropy measurement

The entropy measurement introduced in Section 4.3.2, is indeed a good estimate of the coding performance of these different schemes as shown in Table 4.2. Different from Table 4.1, Table 4.2 evaluates the entropy measurement based on the wavelet

decomposition of data $D^{(2)}$ in Table 4.1. The decreased entropy obtained by VLS-I confirms the efficiency of VLS-I for predicting redundancies.

Table 4.2: Entropy measure of three different compression schemes on “Luigi-1”, “Luigi-2” and “Girl” objects

Objects	Independent-I	Standard-I	VLS-I
Luigi-1	21.14	20.82	17.98
Luigi-2	22.06	21.62	16.58
Girl	19.36	19.43	15.10

Rate-distortion

The first experiments have focused on the encoding of the difference data $D^{(1)}$ and $D^{(2)}$. The distortion is assessed in terms of the standard PSNR criterion as well as the perceptual metric SSIM [66] of the reconstructed 3D object. Figures 4.4 and 4.5 illustrate the rate-distortion results in terms of PSNR and SSIM versus the bitrate given in bit per pixel (bpp). It can be firstly noticed that the standard scheme is less performant than the conventional independent scheme where the inputs are independently encoded. This may explain the fact that residual-based coding methods have not been reported earlier, and it has been preferred to encode separately each pattern.

Apparently, the proposed coding method based on VLS outperforms the two other methods. Compared to the standard coding scheme (resp. the independent one), the PSNR and SSIM improvements range from 2-4 dB (resp. 1-2 dB) and 0.2-0.3 (resp. 0.1-0.2). However, it can be noted that there are some unexpected trend on the SSIM curves of standard scheme and independent scheme. One reason can be considered after observing the reconstructed images (e.g., Figures 5.4 (a) and (b)). When the bitrate is low, there are some bright patterns appearing in the reconstructed images, where they are dark in the originally reconstructed image. These bright patterns are not predictable and they badly influence the SSIM measurement of the full size reconstructed image.

Visual Quality

Figures (5.4)-(4.9) display some reconstructed objects at different bitrates. It can be observed that VLS leads to the best visual quality of the reconstruction. Meanwhile, the unpredictable bright patterns can be observed from the reconstructed images by

independent scheme and standard scheme.

Procedure-2

Entropy measurement

The entropy measurement based on the wavelet decomposition of data $I^{(2)}$ is obtained in Table 4.3. The results obtained from three schemes are similar to the measurements on data $D^{(2)}$

Table 4.3: Entropy measure of three different compression schemes on “Luigi-1”, “Luigi-2” and “Girl” objects

Objects	Independent-II	Standard-II	VLS-II
Luigi-1	20.82	21.04	17.60
Luigi-2	21.63	21.34	16.16
Girl	19.43	19.09	15.14

Rate-distortion

The second strategy which aims at encoding $I^{(1)}$ and $I^{(2)}$ instead of $D^{(1)}$ and $D^{(2)}$ has also been tested. In this case, the resulting PSNR and SSIM of the reconstructed objects are given in Figures 4.10 and 4.11. By comparing these results to those obtained in Figures 4.4 and 4.5, it can be deduced that encoding the pairs $(D^{(1)}, D^{(2)})$ and $(I^{(1)}, I^{(2)})$ lead generally to similar performance. It confirms the similar characteristics between shifted distance representation and real-imaginary representation.

Above all, it confirms the effectiveness of the proposed joint coding scheme based on separable VLS for holographic data compression purposes.

4.5 Conclusion

In this chapter, the work has been devoted to the compression of phase-shifting holographic data, more precisely, the shifted distance information and the real-imaginary information. To this end, due to the great advantages of lifting schemes, a new joint multiscale decomposition based on the separable vector lifting concept has been developed. Moreover, the proposed coding scheme has been adapted to the contents of the holographic data.

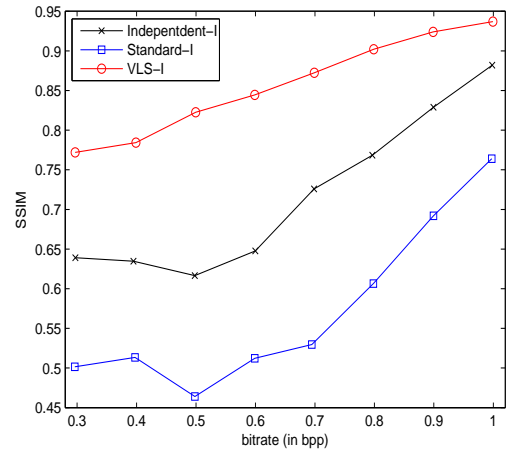
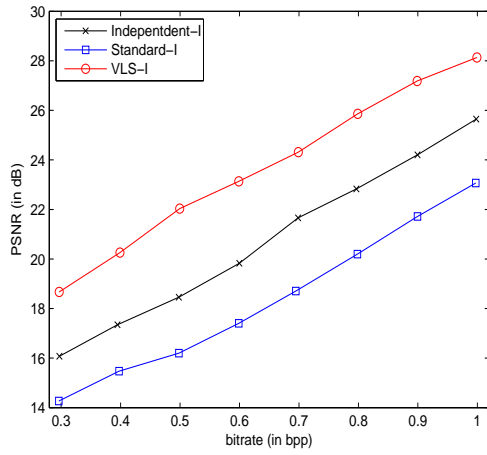
Experimental results have indicated the good performance of the proposed approach over the conventional ones in terms of quality of the reconstructed 3D object. A significant

gain of about 2 dB and 0.15 in terms of PSNR and SSIM, respectively, has been achieved compared to the state-of-the-art independent coding scheme.

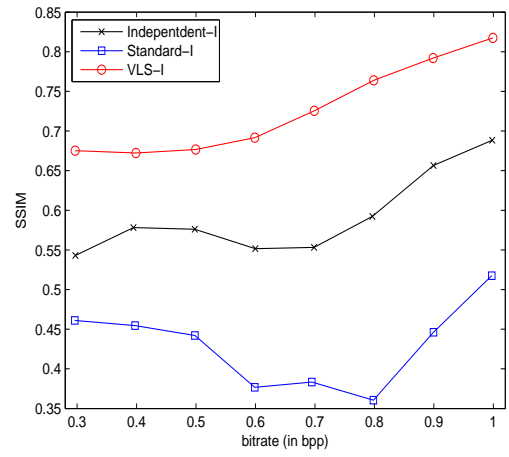
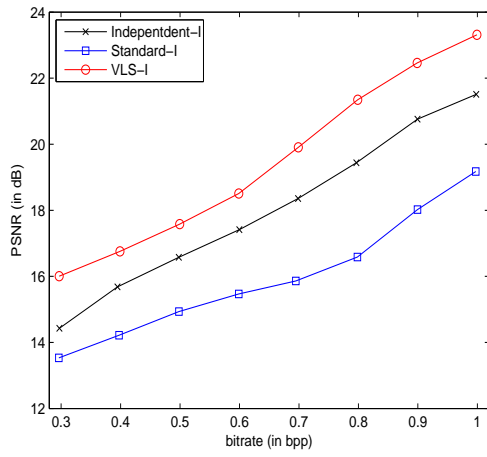
It is worth pointing out that the developed VLS has been performed in a separable way by cascading the 1D decomposition along the horizontal direction, then along the vertical direction. However, according to the visual patterns of the difference data $D^{(1)}$ and $D^{(2)}$, it can be noticed that these signals present some structures (similar to the propagation of waves) which are neither horizontal nor vertical. Thus, it would be interesting to develop a non separable decomposition to better exploit the characteristics of the hologram data.

The research work reported in this chapter has led to this publication:

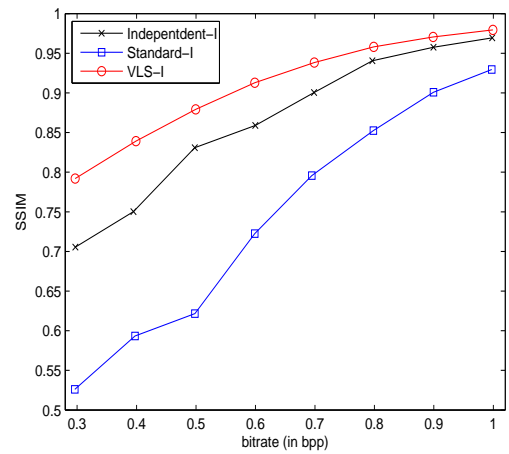
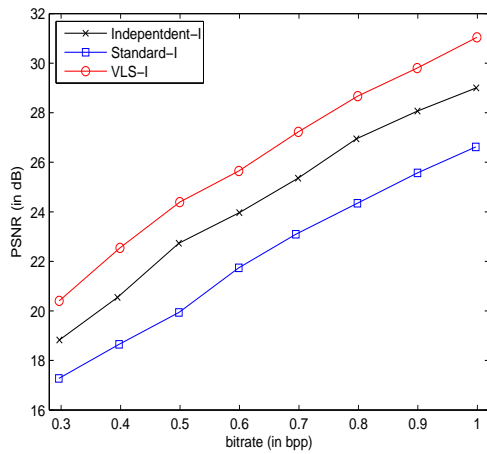
- Y. Xing, M. Kaaniche, B. Pesquet-Popescu, and F. Dufaux, “Vector lifting scheme for phase-shifting holographic data compression,” *Optical Engineering, Special issue on Practical Holography: New Procedures, Materials, and Applications*, 53(11), 2014.



(a)

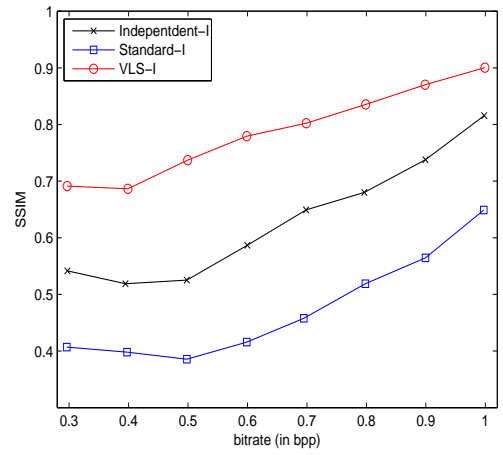
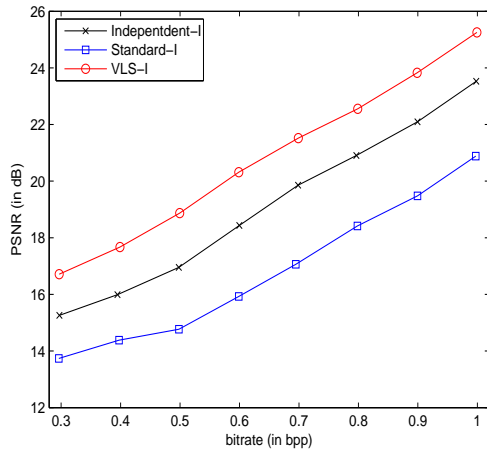


(b)

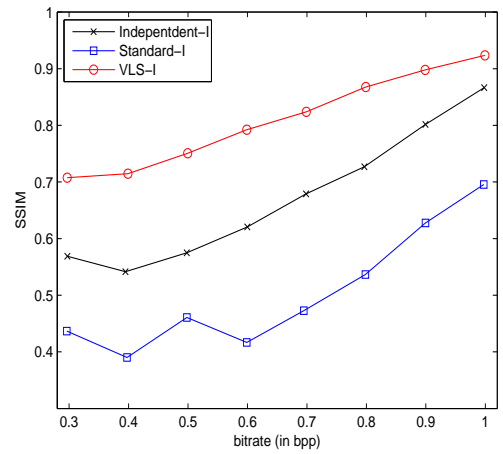
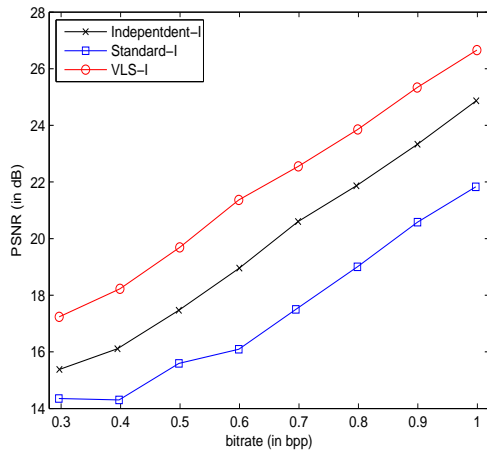


(c)

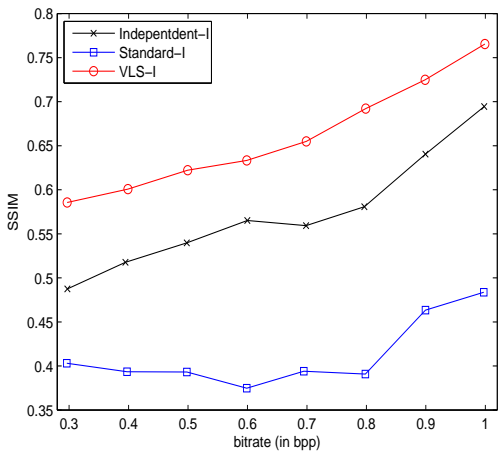
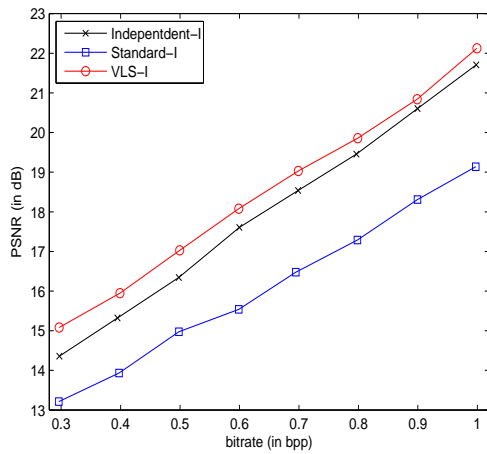
Figure 4.4: Rate-distortion performance of the different hologram compression schemes applied on $D^{(1)}$ and $D^{(2)}$ for the objects: (a) “Bunny-1”, (b) “Bunny-2”, (c) “Girl”.



(a)

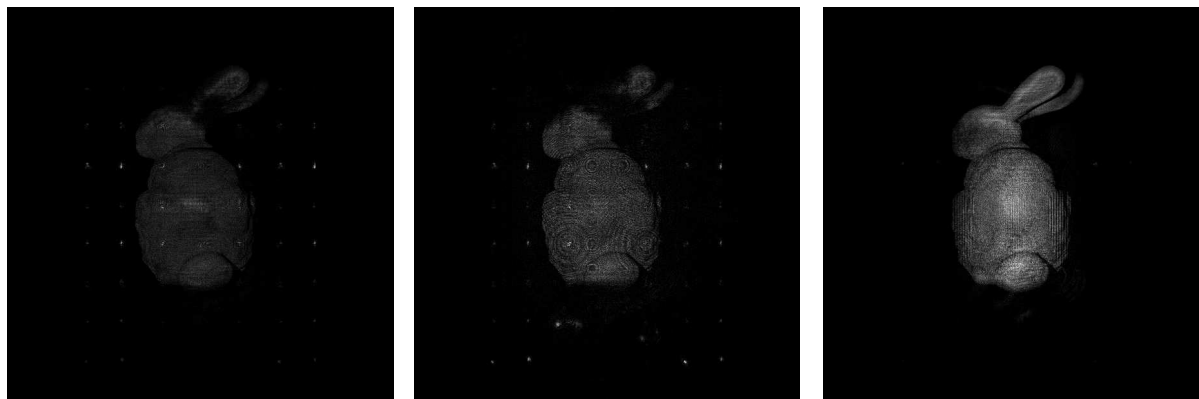


(b)



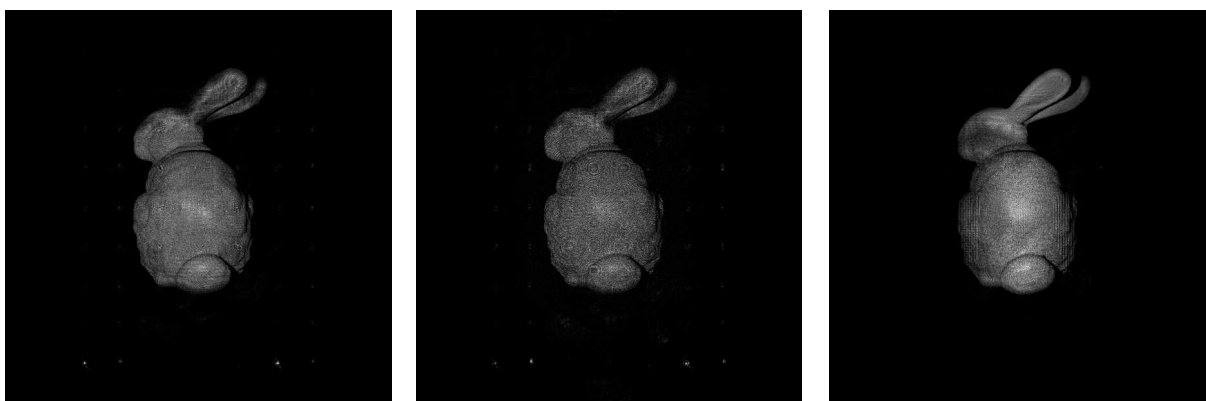
(c)

Figure 4.5: Rate-distortion performance of the different hologram compression schemes applied on $D^{(1)}$ and $D^{(2)}$ for the objects: (a) “Luigi-1”, (b) “Luigi-2”, (c) “Teapot”.



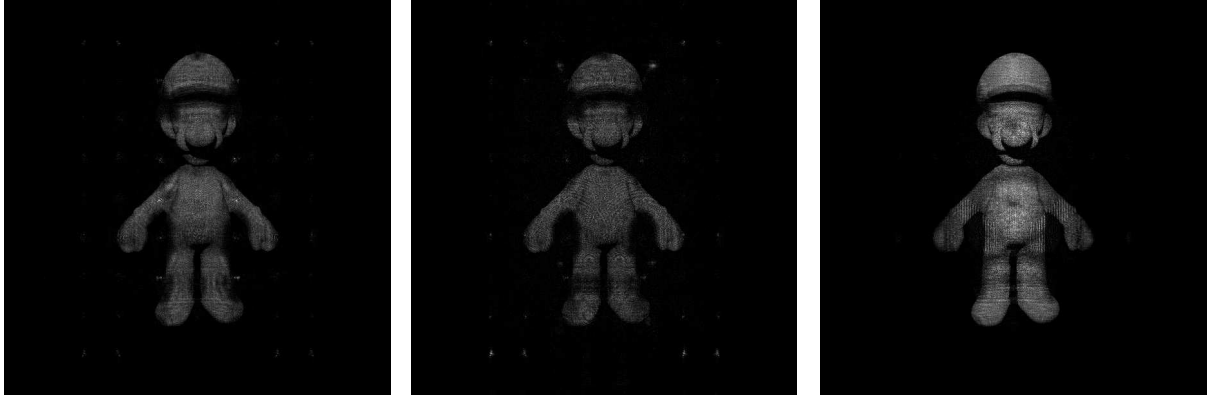
(a) PSNR=18.45 dB, SSIM=0.61 (b) PSNR=16.19 dB, SSIM=0.46 (c) PSNR=22.03 dB, SSIM=0.82

Figure 4.6: Reconstructed “Bunny-1” object at 0.5 bpp using: (a) Independent-I, (b) Standard-I, (c) VLS-I.



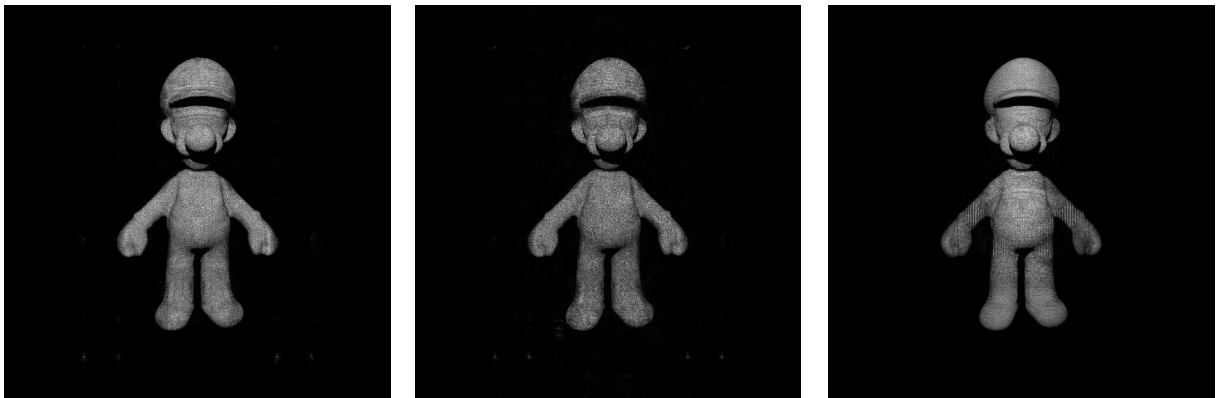
(a) PSNR=21.65 dB, SSIM=0.72 (b) PSNR=18.70 dB, SSIM=0.52 (c) PSNR=24.32 dB, SSIM=0.87

Figure 4.7: Reconstructed “Bunny-1” object at 0.7 bpp using: (a) Independent-I, (b) Standard-I, (c) VLS-I.



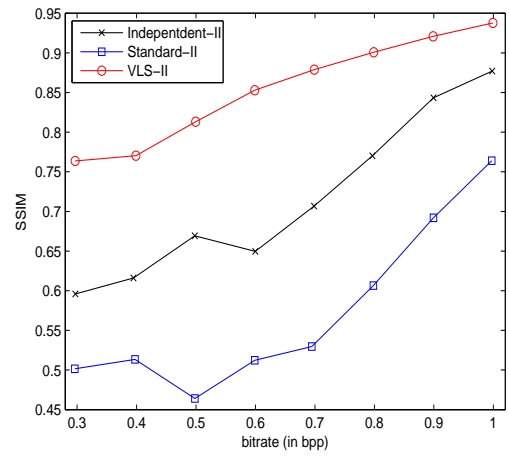
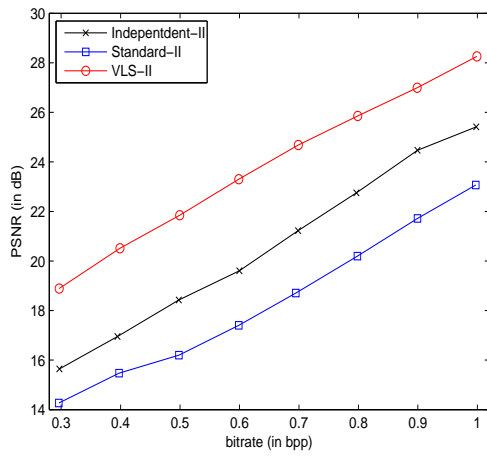
(a) PSNR=18.43 dB, SSIM=0.59 (b) PSNR=15.93 dB, SSIM=0.42 (c) PSNR=20.31 dB, SSIM=0.78

Figure 4.8: Reconstructed “Luigi-1” object at 0.6 bpp using: (a) Independent-I, (b) Standard-I, (c) VLS-I.

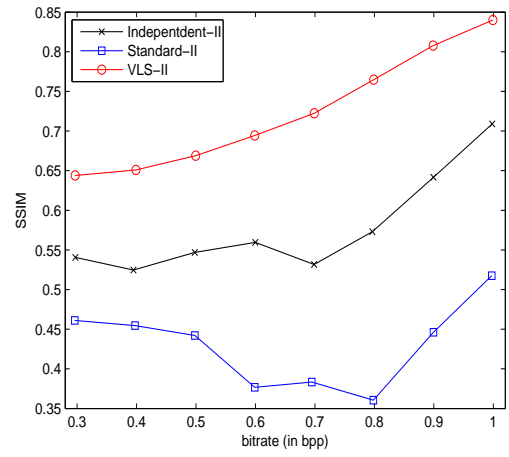
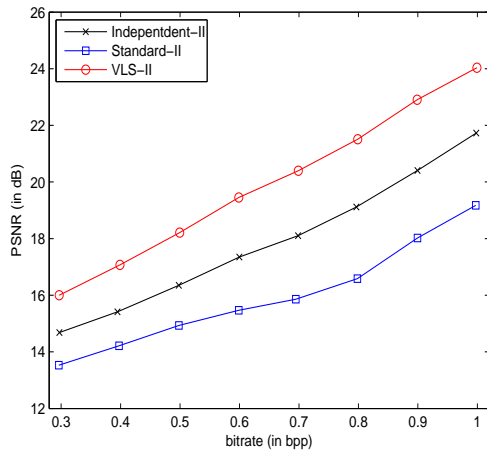


(a) PSNR=22.10 dB, SSIM=0.74 (b) PSNR=19.48 dB, SSIM=0.56 (c) PSNR=23.83 dB, SSIM=0.87

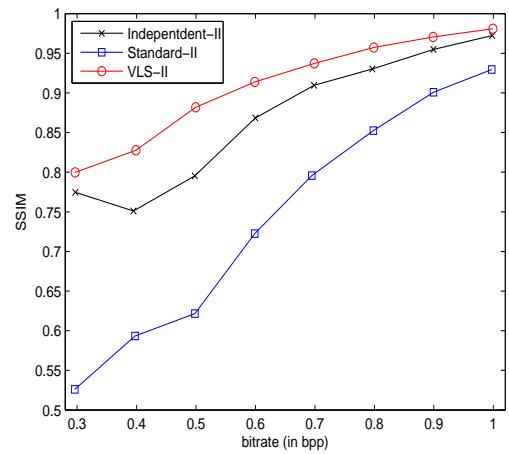
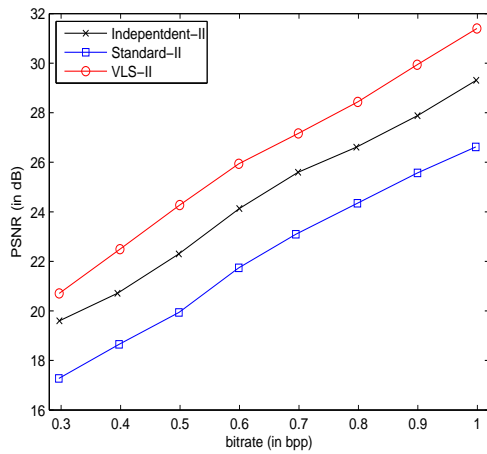
Figure 4.9: Reconstructed “Luigi-1” object at 0.9 bpp using: (a) Independent-I, (b) Standard-I, (c) VLS-I.



(a)

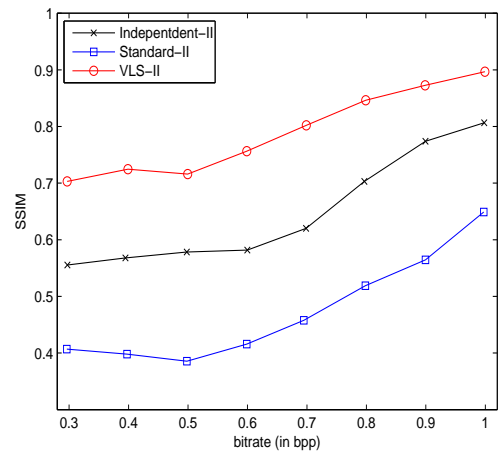
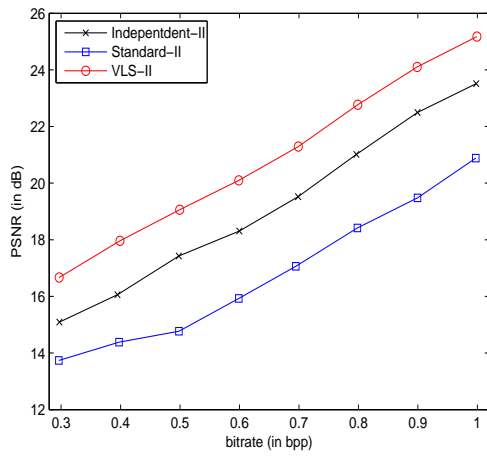


(b)

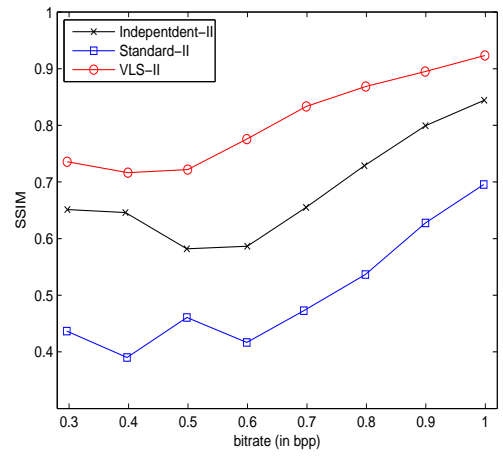
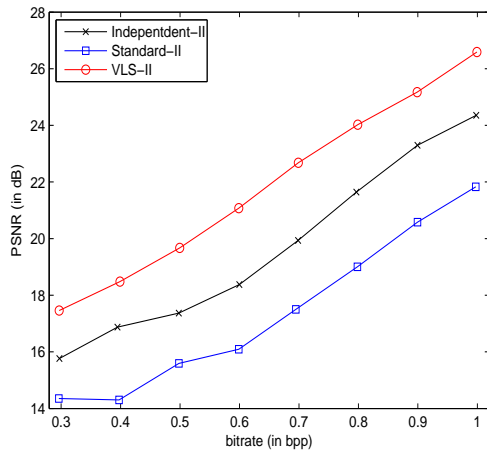


(c)

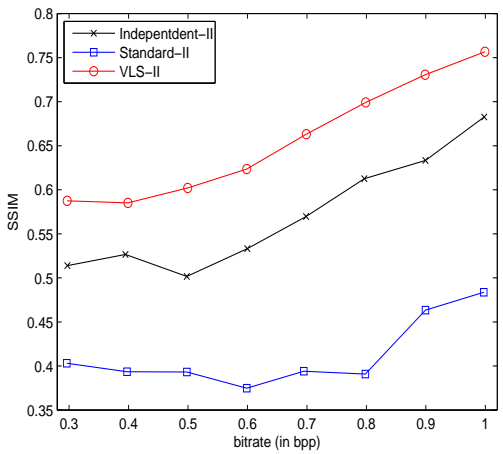
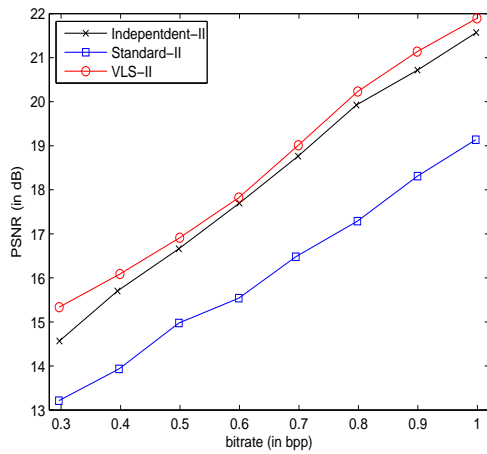
Figure 4.10: Rate-distortion performance of the different hologram compression schemes applied on $I^{(1)}$ and $I^{(2)}$ for the objects: (a) “Bunny-1”, (b) “Bunny-2”, (c) “Girl”.



(a)



(b)



(c)

Figure 4.11: Rate-distortion performance of the different hologram compression schemes applied on $I^{(1)}$ and $I^{(2)}$ for the objects: (a) “Luigi-1”, (b) “Luigi-2”, (c) “Teapot”.

Chapter 5

Non Separable Vector Lifting Scheme on Digital Phase-shifting Holographic Data

5.1 Introduction

In the last chapter, the compression of phase-shifting holographic data has been investigated by using separable VLS. However, the separable structures may not be very efficient for coping with 2D images which contains contours neither horizontal nor vertical. Thus, we propose in this chapter to use 2D non separable vector lifting schemes (NS-VLS) for further investigation. More precisely, except the adaption of the decomposition structures, the optimization of all the operators, including the prediction and update ones, are focused on building a content-adaptive decomposition.

This chapter is organized as follows. In Section 5.2, the decomposition of the 2D NS-VLS is presented with the application to the holographic data of shifted distance representation. Then, the design problems of both prediction and update operators are described in Section 5.3, including the optimization techniques, the definition of the spatial supports and the transmission cost analysis of the filter coefficients. Experimental results are given in Section 5.4 and some conclusions are drawn in Section 5.5.

5.2 Proposed compression scheme based on NS-VLS

5.2.1 Motivation

It is important to note that, in Chapter 4, the decomposition is handled in a separable manner by simply applying a 1D-VLS along the lines, then along the columns of the holographic data. However, according to the visual content of the generated patterns, the input images of the holographic information, either the shifted distance one or real-imaginary one, present rather isotropic structures. Therefore, the previous developed separable VLS is not optimal, and it becomes more important to design a non separable decomposition, designated in what follows by NS-VLS, in order to better exploit the two-dimensional (2D) wave characteristics of the holographic data. Moreover, due to the further confirmed similar characteristics between the shifted distance information and real-imaginary information, the performance of NS-VLS is only investigated with the shifted distance information.

5.2.2 Principle of NS-VLS decomposition

Since the decomposition is still based on the concept of a multiresolution transform, the description of NS-VLS is also given at a given resolution level j . Note that $j = 0$ corresponds to the initial images $D^{(1)}$ and $D^{(2)}$ (i.e the full resolution of shifted distance information). In the following, $D_j^{(1)}$ and $D_j^{(2)}$ designate the approximation coefficients of $D^{(1)}$ and $D^{(2)}$ at each resolution level j and have the dimensions of the initial images divided by 2^j along the horizontal and vertical dimensions. Moreover, at each pixel location (x, y) , the approximation coefficients of the first (resp. second) image $D_j^{(1)}(x, y)$ (resp. $D_j^{(2)}(x, y)$) are divided into four polyphase components denoted by

$$\begin{cases} D_{0,j}^{(i)}(x, y) = D_j^{(i)}(2x, 2y), \\ D_{1,j}^{(i)}(x, y) = D_j^{(i)}(2x, 2y + 1), \\ D_{2,j}^{(i)}(x, y) = D_j^{(i)}(2x + 1, 2y), \\ D_{3,j}^{(i)}(x, y) = D_j^{(i)}(2x + 1, 2y + 1) \end{cases} \quad (5.1)$$

where $i \in \{1, 2\}$.

Fig. A.6 illustrates the NS-VLS analysis structure. As shown in Fig. A.6, one image (here $D^{(1)}$) is selected as a reference image and encoded independently of the other one. To this end, a classical non separable lifting structure [67], composed of three prediction steps and

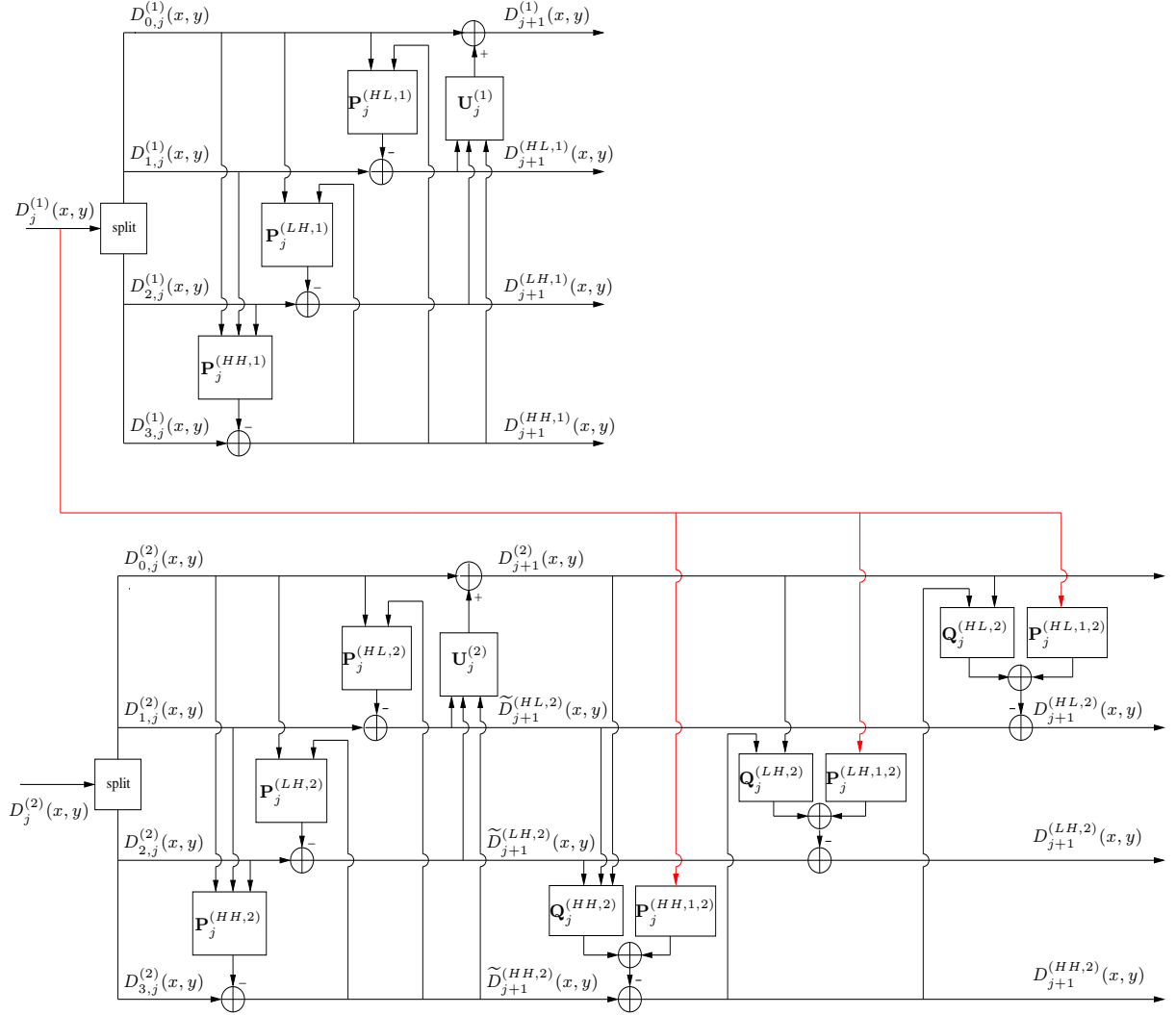


Figure 5.1: Proposed NS-VLS decomposition structure.

an update one, is applied to $D_j^{(1)}$ in order to generate the detail signals oriented diagonally $D_{j+1}^{(HH,1)}$, vertically $D_{j+1}^{(LH,1)}$ and horizontally $D_{j+1}^{(HL,1)}$, as well as the approximation one $D_{j+1}^{(1)}$. Thus, the output wavelet coefficients, at the resolution level $(j + 1)$, can be written as follows:

$$D_{j+1}^{(HH,1)}(x, y) = D_{3,j}^{(1)}(x, y) - \left((\mathbf{P}_{0,j}^{(HH,1)})^\top \mathbf{D}_{0,j}^{(HH,1)} + (\mathbf{P}_{1,j}^{(HH,1)})^\top \mathbf{D}_{1,j}^{(HH,1)} + (\mathbf{P}_{2,j}^{(HH,1)})^\top \mathbf{D}_{2,j}^{(HH,1)} \right), \quad (5.2)$$

$$D_{j+1}^{(LH,1)}(x, y) = D_{2,j}^{(1)}(x, y) - \left((\mathbf{P}_{0,j}^{(LH,1)})^\top \mathbf{D}_{0,j}^{(LH,1)} + (\mathbf{P}_{1,j}^{(LH,1)})^\top \underline{\mathbf{D}}_{j+1}^{(HH,1)} \right), \quad (5.3)$$

$$D_{j+1}^{(HL,1)}(x, y) = D_{1,j}^{(1)}(x, y) - \left((\mathbf{P}_{0,j}^{(HL,1)})^\top \mathbf{D}_{0,j}^{(HL,1)} + (\mathbf{P}_{1,j}^{(HL,1)})^\top \overline{\mathbf{D}}_{j+1}^{(HH,1)} \right), \quad (5.4)$$

$$D_{j+1}^{(1)}(x, y) = D_{0,j}^{(1)}(x, y) + \left((\mathbf{U}_{0,j}^{(HL,1)})^\top \mathbf{D}_{j+1}^{(HL,1)} + (\mathbf{U}_{1,j}^{(LH,1)})^\top \mathbf{D}_{j+1}^{(LH,1)} + (\mathbf{U}_{2,j}^{(HH,1)})^\top \mathbf{D}_{j+1}^{(HH,1)} \right), \quad (5.5)$$

where for every $i \in \{0, 1, 2\}$ and $o \in \{HL, LH, HH\}$,

- $\mathbf{P}_{i,j}^{(o,1)} = (p_{i,j}^{(o,1)}(s, t))_{(s,t) \in \mathcal{P}_{i,j}^{(o,1)}}$ represents the prediction weighting vector whose support is denoted by $\mathcal{P}_{i,j}^{(o,1)}$.
- $\mathbf{D}_{i,j}^{(o,1)} = (D_{i,j}^{(1)}(x + s, y + t))_{(s,t) \in \mathcal{P}_{i,j}^{(o,1)}}$ is a reference vector used to compute $D_{j+1}^{(o,1)}(x, y)$.
- $\underline{\mathbf{D}}_{j+1}^{(HH,1)} = (D_{j+1}^{(HH,1)}(x + s, y + t))_{(s,t) \in \mathcal{P}_{1,j}^{(LH,1)}}$ and $\overline{\mathbf{D}}_{j+1}^{(HH,1)} = (D_{j+1}^{(HH,1)}(x + s, y + t))_{(s,t) \in \mathcal{P}_{1,j}^{(HL,1)}}$ correspond to two reference vectors used in the second and the third prediction steps, respectively.
- $\mathbf{U}_{i,j}^{(o,1)} = (u_{i,j}^{(o,1)}(s, t))_{(s,t) \in \mathcal{U}_{i,j}^{(o,1)}}$ is the update vector coefficients whose support is designated by $\mathcal{U}_{i,j}^{(o,1)}$.
- $\mathbf{D}_{j+1}^{(o,1)} = (D_{j+1}^{(o,1)}(x + s, y + t))_{(s,t) \in \mathcal{U}_{i,j}^{(o,1)}}$ is the reference vector containing the set of detail samples used in the update step.

For the second image $D_j^{(2)}$, selected as a target one, a joint wavelet decomposition is performed by taking into account its correlation with the reference one $D_j^{(1)}$. More specifically, a lifting structure, similar to that used with $D_j^{(1)}$, is firstly applied on $D_j^{(2)}$ in order to produce three intermediate detail signals $\tilde{D}_{j+1}^{(HH,2)}$, $\tilde{D}_{j+1}^{(LH,2)}$ and $\tilde{D}_{j+1}^{(HL,2)}$, which will be used to compute the approximation coefficients $D_{j+1}^{(2)}$. Then, a second prediction stage is added.

Indeed, three hybrid prediction steps, which aim at exploiting simultaneously the intra and inter-image redundancies, are applied in order to generate the final detail coefficients $D_{j+1}^{(HH,2)}$, $D_{j+1}^{(LH,2)}$ and $D_{j+1}^{(HL,2)}$. Therefore, compared to a classical lifting structure, the main feature of a VLS concerns the prediction step which uses samples from the same image $D_j^{(2)}$ and also their corresponding ones taken from the reference one $D_j^{(1)}$. Thus, the final detail

wavelet coefficients, at the resolution level $(j + 1)$, are expressed as follows:

$$\begin{aligned}
D_{j+1}^{(HH,2)}(x, y) &= \tilde{D}_{j+1}^{(HH,2)}(x, y) - \left((\mathbf{Q}_{0,j}^{(HH,2)})^\top \tilde{\mathbf{D}}_{0,j+1}^{(HH,2)} \right. \\
&\quad + (\mathbf{Q}_{1,j}^{(HH,2)})^\top \tilde{\mathbf{D}}_{1,j+1}^{(HH,2)} + (\mathbf{Q}_{2,j}^{(HH,2)})^\top \tilde{\mathbf{D}}_{2,j+1}^{(HH,2)} \\
&\quad + (\mathbf{P}_{0,j}^{(HH,1,2)})^\top \mathbf{D}_{0,j}^{(HH,1)} + (\mathbf{P}_{1,j}^{(HH,1,2)})^\top \mathbf{D}_{1,j}^{(HH,1)} \\
&\quad \left. + (\mathbf{P}_{2,j}^{(HH,1,2)})^\top \mathbf{D}_{2,j}^{(HH,1)} + (\mathbf{P}_{3,j}^{(HH,1,2)})^\top \mathbf{D}_{3,j}^{(HH,1)} \right), \tag{5.6}
\end{aligned}$$

$$\begin{aligned}
D_{j+1}^{(LH,2)}(x, y) &= \tilde{D}_{j+1}^{(LH,2)}(x, y) - \left((\mathbf{Q}_{0,j}^{(LH,2)})^\top \tilde{\mathbf{D}}_{0,j+1}^{(LH,2)} \right. \\
&\quad + (\mathbf{Q}_{1,j}^{(LH,2)})^\top \tilde{\mathbf{D}}_{1,j+1}^{(LH,2)} + (\mathbf{P}_{0,j}^{(LH,1,2)})^\top \mathbf{D}_{0,j}^{(LH,1)} \\
&\quad \left. + (\mathbf{P}_{2,j}^{(LH,1,2)})^\top \mathbf{D}_{2,j}^{(LH,1)} \right), \tag{5.7}
\end{aligned}$$

$$\begin{aligned}
D_{j+1}^{(HL,2)}(x, y) &= \tilde{D}_{j+1}^{(HL,2)}(x, y) - \left((\mathbf{Q}_{0,j}^{(HL,2)})^\top \tilde{\mathbf{D}}_{0,j+1}^{(HL,2)} \right. \\
&\quad + (\mathbf{Q}_{1,j}^{(HL,2)})^\top \tilde{\mathbf{D}}_{1,j+1}^{(HL,2)} + (\mathbf{P}_{0,j}^{(HL,1,2)})^\top \mathbf{D}_{0,j}^{(HL,1)} \\
&\quad \left. + (\mathbf{P}_{1,j}^{(HL,1,2)})^\top \mathbf{D}_{1,j}^{(HL,1)} \right), \tag{5.8}
\end{aligned}$$

where for every $i \in \{0, 1, 2, 3\}$ and $o \in \{HL, LH, HH\}$,

- $\mathbf{Q}_{i,j}^{(o,2)} = (q_{i,j}^{(o,2)}(s, t))_{(s,t) \in \mathcal{Q}_{i,j}^{(o,2)}}$ is the intra prediction weighting vector whose support is designated by $\mathcal{Q}_{i,j}^{(o,2)}$
- $\mathbf{P}_{i,j}^{(o,1,2)} = (p_{i,j}^{(o,1,2)}(s, t))_{(s,t) \in \mathcal{P}_{i,j}^{(o,1,2)}}$ is the hybrid prediction weighting vector whose support is denoted by $\mathcal{P}_{i,j}^{(o,1,2)}$
- $\tilde{\mathbf{D}}_{0,j+1}^{(o,2)} = (D_{j+1}^{(2)}(x + s, y + t))_{(s,t) \in \mathcal{Q}_{0,j}^{(o,2)}}$ is a reference vector containing the approximation coefficients $D_{j+1}^{(2)}$ used to compute the detail ones $D_{j+1}^{(o,2)}(x, y)$
- $\tilde{\mathbf{D}}_{1,j+1}^{(HH,2)} = (\tilde{D}_{j+1}^{(HL,2)}(x + s, y + t))_{(s,t) \in \mathcal{Q}_{1,j}^{(HH,2)}}$ and $\tilde{\mathbf{D}}_{2,j+1}^{(HH,2)} = (\tilde{D}_{j+1}^{(LH,2)}(x + s, y + t))_{(s,t) \in \mathcal{Q}_{2,j}^{(HH,2)}}$ are two reference vectors, containing respectively the intermediate detail coefficients $\tilde{D}_{j+1}^{(HL,2)}$ and $\tilde{D}_{j+1}^{(LH,2)}$, used to compute the final detail coefficients $D_{j+1}^{(HH,2)}(x, y)$
- $\underline{\mathbf{D}}_{j+1}^{(HH,2)} = (D_{j+1}^{(HH,2)}(x + s, y + t))_{(s,t) \in \mathcal{Q}_{1,j}^{(LH,2)}}$ and $\overline{\mathbf{D}}_{j+1}^{(HH,2)} = (D_{j+1}^{(HH,2)}(x + s, y + t))_{(s,t) \in \mathcal{Q}_{1,j}^{(HL,2)}}$ are two intra prediction vectors used to compute $D_{j+1}^{(LH,2)}(x, y)$ and $D_{j+1}^{(HL,2)}(x, y)$
- $\mathbf{D}_{i,j}^{(o,1)} = (D_{i,j}^{(1)}(x + s, y + t))_{(s,t) \in \mathcal{P}_{i,j}^{(o,1,2)}}$ is a vector containing some samples of the reference image $D_j^{(1)}$ used to exploit the inter-image redundancies during the computation of the final

detail coefficients $D_{j+1}^{(o,2)}(x, y)$.

By repeating the same decomposition strategy on the approximation subbands over J resolution levels, two multiresolution representations of $D^{(1)}$ and $D^{(2)}$ are obtained. Finally, at the last resolution level J , instead of encoding the approximation subband of the target image $D_J^{(2)}$, it would be interesting to exploit its correlation with $D_J^{(1)}$ and thus to encode the following residual subband $e_J^{(2)}$:

$$e_J^{(2)}(x, y) = D_J^{(2)}(x, y) - p_J^{(1,2)} D_J^{(1)}(x, y). \quad (5.9)$$

where $p_J^{(1,2)}$ is an hybrid prediction coefficient that exploits the correlation between $D_J^{(2)}$ and $D_J^{(1)}$.

5.3 Design of prediction and update filters

5.3.1 Optimization techniques

For the same reason as the VLS-based approach, the ultimate aim is to design an NS-VLS-based decomposition well adapted to the characteristics of the holographic data. Consequently, the optimization of all the operators is necessary. Due to the complexity of the NS-VLS structure, different strategies of optimization are applied:

Optimization of the predictors for $D^{(1)}$

For the first image $D^{(1)}$, the different prediction filters $\mathbf{P}_j^{(o,1)}$ (with $o \in \{HH, LH, HL\}$), used to generate the detail subbands $D_{j+1}^{(o,1)}$, are optimized at each resolution level by minimizing the variance of the detail coefficients. As mentioned before, the Yule-Walker equations should be satisfied.

Optimization of the update operators

Different from the fixed assignment of the update operators in separable VLS, the update filter here at each level is optimized by minimizing the error between the approximation coefficients $D_{j+1}^{(o,1)}$ and the decimated version of the signal resulting from an ideal low-pass filter. Due to the complexity of the equations for the application, the details will not be provided in this thesis. The readers can refer to [67] for more details.

Optimization of the operators for $D^{(2)}$

For the second image $D^{(2)}$, all the prediction and update operators can also be optimized by adopting the same strategy used with $D^{(1)}$. However, since $D^{(1)}$ and $D^{(2)}$ present similar content, the optimization process of the first three prediction filters $\mathbf{P}_j^{(o,2)}$ and the update one $\mathbf{U}_j^{(2)}$ can be omitted by imposing these operators to be equal to those obtained with $D^{(1)}$. Thus, we have:

$$\begin{aligned}\mathbf{P}_j^{(HH,2)} &= \mathbf{P}_j^{(HH,1)}, \mathbf{P}_j^{(LH,2)} = \mathbf{P}_j^{(LH,1)}, \\ \mathbf{P}_j^{(HL,2)} &= \mathbf{P}_j^{(HL,1)}, \mathbf{U}_j^{(2)} = \mathbf{U}_j^{(1)}.\end{aligned}\quad (5.10)$$

Note that this procedure presents the advantages of simplifying the optimization strategy and reducing the overhead cost corresponding to the number of filter coefficients that must be sent to the decoder. Finally, for the remaining hybrid prediction filters $\mathbf{P}_j^{(o,1,2)}$ and $\mathbf{Q}_j^{(o,2)}$, they will be optimized by minimizing the variance of the detail coefficients $D_{j+1}^{(o,2)}$.

5.3.2 Definition of the spatial supports

To apply the considered adaptive NS-VLS, the sets of spatial supports for the different prediction and update filters should be defined. To this end, it has been shown in [67] that a classical separable lifting structure with 1D prediction and update filters, of length L_p and L_u respectively (which often take even values), has an equivalent 2D structure similar to that shown in the top side of Fig. A.6 (i.e the block which is applied on $D^{(1)}$). More specifically, this results in choosing the following spatial supports of the prediction and update operators used with $D^{(1)}$:

$$\begin{aligned}\mathcal{P}_{0,j}^{(HH,1)} &= \{(s, t) \in \mathbf{Z}^2 \mid -\frac{L_p}{2} + 1 \leq s \leq \frac{L_p}{2} \\ &\quad \text{and} \quad -\frac{L_p}{2} + 1 \leq t \leq \frac{L_p}{2}\}\end{aligned}\quad (5.11)$$

$$\mathcal{P}_{1,j}^{(HH,1)} = \mathcal{P}_{0,j}^{(LH,1)} = \{(s, 0) \mid -\frac{L_p}{2} + 1 \leq s \leq \frac{L_p}{2}\} \quad (5.12)$$

$$\mathcal{P}_{2,j}^{(HH,1)} = \mathcal{P}_{0,j}^{(HL,1)} = \{(0, t) \mid -\frac{L_p}{2} + 1 \leq t \leq \frac{L_p}{2}\} \quad (5.13)$$

$$\mathcal{U}_{0,j}^{(HL,1)} = \mathcal{P}_{1,j}^{(LH,1)} = \{(0, t) \mid -\frac{L_u}{2} \leq t \leq \frac{L_u}{2} - 1\} \quad (5.14)$$

$$\mathcal{U}_{1,j}^{(LH,1)} = \mathcal{P}_{1,j}^{(HL,1)} = \{(s, 0) \mid -\frac{L_u}{2} \leq s \leq \frac{L_u}{2} - 1\} \quad (5.15)$$

$$\begin{aligned} \mathcal{U}_{2,j}^{(HH,1)} &= \{(s, t) \in \mathbf{Z}^2 \mid -\frac{L_u}{2} \leq s \leq \frac{L_u}{2} - 1 \\ &\text{and } -\frac{L_u}{2} \leq t \leq \frac{L_u}{2} - 1\} \end{aligned} \quad (5.16)$$

While the same spatial supports are used with the three intra-prediction filters $\mathcal{P}_{i,j}^{(o,2)}$ and the update one $\mathcal{U}_{i,j}^{(o,2)}$ thanks to (A.19), those of the remaining hybrid prediction operators are given by:

$$\mathcal{Q}_{0,j}^{(HH,2)} = \{(0, 0); (0, 1); (1, 0); (1, 1)\} \quad (5.17)$$

$$\mathcal{Q}_{1,j}^{(HH,2)} = \mathcal{Q}_{0,j}^{(LH,2)} = \{(0, 0); (1, 0)\} \quad (5.18)$$

$$\mathcal{Q}_{2,j}^{(HH,2)} = \mathcal{Q}_{0,j}^{(HL,2)} = \{(0, 0); (0, 1)\} \quad (5.19)$$

$$\begin{aligned} \mathcal{P}_{0,j}^{(HH,1,2)} &= \mathcal{P}_{0,j}^{(HH,1)}, \quad \mathcal{P}_{1,j}^{(HH,1,2)} = \mathcal{P}_{1,j}^{(HH,1)}, \\ \mathcal{P}_{2,j}^{(HH,1,2)} &= \mathcal{P}_{2,j}^{(HH,1)} \end{aligned} \quad (5.20)$$

$$\mathcal{P}_{1,j}^{(HL,1,2)} = \mathcal{P}_{2,j}^{(LH,1,2)} = \mathcal{P}_{3,j}^{(HH,1,2)} = \{(0, 0)\} \quad (5.21)$$

$$\mathcal{Q}_{1,j}^{(LH,2)} = \{(0, 0); (0, -1)\} \quad (5.22)$$

$$\mathcal{Q}_{1,j}^{(HL,2)} = \{(0, 0); (-1, 0)\} \quad (5.23)$$

$$\mathcal{P}_{0,j}^{(LH,1,2)} = \mathcal{P}_{0,j}^{(LH,1)}, \quad \mathcal{P}_{0,j}^{(HL,1,2)} = \mathcal{P}_{0,j}^{(HL,1)} \quad (5.24)$$

5.3.3 Transmission cost of the filter coefficients

Once the spatial supports are defined and the prediction and update coefficients are optimized, the latter must be transmitted to the decoder in order to proceed to the inverse transform and reconstruct the data $(D^{(1)}, D^{(2)})$. Knowing that the filter coefficients can be generally stored on 24 bits, the overhead cost related to the encoding of all the filter coefficients is given by:

$$o = \frac{L \times J \times 24}{2MN} \text{ bits per pixel (bpp)} \quad (5.25)$$

where L is the number of filter coefficients in the proposed NS-VLS, J is the number of resolution levels, and $M \times N$ is the size of the data.

According to the defined sets of the spatial prediction and update supports, it can be checked that the involved number of coefficients is:

$$L = 2L_p^2 + 8L_p + L_u^2 + 4L_u + 19. \quad (5.26)$$

For example, when $M = N = 600$ and $J = 3$, taking short length filters with parameters $L_p = 6$ and $L_u = 2$ results in a very small transmission cost equal to 0.015 bpp. However, this overhead becomes more important and reaches 0.233 bpp when $L_p = 32$ and $L_u = 2$.

5.4 Experimental results

5.4.1 Comparative study

In order to illustrate the efficiency of the proposed hologram coding scheme, its performance is compared with those methods applied in last chapter, using the same shifted distance data:

1. Similarly, the first one designated by ‘‘Independent’’, represents the coding method where the data are separately encoded by using the JPEG2000 standard with the 9/7 wavelet transform.
2. The second approach, denoted in what follows by ‘‘Standard’’ corresponds to the

standard joint coding scheme used often to exploit the inter-image redundancies in the context of stereo and video compression.

3. The third method corresponds to the separable VLS used in last chapter. Noted that, this decomposition, designated by SEP-VLS(2,2), is performed by using a prediction and an update filters of size 2 (i.e $L_p = L_u = 2$).
4. The proposed non separable extension of SEP-VLS(2,2) is denoted by NS-VLS(2,2). It should be noted that all these multiresolution coding schemes have been carried out over 3 resolution levels (i.e $J = 3$).
5. In addition, due to the advantages of the NS-VLS, we have also tested this decomposition with different prediction filter lengths L_p . Indeed, increasing L_p may be interesting for two reasons. The first one is explained by the fact that the holographic data presents repetitive circular structures similar to the propagation of waves. The second one is due to the objective of VLS which consists in exploiting the inter-images redundancies through the prediction stage. Thus, we propose in what follows to vary the length of the prediction filter while keeping the size of the update one fix (i.e $L_u = 2$). To this respect, in addition to the previous case given by $L_p = 2$, other cases with $L_p \in \{6, 12, 20, 32\}$ are also considered. Similarly to the notation NS-VLS(2,2), the new structures will be designated by NS-VLS(6,2), NS-VLS(12,2), NS-VLS(20,2) and NS-VLS(32,2).

5.4.2 Results of different encoding schemes

Rate-Distortion

All these methods are firstly compared in terms of Rate-Distortion (R-D) performance. Fig. 5.2 illustrates the PSNR of the reconstructed objects versus the bitrate given in bits per pixel (bpp). The obtained R-D curves show that the proposed NS-VLS-based method outperforms all the conventional coding schemes. For instance, compared to the SEP-VLS(2,2) decomposition, the proposed non separable one achieves an improvement of about 0.3 to 1 dB depending on the object.

Bjontegaard metric

Furthermore, the relative gain of NS-VLS(2,2) compared to SEP-VLS(2,2) has also been measured by Bjontegaard metric [68]. The results are given in Table 5.1 for bitrate range from 0.3 bpp to 1.0 bpp. It can be noticed that for a given quality of reconstruction, NS-VLS(2,2) outperforms SEP-VLS(2,2) up to 10% in terms of bitrate saving. Moreover, an improvement of up to 0.8 dB and 0.02 can be achieved in terms of PSNR and SSIM, respectively.

Table 5.1: The average PSNR, SSIM and bitrate saving gains of NS-VLS(2,2) with respect to SEP-VLS(2,2) using Bjontegaard metric.

Objects	bitrate saving (in %)	PSNR gain (in dB)	bitrate saving (in %)	SSIM gain
Bunny-1	-4.79	0.40	2.98	-0.004
Bunny-2	-9.33	0.62	4.20	-0.014
Luigi-1	-10.30	0.80	-9.59	0.026
Luigi-2	-5.26	0.43	-7.75	0.022
Girl	-3.13	0.30	-10.79	0.018
Teapot	-9.92	0.69	0.05	-0.0002

Visual quality

Moreover, Fig. 5.3 displays the examples of reconstructed “Luigi-1” object from different coding schemes and provides the quality of reconstruction in terms of PSNR and the perceptual criterion SSIM [66]. Some other examples of reconstructed “Bunny-1” object with lower bit rates are shown in Fig. 5.4. It is clear that the proposed NS-VLS(2,2) leads to better visual quality of reconstruction than the SEP-VLS(2,2).

5.4.3 Results of NS-VLS with different filter lengths

Rate-Distortion

Fig. 5.5 illustrates the R-D performance for different 3D objects. Compared to the case $L_p = 2$, it can be observed that increasing this length up to 12 or 20 leads to greatly improved compression performance. Indeed, an important gain of about 10 dB is achieved by NS-VLS(12,2) and NS-VLS(20,2) compared to NS-VLS(2,2). Moreover, it can be also

noticed that using very long filters ($L_p = 32$) leads to worse performance at low bitrate because of the expensive cost of encoding the filter coefficients compared to the case of small L_p values.

An example of R-D curves is also illustrated in Fig. 5.6, where the coding cost of filter coefficients is not taken into account. As expected, it can be seen in this case that NS-VLS(32,2) becomes more performant and have R-D results close to that obtained by NS-VLS(20,2).

Bjontegaard metric

Finally, the Bjontegaard metric results shown in Table 5.2 and 5.3 demonstrate also the interest of NS-VLS(12,2) and NS-VLS(20,2) compared to the NS-VLS(2,2), respectively. NS-VLS(12,2) slightly outperforms NS-VLS(20,2). Indeed, it shows a significant gain that reaches 80%, 12 dB and 0.29 in terms of bitrate saving, PSNR and SSIM, respectively.

Table 5.2: The average PSNR, SSIM and bitrate saving gains of NS-VLS(12,2) with respect to NS-VLS(2,2) using Bjontegaard metric.

Objects	bitrate saving (in %)	PSNR gain (in dB)	bitrate saving (in %)	SSIM gain
Bunny-1	-72.80	11.21	-66.89	0.13
Bunny-2	-78.84	12.22	-80.20	0.25
Luigi-1	-72.34	11.52	-68.96	0.18
Luigi-2	-74.33	11.78	-71.95	0.17
Girl	-69.18	8.55	-62.71	0.08
Teapot	-77.99	12.17	-89.34	0.29

Visual quality

Fig. 5.7 and Fig. 5.8 show the visual reconstruction quality of the object “Girl” at 0.6 bpp and “Teapot” at 0.8 bpp, respectively, using various NL-VLS schemes. Significant differences are quite visible. Therefore, a NS-VLS with an increased prediction filter length (e.g., 12 or 20) is very efficient for compressing shifted distance information.

All these results confirm the effectiveness of the proposed adaptive non separable VLS scheme for hologram compression purpose.

Table 5.3: The average PSNR, SSIM and bitrate saving gains of NS-VLS(20,2) with respect to NS-VLS(2,2) using Bjontegaard metric.

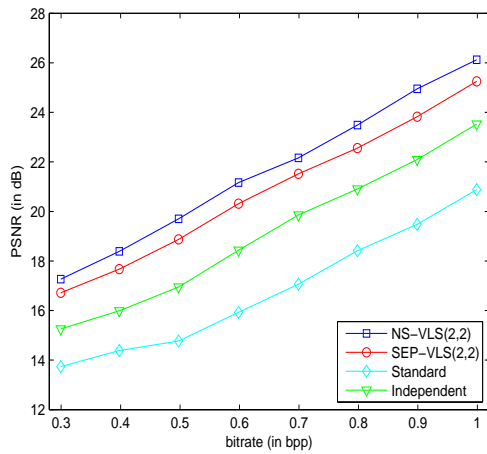
Objects	bitrate saving (in %)	PSNR gain (in dB)	bitrate saving (in %)	SSIM gain
Bunny-1	-70.81	11.21	-62.88	0.13
Bunny-2	-72.11	11.84	-69.46	0.24
Luigi-1	-70.92	11.49	-65.61	0.17
Luigi-2	-72.05	11.61	-65.18	0.16
Girl	-62.40	7.59	-52.95	0.07
Teapot	-75.51	12.23	-81.49	0.29

5.5 Conclusion

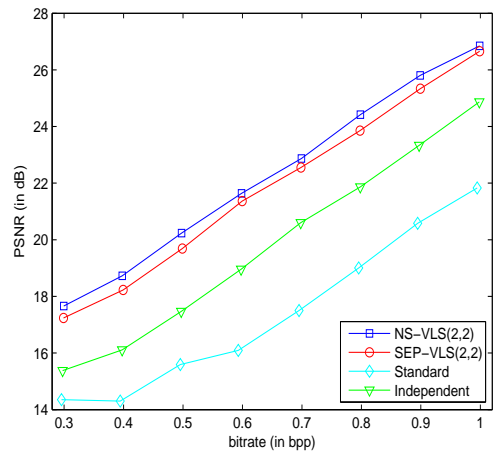
In this chapter, a non separable vector lifting scheme has been developed to encode the phase-shifting holographic information in order to better exploit the 2D isotropic characteristics of this data. Moreover, the proposed decomposition has been adapted to the data contents. Due to the particular structures of such data, it has been shown that increasing the prediction filter length results in a significant gain in terms of bitrate saving and visual quality of reconstruction.

The research work reported in this chapter has led to this publication:

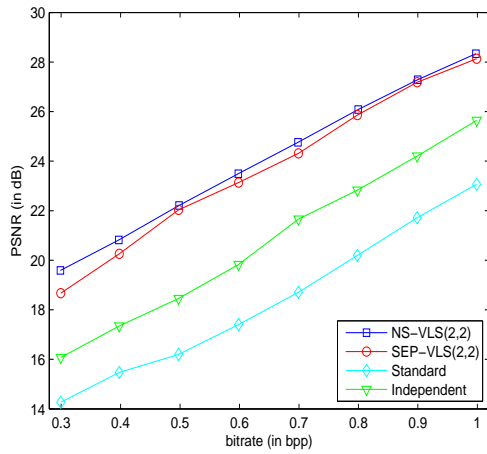
- Y. Xing, M. Kaaniche, B. Pesquet-Popescu, and F. Dufaux, “Adaptive non separable vector lifting scheme for digital holographic data compression,” *Applied Optics*, Vol. 54, Issue 1, pp. A98-A109 (2015)



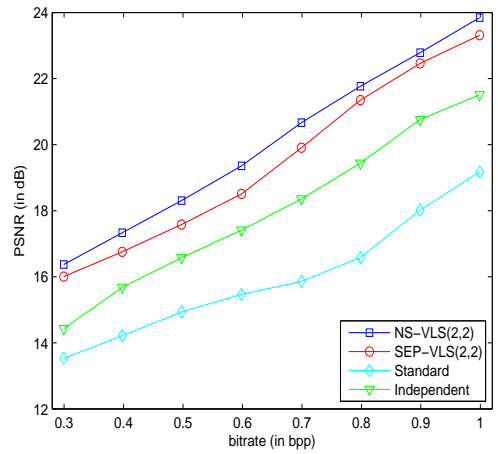
(a)



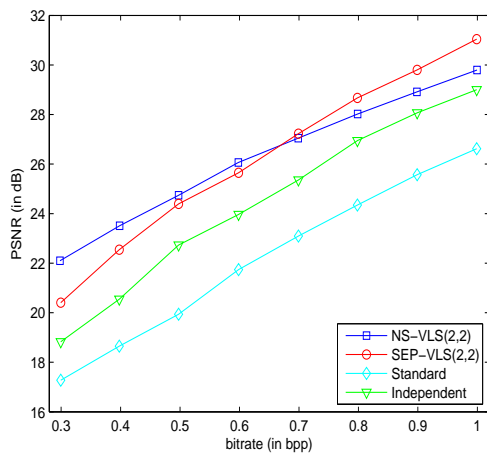
(b)



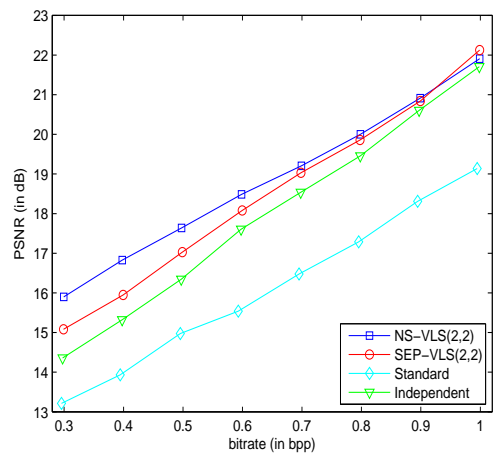
(c)



(d)

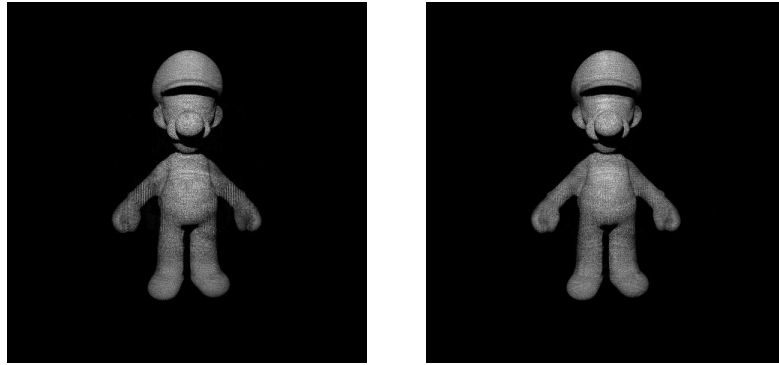


(e)



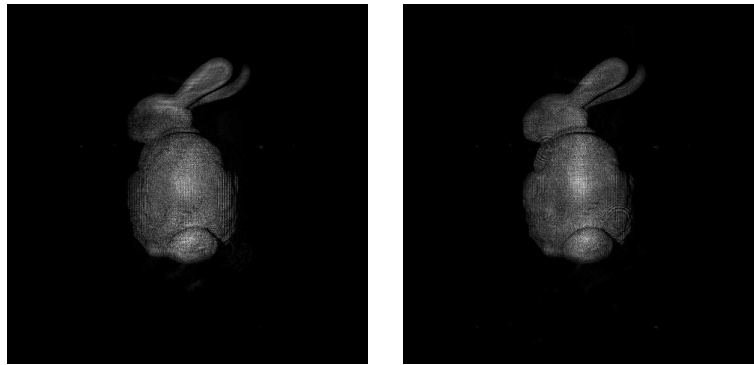
(f)

Figure 5.2: Rate-distortion performance of the different hologram compression schemes for the objects: (a) “Luigi-1”, (b) “Luigi-2”, (c) “Bunny-1”, (d) “Bunny-2”, (e) “Girl”, (f) “Teapot”.



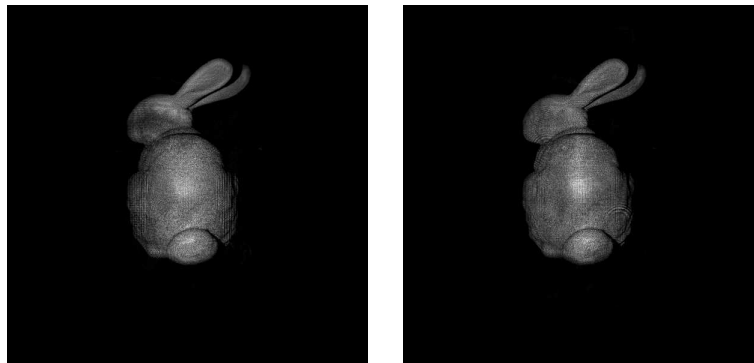
(a) PSNR=23.83 dB, SSIM=0.87 (b) PSNR=24.95 dB, SSIM=0.89

Figure 5.3: Reconstructed “Luigi-1” object at 0.9 bpp using: (a)SEP-VLS(2,2), (b) NS-VLS(2,2).



PSNR=22.03 dB, SSIM=0.82

PSNR=22.21 dB, SSIM=0.80



PSNR=24.32 dB, SSIM=0.87

PSNR=24.76 dB, SSIM=0.87

(a)

(b)

Figure 5.4: Reconstructed “Bunny-1” object at 0.5 bpp (upper) and 0.7 bpp (lower) using: (a)SEP-VLS, (b) NS-VLS.

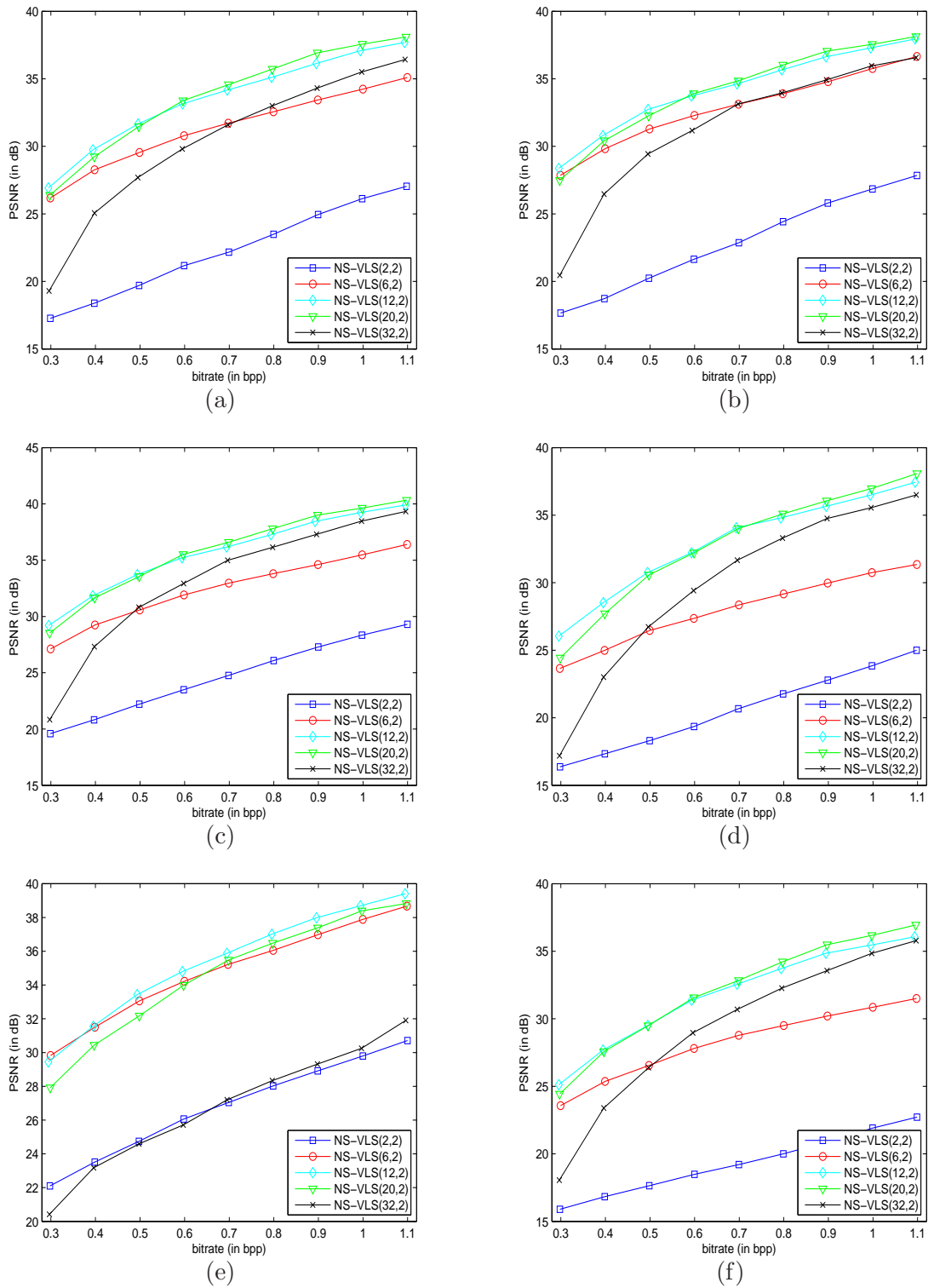
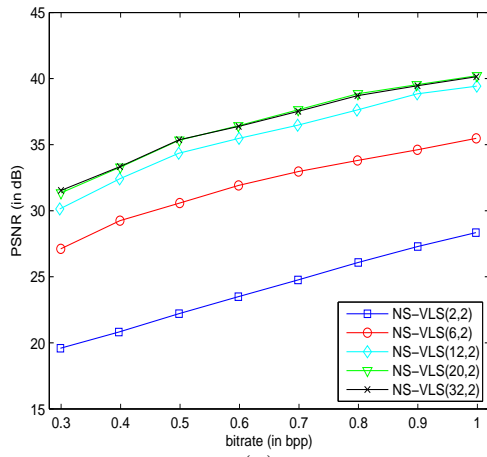
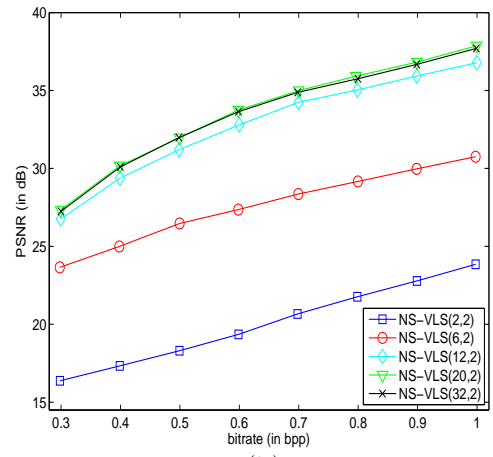


Figure 5.5: Rate-distortion performance of the proposed NS-VLS with different prediction filter lengths for the objects: (a) "Luigi-1", (b) "Luigi-2", (c) "Bunny-1", (d) "Bunny-2", (e) "Girl", (f) "Teapot".



(a)



(b)

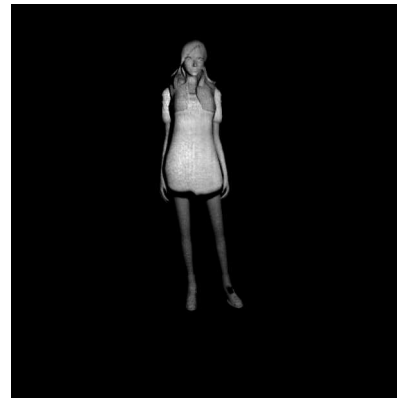
Figure 5.6: Rate-distortion performance of the proposed NS-VLS with different prediction filter lengths for the objects: (a) “Bunny-1”, (b) “Bunny-2”. An example where the overhead coding cost of the filter coefficients is not taken into account.



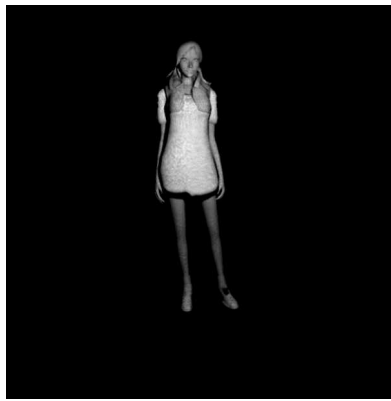
(a)Original



(b) PSNR=26.06 dB, SSIM=0.93



(c) PSNR=34.22 dB, SSIM=0.98



(d) 34.79 dB, SSIM=0.99



(e) PSNR=33.99 dB, SSIM=0.99



(f) PSNR=25.71 dB, SSIM=0.89

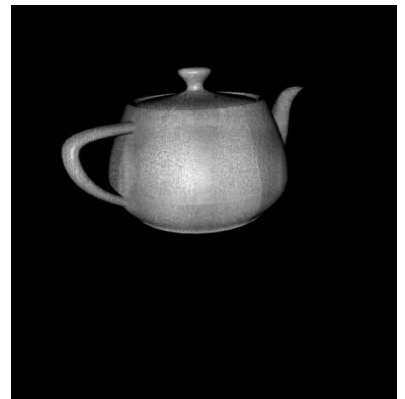
Figure 5.7: Reconstructed “Girl” objects at 0.6 bpp by using (b) NS-VLS(2,2), (c) NS-VLS(6,2), (d) NS-VLS(12,2), (e) NS-VLS(20,2), (f) NS-VLS(32,2).



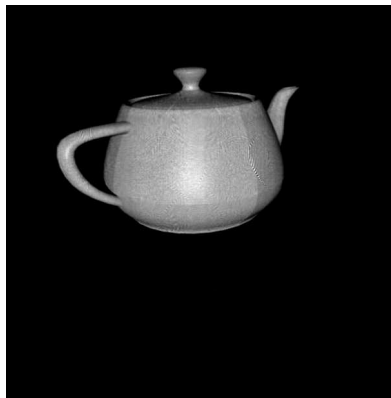
(a)Original



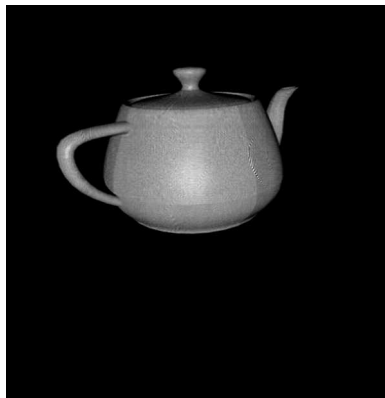
(b) PSNR=20.00 dB, SSIM=0.69



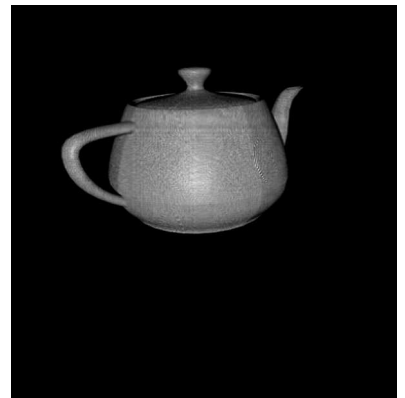
(c) PSNR=29.50 dB, SSIM=0.94



(d) 33.72 dB, SSIM=0.96



(e) PSNR=34.22 dB, SSIM=0.97



(f) PSNR=32.77 dB, SSIM=0.94

Figure 5.8: Reconstructed “Teapot” objects at 0.8 bpp by using: (b) NS-VLS(2,2), (c) NS-VLS(6,2), (d) NS-VLS(12,2), (e) NS-VLS(20,2), (f) NS-VLS(32,2).

Chapter 6

Investigation of Compressing Phase-shifting Holographic Data by Video Coding Schemes

6.1 Introduction

In this chapter, we propose to use two mainstream video coding schemes - advanced video coding (AVC) and high efficiency video coding (HEVC) - for the compression of phase-shifting holographic data. This preliminary investigation can be divided into two parts: the efficiency comparison between the compression performances of video coding schemes on phase-shifting digital hologram sequence (PSDHS) generated from 2D image sequences and video coding schemes on shifted distance information generated from single image.

For the first investigation, the holographic data is generated in the same way as described in the previous chapters, differently, the data should be re-formatted to satisfy the input requirements of the video coding software. The second investigation includes procedures of generating digital hologram sequences, the arrangement of hologram frames to form a video stream and its compression. Similarly, the digital hologram sequences used in this chapter are also CGH sequences based on the Fresnel transform from three 2D image sequences. The sequences are coded and reconstructed to evaluate the performance of the coding schemes by comparing their reconstructions with those from the uncompressed sequences.

This chapter is organized as follows: Section 6.2 presents the generation details of digital

hologram sequences by using the standard image sequences and the coding processing on the sequences by video coding schemes, followed with the experimental comparisons. Section 6.3 describes the scheme and its performance of applying AVC and HEVC on shifted distance data generated from different object images. Conclusions are given in Section 6.4.

6.2 Investigation of AVC and HEVC on hologram sequences generated from image sequences

6.2.1 Overview of compression schemes for digital holographic sequences

Some works on compressing hologram sequences have been reported. However, in the absence of a specific hologram sequence compression technique, most methods are based on 2D video compression techniques.

Seo *et al.* [69] used a multi-view prediction technique and a temporal motion prediction technique to remove the spatial and temporal data redundancies. The predicted and compensated data is then compressed by MPEG-2 encoder. Enhanced performance has been reported.

The use of MPEG-4 Advanced Simple Profile (ASP) for the compression of hologram sequences was investigated by Darakis [70]. Higher performance is obtained by MPEG-4 ASP inter-frame coding in the proposed approach, compared to independent intra-frame coding.

A 3D scanning method is introduced in [71]. More specifically, interference patterns are divided into blocks, and 2D DCT is performed. The resulting segments are then scanned in 3D, in order to form a sequence which is then compressed using a combination of advanced video coding, Differential Pulse Code Modulation and lossless coding. High compression rates are reported.

Even though there are not many work contributing directly on holographic sequence compression, it is still interesting to investigate the performance of more recent video coding schemes. Moreover, the compression efficiency on visual digital data of two mainstream video coding methods AVC and HEVC has been proved to be remarkable, especially HEVC which can reach twice the compression rate of AVC with similar quality. As a result, the inter mode coding of AVC and HEVC are applied on phase-shifting hologram sequences in this section.

6.2.2 Generation and processing of phase-shifting digital hologram sequence

The overall scheme is described as shown in Fig. A.7. The digital hologram sequences are generated from the sequences of “bitmap” images. The models are provided by a virtual camera which captures the motion of virtual 3D objects. Each 2D frame yields three digital holograms by the Fresnel transform as explained in Chapter 2.

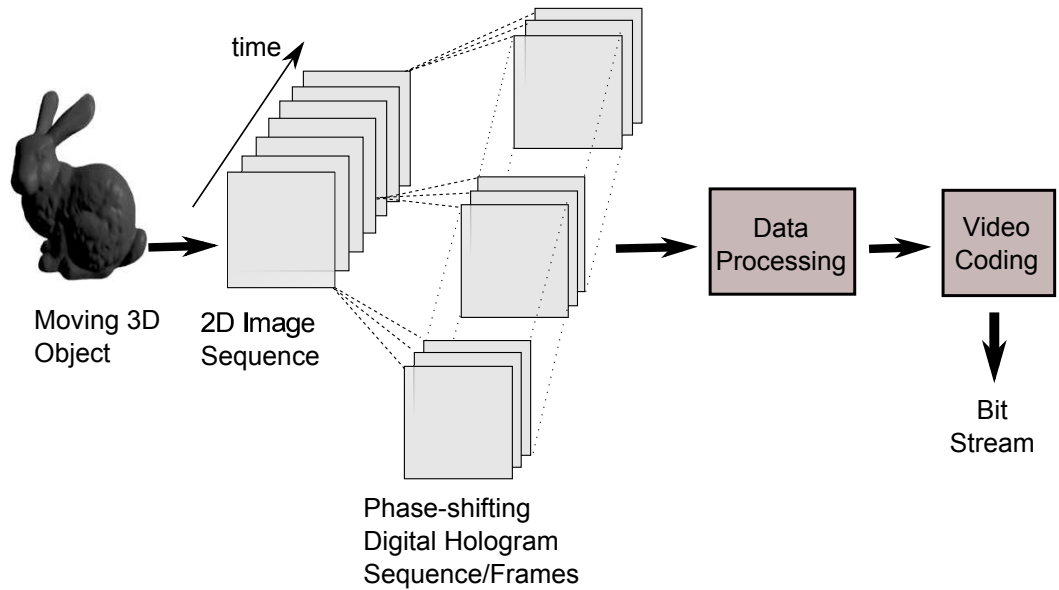


Figure 6.1: Over scheme for digital holographic video processing

Normally, YUV format is the main raw video format used in video coding softwares. So before encoding, the generated PSDHS should be converted to appropriate YUV format video to satisfy the input format of the coding softwares. Additionally, the applied HEVC version only accepts YUV 4:2:0 format as input. So YUV 4:2:0 format is selected as the input format for both AVC and HEVC. With a proposed construction that each holographic frame consists of one digital hologram as Y component and dummy U and V components (with 128 selected as value), the original PSDHS is converted to YUV 4:2:0 format video. After processing the digital hologram sequences into appropriate video format, coding procedure is conducted.

6.2.3 Experimental results

Coding setup

The CGH setups for generating holograms are the same as those in Chapter 4 and 5. Two 2D image sequences are provided for compression. For simplicity, the motion of one single object on its object plane is captured in each sequence. Each of the two sequences (named “BUNNY”, and “CONE”, respectively) includes a simple virtual 3D object rotating in the center of the object plane. The length of each image sequence is 10, so each phase-shifting digital holographic video has 30 frames in YUV 4:2:0 format with uncompressed bitrate of 129600kbps.

The performance of AVC and HEVC is studied using the reference softwares JM 18.4 and HM 9.2, respectively. For each codec, the size of frames in input and output video file is 600×600 . Some other basic encoder configurations for the JM and HM are depicted in Fig. 6.2(a) and (b), respectively.

Rate-distortion

The bitrate of the compressed bitstreams, the PSNR and SSIM measurement [54] of each image sequence reconstructed by AVC and HEVC are shown in Table. 6.1 and Table. 6.2, by changing the QP parameters.

Table 6.1: Bitrate (kbps), PSNR (dB) and MSSIM obtained by AVC

	BUNNY			CONE		
QP	Bitrate	PSNR	SSIM	Bitrate	PSNR	SSIM
26	11938.60	32.55	0.93	10604.58	30.28	0.86
28	9109.42	30.38	0.89	8178.02	28.31	0.82
30	6466.31	28.09	0.81	5886.76	26.10	0.76
32	4675.22	26.13	0.70	4297.73	24.12	0.70
34	3313.46	24.23	0.57	3111.75	22.27	0.63

Fig. 6.3 depicts the bitrate-PSNR and bitrate-SSIM curves of each sequence by AVC and HEVC. It can be observed that HEVC globally performs significantly better than AVC both in terms of PSNR and SSIM.

```

ProfileIDC          = 100 # Profile IDC (66=baseline, 77=main, 88=extended;
                        # FREXT Profiles: 100=High, 110=High 10, 122=High 4:2:2, 244=High 4:4:4)
IntraProfile        = 0 # Activate Intra Profile for FRExt (0: false, 1: true)
LevelIDC           = 40 # (e.g. ProfileIDC=110, IntraProfile=1 => High 10 Intra Profile:
                        # Level IDC (e.g. 20 = level 2.0)

IntraPeriod        = 0 # Period of I-pictures (0=only first)
IDRPeriod          = 0 # Period of IDR pictures (0=only first)
AdaptiveIntraPeriod = 1 # Adaptive intra period
AdaptiveIDRPeriod  = 0 # Adaptive IDR period
IntraDelay         = 0 # Intra (IDR) picture delay (i.e. coding structure of PPIPPP... )
EnableIDRGOP       = 0 # Support for IDR closed GOPs (0: disabled, 1: enabled)
EnableOpenGOP      = 0 # Support for open GOPs (0: disabled, 1: enabled)
FrameSkip          = 0 # Number of frames to be skipped in input (e.g 2 will code every 1
                        # Note that this now excludes intermediate (i.e. B) coded picture:
ChromaQPoffset     = 0 # Chroma QP offset (-51..51)

DisableSubpelME    = 0 # Disable Subpixel Motion Estimation (0=off/default, 1=on)
SearchRange        = 32 # Max search range

```

(a)

```

##### Unit definition #####
MaxCUwidth          : 64 # Maximum coding unit width in pixel
MaxCUheight         : 64 # Maximum coding unit height in pixel
MaxPartitionDepth   : 4 # Maximum coding unit depth
QuadtreeTULog2MaxSize : 5 # Log2 of maximum transform size for
                          # quadtree-based TU coding (2...6)
QuadtreeTULog2MinSize : 2 # Log2 of minimum transform size for
                          # quadtree-based TU coding (2...6)

QuadtreeTUMaxDepthInter : 3
QuadtreeTUMaxDepthIntra : 3

##### Coding Structure #####
IntraPeriod         : -1 # Period of I-Frame ( -1 = only first)
DecodingRefreshType : 0 # Random Access 0:none, 1:CDR, 2:IDR
GOPSize            : 8 # GOP Size (number of B slice = GOPSize-1)
# Type POC QPoffset QPfactor tcOffsetDiv2 betaOffsetDiv2 temporal_id #ref_pics_active
Frame1: P 8 1 0.442 0 0 0 4
Frame2: B 4 2 0.3536 0 0 0 2
Frame3: B 2 3 0.3536 0 0 0 2
Frame4: B 1 4 0.68 0 0 0 2
Frame5: B 3 4 0.68 0 0 0 2
Frame6: B 6 3 0.3536 0 0 0 2
Frame7: B 5 4 0.68 0 0 0 2
Frame8: B 7 4 0.68 0 0 0 2
ListCombination    : 1 # Use combined list for uni-prediction in B-slice

##### Motion Search #####
FastSearch          : 1 # 0:Full search 1:TZ search
SearchRange         : 32 # (0: Search range is a Full frame)
BipredSearchRange   : 4 # Search range for bi-prediction refinement
HadamardME          : 1 # Use of hadamard measure for fractional ME
FEN                 : 1 # Fast encoder decision

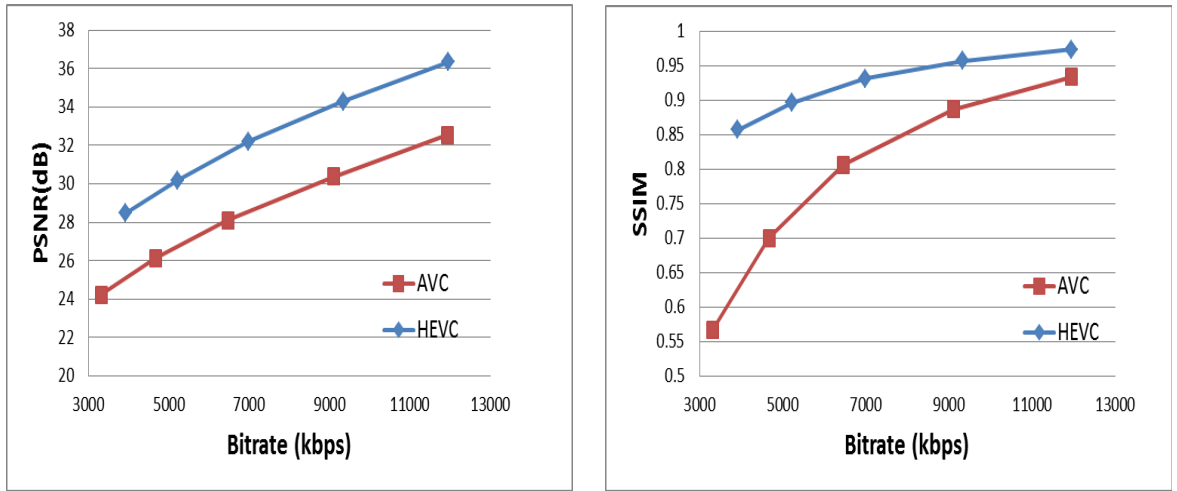
```

(b)

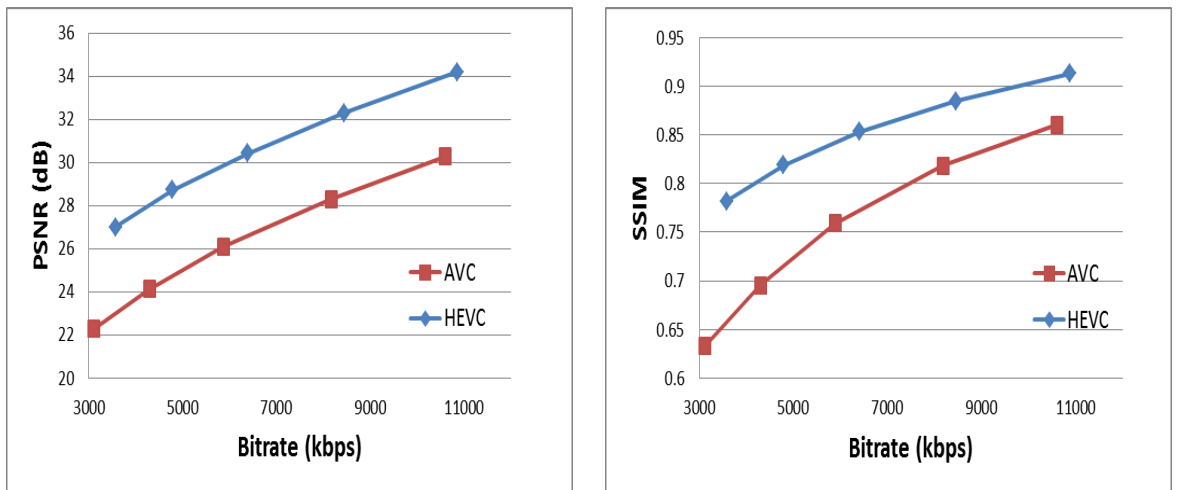
Figure 6.2: Some basic encoder configurations for (a)JM and (b) HM

Table 6.2: Bitrate (kbps), PSNR (dB) and MSSIM obtained by HEVC

QP	BUNNY			CONE		
	Bitrate	PSNR	SSIM	Bitrate	PSNR	SSIM
19	11949.54	36.35	0.97	10867.58	34.19	0.91
21	9337.94	34.30	0.96	8457.34	32.29	0.88
23	6989.67	32.19	0.93	6401.88	30.42	0.85
25	5221.62	30.17	0.90	4788.39	28.72	0.82
27	3920.66	28.47	0.86	3575.14	27.00	0.78



(a)



(b)

Figure 6.3: Rate-distortion performance of AVC and HEVC for the objects: (a) "Bunny", (b) "CONE"

Bjontegaard metric

In order to compare the two coding methods more precisely and intuitively, Bjontegaard metric [68] is also used to compute the average gain in PSNR, SSIM or the average bitrate

saving, as shown in Table. 6.3. HEVC achieves a gain of 3.82 and 0.12 in terms of PSNR and SSIM, respectively, when compared to AVC. Similarly, HEVC reaches a bitrate saving of up to 44.45% and 45.68%, when compared to AVC, for the PSNR and SSIM quality metrics.

Table 6.3: Bjontegaard Metrics for each sequence

	Bitrate(%)	PSNR	Bitrate(%)	SSIM
BUNNY	-40.71	3.56	-45.68	0.12
CONE	-44.45	3.82	-41.31	0.08

Visual quality

The reconstructed images by AVC and HEVC with different QP parameters can be observed in Fig. 6.4 and 6.5 for one frame of object “BUNNY” and “CONE”, respectively. At similar bitrates, the visual quality obtained by HEVC also confirms its superiority for compressing hologram sequences under inter mode.

6.3 Investigation of AVC and HEVC on shifted distance data obtained from still images

6.3.1 Motivation

For most of the video coding schemes, they support two kinds of basic compression methods- the intra compression and inter compression. Meanwhile, it has been proven that there are redundancies existing between the two sets of shifted distance holographic data. Consequently, the performance of applying video coding schemes on shifted distance information could be investigated in order to further exploit the characteristics of the data.

6.3.2 Experimental results

Comparative study

As being confirmed above, HEVC outperforms AVC for coding digital holographic data. So the application of AVC on shifted distance information is not studied in this investigation. Due to the time limitation, the influence of one parameter used in HEVC- the size of the

transform unit (TU)-is mainly investigated. The following modes of HEVC are considered on the data of “Luigi” object:

- HEVC intra mode with different sizes of TU ($TU = 3, 4, 5$), designated by HEVC-intra-3 (resp. HEVC intra 4, HEVC intra 5)
- Separable VLS based HEVC intra mode with the largest size of TU ($TU = 5$), designated by VLS-HEVC-intra-5
- HEVC inter mode with $TU = 5$, designated by HEVC-inter-5

Still, YUV format video is necessary as the input of HEVC. In order to further study the two sets of shifted distance information, YUV 4:2:0 format input which contains two frames is generated. For both the intra and inter HEVC schemes, each frame consists of one set of re-scaled shifted distance information as Y component and dummy U and V components (still with 128 selected as value). For the VLS-HEVC-intra-5 scheme, the raw shifted distance data is first processed by separable VLS decomposition. Then, the decomposed coefficients are re-scaled as Y component.

The configuration of HM software is kept the same for each scheme except for the parameters controlling the inter/intra mode selection and the transform size. Different reconstruction quality can be obtained under different QP setup.

Rate-distortion

Fig. 6.6 gives the performance comparison among different schemes by PSNR and SSIM measurement on reconstructed “Luigi” object. It can be observed that the performance can be improved a lot with the increasing size of TU under the intra mode. HEVC-intra-5 outperforms all the other intra modes with smaller TU. It can be explained is that when the size of TU is 5, it performs more effectively on the given patterns with less prediction vectors needed. However, the best TU size may vary according to different kinds of holographic patterns.

On the other hand, the VLS-HEVC-intra-5 scheme slightly outperforms the HEVC-intra-5 by both PSNR and SSIM measurement. Therefore, it can be concluded again that VLS based decomposition is efficient for our holographic data. However, the inter mode of HEVC yields the best performance, which means it can exploit the redundancies between the shifted distance information better.

6.4 Conclusion

The proposal of compressing PSDHS by AVC and HEVC has firstly been investigated in this chapter, which is evaluated by measuring the quality of the reconstructed object image sequence. The numerical experiments' results indicate that, compressing with the inter mode of both AVC and HEVC can offer good reconstruction images with good quality, however, HEVC globally outperforms AVC.

The research work reported in this chapter has led to this publication:

- Y. Xing, B. Pesquet-Popescu, and F. Dufaux, "Compression of computer generated phase-shifting hologram sequence using AVC and HEVC," in *Proc. SPIE, Applications of Digital Image Processing XXXVI*, 8856, San Diego, California, USA, 2013.

In the second investigation, the performance of the inter and intra mode of HEVC on shifted distance data has been studied. Still, the inter mode of HEVC outperforms than any other schemes. However, the separable VLS decomposition based HEVC scheme performs better than the other intra mode. Inspired on the results in Chapter 5, the NS-VLS decomposition based HEVC scheme should likely outperform the inter mode of HEVC. Furthermore, the performance of HEVC with different TU size implies that the suitable TU size for compressing holographic data should be further studied.

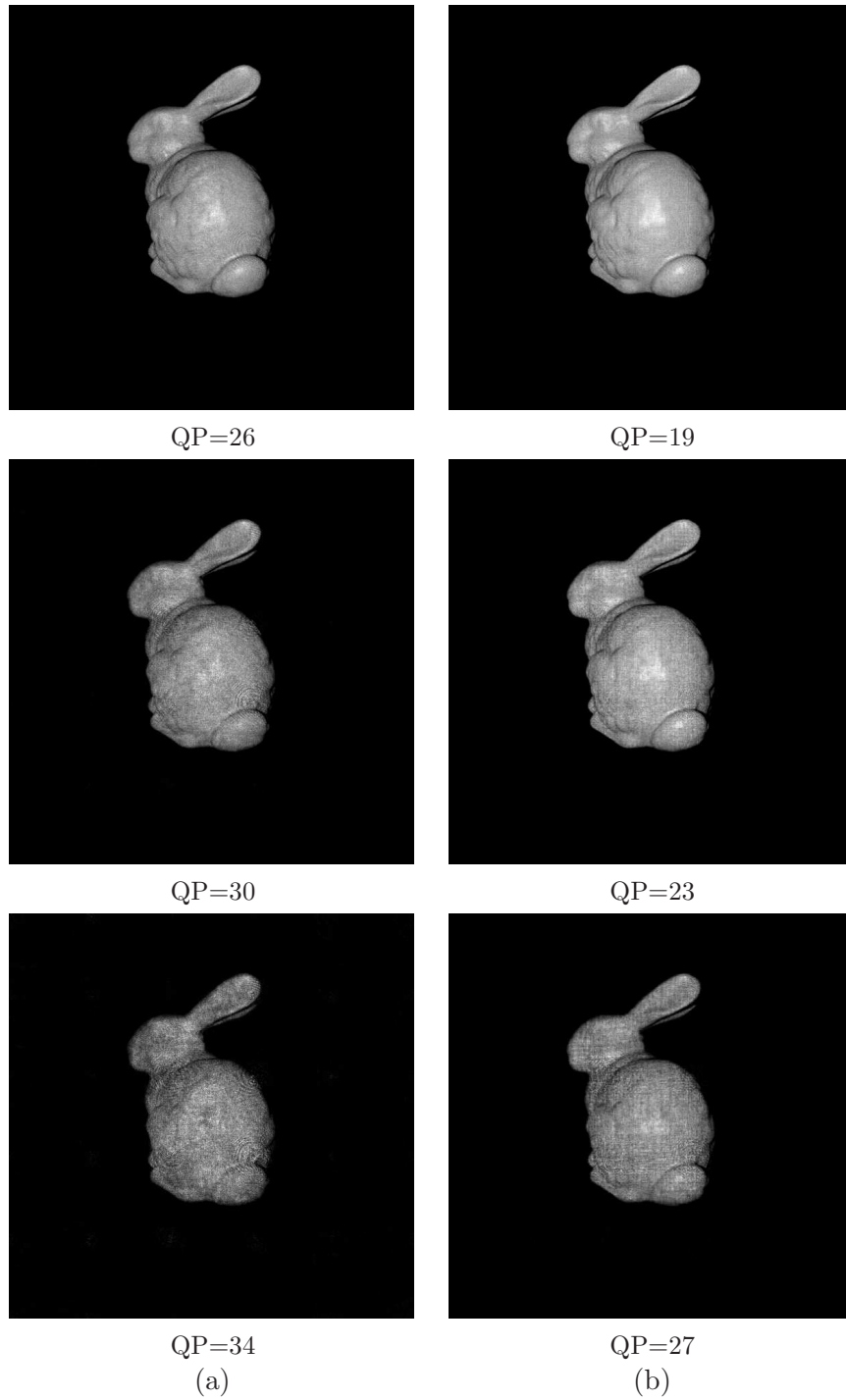


Figure 6.4: Reconstructed “Bunny” object by: (a)AVC and (b) HEVC with different QP parameters.

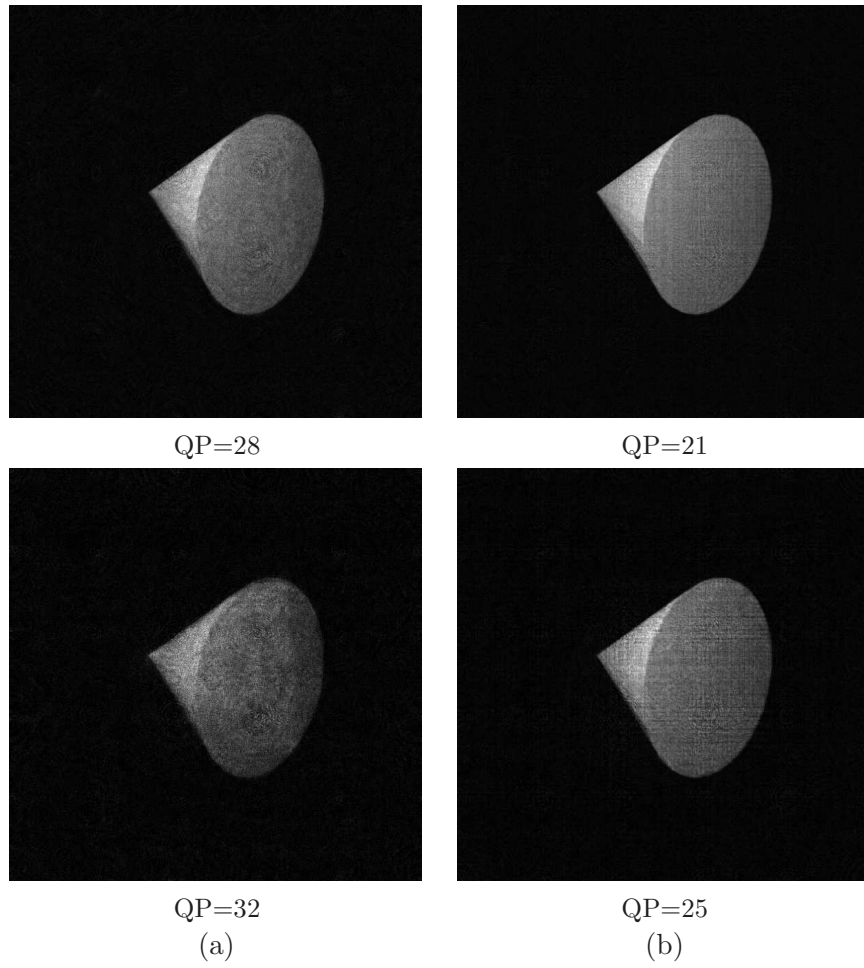
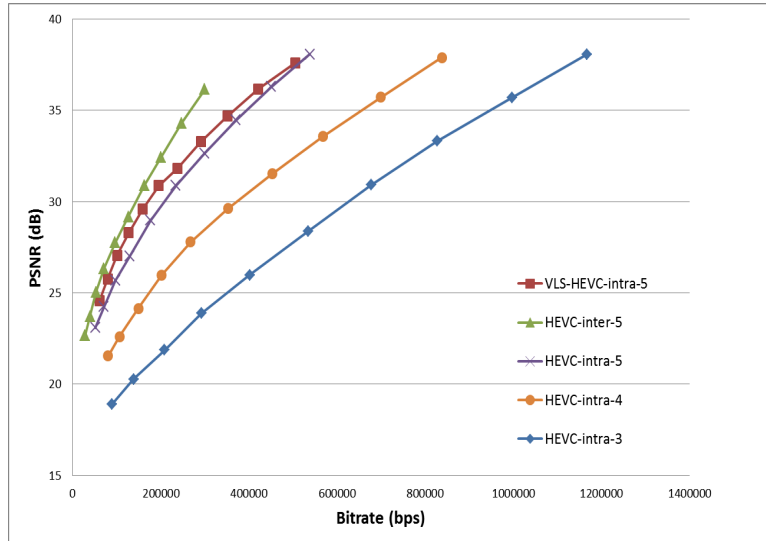
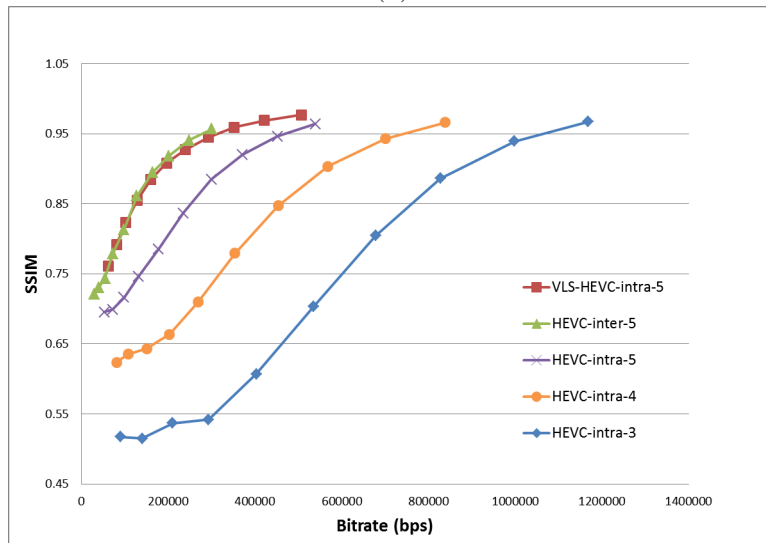


Figure 6.5: Reconstructed “CONE” object by: (a)AVC and (b) HEVC with different QP parameters.



(a)



(b)

Figure 6.6: (a) PSNR and (b) SSIM measurement obtained from compressing shifted distance information of “Luigi” object by different video coding schemes

Conclusions and Future Work

With the increasing interest for digital holography and computer generated holography in many applications, this thesis has been mainly devoted to design efficient compression schemes for phase-shifting digital holographic data with some basic analysis of different holographic data representation. In the following, the main concepts and contributions of this work are summarized with some possible future extensions.

The first contribution is that by analyzing the phase-shifting algorithm, a new representation of phase-shifting holographic data, named shifted distance information, is introduced. Further, a clear classification of different holographic data representations is given to make more understandable the data characteristics. Intensity and complex amplitude based representations respectively include representations obtained before and after applying phase-shifting algorithm. Moreover, the redundancies in different representations of phase-shifting holographic data are investigated in a comparative study, revealing that more redundancies exist in shifted distance information and real-imaginary information than amplitude-phase information.

The second contribution is that we propose a new joint multiscale decomposition of phase-shifting holographic data based on Vector Lifting Schemes (VLS). Unlike the other methods in the state-of-the-art where different information is separately encoded, two sets of shifted distance information (or real-imaginary information) are encoded jointly by VLS. The generated multiresolution representations of shifted distance information are more compact than those generated independently. In this context, we have proposed two decomposition schemes based on VLS, a separable one and a non separable one, respectively denoted as SEP-VLS and NS-VLS. In SEP-VLS, VLS has been performed in a separable way by cascading the 1D decomposition along the horizontal direction, then along the vertical direction. However, according to the visual patterns of the shifted difference data, some isotropic structures are clearly present. A non separable decomposition is consequently proposed to

improve the performance. Experimental results have demonstrated the superiority of the proposed SEP-VLS and NS-VLS over the conventional ones, while the NS-VLS is more adaptive to our data in terms of quality of the reconstructed 3D object.

Furthermore, due to the special structure of shifted distance data and the advantage of VLS which is exploiting the inter-images redundancies through the prediction stage, our third contribution is the investigation of NS-VLS with different filter lengths. The experimental results have shown significant gains by increasing the prediction filter length in terms of bitrate saving and visual quality of reconstruction.

At the end, in order to study the effectiveness of the mainstream video coding schemes, a preliminary investigation of compressing phase-shifting digital holographic data is provided by applying AVC and HEVC. The fourth contribution is divided into two parts. First, phase-shifting hologram sequences generated by 2D image sequences are compressed by inter mode of AVC and HEVC. The better performance of HEVC has been verified. Second, the effect of the TU size used in HEVC is investigated on shifted distance information generated by one image. It turns out that bigger TU size yields better performance. Moreover, applying HEVC after a separable VLS decomposition further improves performance, which demonstrate the efficiency of applying VLS on shifted distance data.

However, our work have some limitations which should be addressed in future work. Firstly, throughout the whole thesis, 2D image objects are selected for the simplicity to generate holograms. Secondly, unlike other 3D techniques, from the recording part to the display part, there are still technological bottlenecks to overcome in digital holography. Consequently, the research on compressing digital holographic data is also a quite new domain. Discussions of future work can be divided into four parts addressing some main concerns in our work.

1. First of all, the compression target should be improved. There are two main concerns: (1) the holograms of real world object may have different appearance than computer generated holograms (CGHs) because the real world recording system is more complicated, and (2) complex object models may also result in different interference patterns, for example, the number of objects and their locations. So our contributions should be further confirmed either on physically recorded holograms or CGHs with more complex object models. For the calculation models for CGHs, so far, we have tried ray tracing method using scatter point objects and Fresnel transform using 'bitmap'

images. In order to obtain more accurate holograms containing enough depth, texture, shade and angle information, other more complicated objects models, such as polygon mesh objects, could be tried with some accelerated algorithms.

2. Secondly, in order to compare with some methods mentioned in the state-of-the-art, such as the application of Fresnelets and Gabor wavelets, our proposed method based on VLS can also be extended to the reconstruction plane. Currently, our method is about camera (hologram) plane compression. Its advantage is that the coding is performed pixel by pixel and hence the introduced error is minimal contrary to transform-based methods which usually bring in block distortion. However, as in phase-shifting digital holography, there are more structure information in the reconstruction plane, it is expected to increase the effectiveness of the inter compression. Therefore, it should be promising to apply inter compression schemes on the complex wavefront in the reconstruction plane. It also would be interesting to extend the proposed approach to the digital holographic video coding framework.
3. Thirdly, it has been found that the filter length of the prediction operator in VLS and the TU size can significantly impact compression efficiency, methods to optimize filter length or TU size should be investigated to adapt to differently recorded holograms.
4. Finally, more appropriate metrics for the quality assessment could be investigated. Currently, NRMS and PSNR metrics applied on compressed holograms and original holograms are commonly used for physically recorded holograms. However, these two metrics do not always predict the visual quality of the reconstructed objects. In our work, we have found some limitations when applying SSIM. For example, sometimes at very low bitrate, the trend of the SSIM metric is contrary to the change of visual quality with the increasing bitrate. In conclusion, the problem of quality assessment in the context of hologram compression still remains an open issue.

Bibliography

- [1] D. Gabor. A new microscopic principle. *Nature*, 161(4098):777–778, 1948.
- [2] U. Schnars and W. Jüptner. Direct recording of holograms by a ccd target and numerical reconstruction. *Appl. Opt.*, 33(2):179–181, Jan 1994.
- [3] J. W. Goodman and R. W. Lawrence. Digital image formation from electronically detected holograms. *Applied Physics Letters*, 11(3):77–79, 1967.
- [4] W. J. Dallas. Computer-generated holograms. In B.Roy Frieden, editor, *The Computer in Optical Research*, volume 41 of *Topics in Applied Physics*, pages 291–366. Springer Berlin Heidelberg, 1980.
- [5] G. Tricoles. Computer generated holograms: an historical review. *Appl. Opt.*, 26(20):4351–4360, Oct 1987.
- [6] I. Yamaguchi and T. Zhang. Phase-shifting digital holography. *Optics Letters*, 22(16):1268–1270, Aug 1997.
- [7] A. Benazza-Benyahia, J.-C. Pesquet, and M. Hamdi. Vector lifting schemes for lossless coding and progressive archival of multispectral images. *IEEE Transactions on Geoscience and Remote Sensing*, 40(9):2011–2024, September 2002.
- [8] W. B. Pennebaker and J. L. Mitchell. *JPEG Still Image Data Compression Standard*. Kluwer Academic Publishers, Norwell, MA, USA, 1st edition, 1992.
- [9] M. Rabbani and R. Joshi. An overview of the jpeg 2000 still image compression standard. *Sig. Proc.: Image Communication*, 17(1):3–48, Jan 2002.

- [10] T. Wiegand, G.J. Sullivan, G. Bjontegaard, and A. Luthra. Overview of the h.264/AVC video coding standard. *Circuits and Systems for Video Technology, IEEE Transactions on*, 13(7):560–576, 2003.
- [11] G.J. Sullivan, J. Ohm, Woo-Jin Han, and T. Wiegand. Overview of the high efficiency video coding (hevc) standard. *Circuits and Systems for Video Technology, IEEE Transactions on*, 22(12):1649–1668, 2012.
- [12] M. Kaaniche, B. Pesquet-Popescu, and J.-C. Pesquet. 11-adapted non separable vector lifting schemes for stereo image coding. In *Signal Processing Conference (EUSIPCO), 2012 Proceedings of the 20th European*, pages 769–773, Aug 2012.
- [13] D. Gabor. Microscopy by reconstructed wave-fronts. *Proceedings of the Royal Society of London. Series A. Mathematical and Physical Sciences*, 197(1051):454–487, 1949.
- [14] Etienne Cuche, Frédéric Bevilacqua, and Christian Depeursinge. Digital holography for quantitative phase-contrast imaging. *Opt. Lett.*, 24(5):291–293, Mar 1999.
- [15] Frank Dubois, Luc Joannes, and Jean-Claude Legros. Improved three-dimensional imaging with a digital holography microscope with a source of partial spatial coherence. *Appl. Opt.*, 38(34):7085–7094, Dec 1999.
- [16] Maxime Jacquot, Patrick Sandoz, and Gilbert Tribillon. High resolution digital holography. *Optics Communications*, 190(1-6):87 – 94, 2001.
- [17] D. Abookasis and J. Rosen. Fourier, Fresnel and image CGHs of three-dimensional objects observed from many different projections. In *Proceedings of SPIE, Interferometry XII: Techniques and Analysis*, volume 5531, pages 273–284, August 2004.
- [18] A. D. Stein, Z. Wang, and J. S. Leigh. Computer-generated holograms: A simplified ray-tracing approach. In *Computers in Physics*, pages 389–392, 1992.
- [19] N. Masuda, T. Ito, T. Tanaka, A. Shiraki, and T. Sugie. Computer generated holography using a graphics processing unit. *Optics Express*, 14(2):603–608, Jan 2006.
- [20] I. Yamaguchi, J. Kato, S. Ohta, and J. Mizuno. Image formation in phase-shifting digital holography and applications to microscopy. *Applied Optics*, 40(34):6177–6186, Dec 2001.

- [21] Cheng-Shan Guo, Li Zhang, Hui-Tian Wang, Jun Liao, and Y. Y. Zhu. Phase-shifting error and its elimination in phase-shifting digital holography. *Opt. Lett.*, 27(19):1687–1689, Oct 2002.
- [22] J.W. Goodman. *Introduction to Fourier Optics*. McGraw-Hill, 2 edition, 1996.
- [23] Masahiro Yamaguchi. Ray-based and wavefront-based holographic displays for high-density light-field reproduction, 2011.
- [24] Jae-Hyeung Park, Min-Su Kim, Ganbat Baasantseren, and Nam Kim. Fresnel and fourier hologram generation using orthographic projection images. *Opt. Express*, 17(8):6320–6334, Apr 2009.
- [25] Natan T. Shaked and Joseph Rosen. Modified fresnel computer-generated hologram directly recorded by multiple-viewpoint projections. *Appl. Opt.*, 47(19):D21–D27, Jul 2008.
- [26] Hwi Kim, Joonku Hahn, and ByoungHo Lee. Mathematical modeling of triangle-mesh-modeled three-dimensional surface objects for digital holography. *Applied Optics*, 47(19):D117–D127, Jul 2008.
- [27] Kyoji Matsushima and Sumio Nakahara. Extremely high-definition full-parallax computer-generated hologram created by the polygon-based method. *Applied Optics*, 48(34):H54–H63, Dec 2009.
- [28] E. N. Leith and J. Upatnieks. Reconstructed wavefronts and communication theory. *Journal of the Optical Society of America*, 52(10):1123–1128, Oct 1962.
- [29] D. Taubman and M. Marcellin. *JPEG2000: Image Compression Fundamentals, Standards and Practice*. Kluwer Academic Publishers, Norwell, MA, USA, 2001.
- [30] D. Taubman. High performance scalable image compression with ebcot. *Image Processing, IEEE Transactions on*, 9(7):1158–1170, Jul 2000.
- [31] I. Daubechies. *Ten Lectures on Wavelets*. Society for Industrial and Applied Mathematics, 1992.
- [32] J. Max. Quantizing for minimum distortion. *Information Theory, IRE Transactions on*, 6(1):7–12, March 1960.

- [33] S. Lloyd. Least squares quantization in pcm. *IEEE Trans. Inf. Theor.*, 28(2):129–137, September 2006.
- [34] Y. Linde, A. Buzo, and R.M. Gray. An algorithm for vector quantizer design. *Communications, IEEE Transactions on*, 28(1):84–95, Jan 1980.
- [35] J.M. Shapiro. Embedded image coding using zerotrees of wavelet coefficients. *Signal Processing, IEEE Transactions on*, 41(12):3445–3462, Dec 1993.
- [36] A. Said and W.A. Pearlman. A new, fast, and efficient image codec based on set partitioning in hierarchical trees. *Circuits and Systems for Video Technology, IEEE Transactions on*, 6(3):243–250, Jun 1996.
- [37] T. J. Naughton, Y. Frauel, B. Javidi, and E. Tajahuerce. Compression of digital holograms for three-dimensional object reconstruction and recognition. *Applied Optics*, 41(20):4124–4132, 2002.
- [38] Emmanouil Darakis, Thomas J. Naughton, John J. Soraghan, and Bahram Javidi. Measurement of compression defects in phase-shifting digital holographic data. In *Proc. SPIE, Optical Information Systems IV*, volume 6311, 2006.
- [39] G. A. Mills and I. Yamaguchi. Effects of quantization in phase-shifting digital holography. *Applied Optics*, 44(7):1216–1225, Mar 2005.
- [40] Thomas J. Naughton, John B. McDonald, and Bahram Javidi. Efficient compression of fresnel fields for internet transmission of three-dimensional images. *Appl. Opt.*, 42(23):4758–4764, Aug 2003.
- [41] Alison E. Shortt, Thomas J. Naughton, and Bahram Javidi. A companding approach for nonuniform quantization of digital holograms of three-dimensional objects. *Opt. Express*, 14(12):5129–5134, Jun 2006.
- [42] A.E. Shortt, T.J. Naughton, and B. Javidi. Histogram approaches for lossy compression of digital holograms of three-dimensional objects. *Image Processing, IEEE Transactions on*, 16(6):1548–1556, June 2007.
- [43] A. Arrifano, M. Antonini, and M. Pereira. Multiple description coding of digital holograms using maximum-a-posteriori. In *European Workshop on Visual Information Processing*, pages 232–237, 2013.

- [44] Alison Shortt, Thomas J. Naughton, and Bahram Javidi. Compression of digital holograms of three-dimensional objects using wavelets. *Opt. Express*, 14(7):2625–2630, Apr 2006.
- [45] E. Darakis and J. J. Soraghan. Compression of interference patterns with application to phase-shifting digital holography. *Applied Optics*, 45(11):2437–2443, Apr 2006.
- [46] M. Liebling, T. Blu, and M. Unser. Fresnelets: new multiresolution wavelet bases for digital holography. *Image Processing, IEEE Transactions on*, 12(1):29–43, Jan 2003.
- [47] M. Unser. Splines: a perfect fit for signal and image processing. *Signal Processing Magazine, IEEE*, 16(6):22–38, Nov 1999.
- [48] E. Darakis and J.J. Soraghan. Use of fresnelets for phase-shifting digital hologram compression. *IEEE Transactions on Image Processing*, 15(12):3804–3811, 2006.
- [49] Kartik Viswanathan, Patrick Gioia, and Luce Morin. Wavelet compression of digital holograms: Towards a view-dependent framework, 2013.
- [50] Kartik Viswanathan, Patrick Gioia, and Luce Morin. Morlet wavelet transformed holograms for numerical adaptive view-based reconstruction, 2014.
- [51] David Blinder, Tim Bruylants, Erik Stijns, Heidi Ottevaere, and Peter Schelkens. Wavelet coding of off-axis holographic images, 2013.
- [52] Chuo-Ling Chang and B. Girod. Direction-adaptive discrete wavelet transform for image compression. *Image Processing, IEEE Transactions on*, 16(5):1289–1302, May 2007.
- [53] Tim Bruylants, David Blinder, Heidi Ottevaere, Adrian Munteanu, and Peter Schelkens. Microscopic off-axis holographic image compression with jpeg 2000, 2014.
- [54] Z. Wang, A.C. Bovik, H.R. Sheikh, and E.P. Simoncelli. Image quality assessment: from error visibility to structural similarity. *IEEE Transactions on Image Processing*, 13(4):600–612, 2004.
- [55] W. Sweldens. The lifting scheme: A custom-design construction of biorthogonal wavelets. *Applied and computational harmonic analysis*, 3(2):186–200, 1996.

- [56] F. J. Hampson and J.-C. Pesquet. M-band nonlinear subband decompositions with perfect reconstruction. *IEEE Transactions on Image Processing*, 7(11):1547–1560, 1998.
- [57] M. Kaaniche, A. Benazza-Benyahia, B. Pesquet-Popescu, and J.-C. Pesquet. Non separable lifting scheme with adaptive update step for still and stereo image coding. *Elsevier Signal Processing: Special issue on Advances in Multirate Filter Bank Structures and Multiscale Representations*, 91(12):2767–2782, January 2011.
- [58] M. Kaaniche, B. Pesquet-Popescu, A. Benazza-Benyahia, and J.-C. Pesquet. Adaptive lifting scheme with sparse criteria for image coding. *Journal on Advances in Signal Processing: Special issue on New Image and Video Representations Based on Sparsity*, 2012(1), January 2012.
- [59] A. Gouze, M. Antonini, M. Barlaud, and B. Macq. Design of signal-adapted multidimensional lifting scheme for lossy coding. *Image Processing, IEEE Transactions on*, 13(12):1589–1603, Dec 2004.
- [60] V. Chappelier and C. Guillemot. Oriented wavelet transform for image compression and denoising. *Image Processing, IEEE Transactions on*, 15(10):2892–2903, Oct 2006.
- [61] Stéphane Mallat. Geometrical grouplets. *Applied and Computational Harmonic Analysis*, 26(2):161 – 180, 2009.
- [62] Mounir Kaaniche, Amel Benazza-Benyahia, Béatrice Pesquet-Popescu, and J-C Pesquet. Vector lifting schemes for stereo image coding. *IEEE Trans. on Image Proc.*, 18(11):2463–2475, 2009.
- [63] M.S. Moellenhoff and M.W. Maier. Transform coding of stereo image residuals. *IEEE Transactions on Image Processing*, 7(6):804–812, June 1998.
- [64] N. V. Boulgouris and M. G. Strintzis. A family of wavelet-based stereo image coders. *IEEE Transactions on Circuits and Systems for Video Technology*, 12(10):898–903, 2002.
- [65] Ronald R. Coifman and M. Victor Wickerhauser. Entropy-based algorithms for best basis selection. *IEEE Transactions on Information Theory*, 38(2):713–718, 1992.

- [66] Z. Wang, A. C. Bovik, H. R. Sheikh, and E. P. Simoncelli. Image quality assessment: From error visibility to structural similarity. *IEEE Trans. on Image Processing*, 13(4):600–612, April 2004.
- [67] M. Kaaniche, A. Benazza-Benyahia, B. Pesquet-Popescu, and J.-C. Pesquet. Non-separable lifting scheme with adaptive update step for still and stereo image coding. *Signal Processing*, 91(12):2767 – 2782, 2011. Advances in Multirate Filter Bank Structures and Multiscale Representations.
- [68] G. Bjontegaard. Calculation of average psnr differences between rd-curves. *ITU-T SG16/Q.6 VCEG Doc., VCEG-M33*, 2001.
- [69] Young-Ho Seo, Hyun-Jun Choi, Jin-Woo Bae, Ji-Sang Yoo, and Dong wook Kim. Data compression technique for digital holograms using a temporally scalable coding method for 2-d images. In *Signal Processing and Information Technology, 2006 IEEE International Symposium on*, pages 326–331, Aug 2006.
- [70] Emmanouil Darakis and Thomas J. Naughton. Compression of digital hologram sequences using MPEG-4. In *Proc. SPIE, Holography: Advances and Modern Trends*, volume 7358, page 735811, 2009.
- [71] Young-Ho Seo, Hyun-Jun Choi, and Dong-Wook Kim. 3D scanning-based compression technique for digital hologram video. *Image Communication*, 22(2):144–156, February 2007.

Appendix A

Résumé en français

A.1 Introduction: Contexte de la thèse

Depuis son invention par Gabor en 1948 [1], la technique holographique est considéré comme l'ultime technologie tridimensionnel (3D). Des images 3D complètes d'objets enregistrées peuvent être reconstruites avec toutes ses informations de profondeurs en éclairant l'hologramme en utilisant l'onde de référence dans la procédure d'enregistrement. D'autre part, avec la promesse de plus en plus d'expérience en trois dimensions, l'intérêt pour la vidéo 3D ne cesse de prendre de l'ampleur. Les techniques de 3D actuelles sont largement basées sur les représentations stéréoscopiques et multi-vues limitées à l'utilisation de l'information de profondeur. De plus, elles introduisent irrémédiablement un conflit entre l'accommodation et la vergence, ce qui peut induire des maux de têtes, des nausées ou de la fatigue visuelle. En conséquence, la technique holographique peut être considérée comme étant la technologie 3D parfaite. En outre, en considérant les avantages obtenues par les capteurs CCD ainsi que le calcul par ordinateur, l'holographie numérique [2,3] et la génération d'hologrammes par ordinateur (CGHs) [4,5], ont également été mises au point avec des caractéristiques prometteuses.

Néanmoins, autant l'holographie traditionnelle que la holographie numérique, exige un système très stable pour enregistrer les hologrammes optiques de véritables objets 3D. Le faisceau laser éclairant les objets doit être hautement cohérent avec le faisceau laser de référence. Ces contraintes, ajoutées aux temps nécessaire à l'exposition d'un film ainsi que les contraintes de résolutions spatiales limitent l'application de l'holographie optique. Une solution alternative consiste à utiliser des hologrammes générés par ordinateur, ce

qui permet de simuler la procédure complète d'enregistrement et de reconstruction grâce à l'ordinateur. Peu importe la manière dont les hologrammes numériques sont obtenus, le fait que les données numériques holographiques représentent une énorme quantité d'information est un obstacle technologique important pour son utilisation pratique. Pour surmonter ce problème, l'utilisation de techniques de compression est nécessaire au stockage et à la transmission de données numériques holographiques.

Cependant, les méthodes de compression devraient être développées sur la base des objectifs recherchés. En d'autres termes, une représentation convenable des motifs d'interférence est requise pour une certaine méthode de compression. Directement, l'intensité des motifs d'interférence, qui est également définie comme un hologramme, devrait être la première option. Malheureusement, la qualité de la reconstruction d'un unique hologramme est mal influencée par l'image d'ordre zéro ou de l'image jumelle due à la perte de l'informations de phase, ce qui conduit au déphasage de phase en holographie numérique (PSDH) [6].

En PSDH, l'amplitude complexe de l'onde de l'objet sur le plan de l'hologramme peut être entièrement reconstruite en enregistrant au moins trois hologrammes numériques. En utilisant un algorithme de décalage de phase, d'autres représentations de la figure d'interférence, composées de deux ensembles de données, au lieu de trois ensembles de données d'informations sur l'intensité, peuvent être extraites. Dans ce cas, d'autres représentations sont plus appropriées pour la compression d'objets que trois ensembles de données d'intensité. D'autre part, comparé avec un seul hologramme en ligne et hors-axe, l'ensemble supplémentaire de données holographiques déphasées permet la compression des données holographiques numériques encore plus sévères. Ainsi, dans cette thèse, l'attention est plus particulièrement axée sur la représentation et la compression des données numériques holographiques basées sur le PSDH.

Comme mentionné précédemment, il y a deux objectifs principaux dans cette thèse. La première consiste à rechercher et à trouver une représentation appropriée de la figure d'interférence. Ensuite, sur la base de cette représentation, l'autre objectif est d'étudier et de développer des méthodes de compression efficaces.

Plus précisément, afin de se concentrer sur la compression, des hologrammes numériques, qui sont générés d'après un seul point de vue, sont simplement utilisés. Il pourrait être adapté à l'application de la compression d'hologrammes numériques parallaxes. Les différentes représentations des figures d'interférence sont obtenues, constituées d'au moins deux ensembles de données holographiques numériques. Par conséquent, l'utilisation du mode inter

frame pour la compression sur une telle représentation pourrait être plus efficace si une redondance importante existe dans cette représentation. Ainsi, l'analyse de redondance est tout d'abord effectuée afin de trouver une représentation appropriée. Avec cela, les méthodes de compression en inter frame principalement basées sur le schéma de lifting vectoriel (VLS) [7] sont adaptées et étudiées dans cette thèse.

A.2 Etat de l'art

Les deux types de compression sans et avec perte ont été testées pour la compression de données numériques holographiques. Dans un premier temps, les méthodes de codage et de quantification sans perte ont été étudiées et évaluées. Puis dans un stade plus avancé, nos travaux de recherche se sont orientés vers les méthodes de compression avec perte basée sur la transformée en ondelettes.

Shortt et al. [44] introduisent les ondelettes dans la compression de données réelles et imaginaires. Une transformée en ondelettes discrètes à une dimension est appliquée à chaque donnée et pour différents niveaux de résolution. Les coefficients en ondelettes sont ensuite quantifiés pour chaque niveau. Les tests ont montré qu'en moyenne les meilleures performances sont obtenues sur 3 niveaux. En outre, la compression des motifs d'interférence en déphasage de phase avec les standards de compression JPEG et JPEG 2000 a été traitée dans [45], en considérant des taux de compression allant de 20 à 27 et à des niveaux acceptables de reconstruction.

Cependant, les standards en ondelettes sont généralement conçus pour traiter des signaux par morceaux, tandis que les hologrammes ont une structure qui va au-delà des objets. Par conséquent, l'application directe des ondelettes à l'hologramme numérique n'est pas assez efficace. Dans ce contexte, Liebling et al. [46] ont développé une famille d'ondelettes (Fresnelet) obtenue en appliquant la transformée de Fresnel à une base de b-spline, adaptée aux spécificités de la donnée numérique holographique. Les propriétés multi-résolutions (translation, dilatation) des transformées de Fresnel sont d'abord étudiées pour construire de nouvelles ondelettes. Autrement, l'approche de convolution peut être utilisée dans la reconstruction de Fresnel. En outre, une relation d'incertitude de Heisenberg donnant la limite de l'étalement spatial dans le domaine de Fresnel est dérivée. Ce qui nous amène à la définition des Fresnelets. La base des Fresnelets est la transformée de Fresnel d'un b-spline.

Darakis et al. [48] introduisent les Fresnelets au niveau du déphasage de phase en holographie numérique pour la compression de données holographiques. Ils ont tout d'abord décomposé les données réelles et imaginaires en coefficients de Fresnel à une profondeur d'échelle requise. Les coefficients réels et imaginaires de Fresnel (Fresnelets) sont ensuite introduits à l'algorithme SPIHT. Les résultats expérimentaux prouvent la grande flexibilité de cette méthode dans la compression des données holographiques en déphasage de phase.

Cependant, Viswanathan et al. [49] ont démontrés que les Fresnelets présentent des limitations au niveau de la localisation fréquentielle relative à une reconstruction basée sur un point de vue. Ils proposent alors d'utiliser les ondelettes de Gabor pour mesurer localement les fréquences spatiales. Les coefficients pourront à ce moment-là être taillés correspondant à une sélection de points de vue différents. Différemment, la méthode de spectre angulaire est utilisé pour effectuer la reconstruction au lieu de la transformée de Fresnel. Les résultats expérimentaux prouvent que les ondelettes de Gabor sont capables de supprimer les ordres indésirables créés au moment de la reconstruction des hologrammes hors axe et d'avoir une meilleure localisation temps-fréquence pour les techniques de compression dépendant des vues. En outre, Ils ont proposé d'utiliser des ondelettes de Morlet pour transformer un hologramme et de reconstruire en partie une scène en utilisant un échantillon clairsemé de coefficients transformés de Morlet [50]. Il a été démontré que les représentations dépendantes des vues faites avec des ondelettes de Morlet forment un bon départ pour une meilleure compression des données holographiques pour la prochaine génération d'applications 3DTV.

D'autre part, Blinder et al. [51] ont également étudié les ondelettes pour le codage des hologrammes hors axe. Autrement, la propriété des hologrammes hors axe est d'abord examinée par analyse en composantes indépendantes, ce qui révèle l'importance de l'orientation et des hautes fréquences dans des hologrammes hors axe. Pour cette raison, les schémas de décomposition standards ne sont pas très appropriés pour la compression des hologrammes. Ils ont proposé certains régimes de décomposition alternative qui décomposent en outre les sous-bandes de haute fréquence. Les ondelettes de direction adaptative sont combinées pour améliorer les performances de compression du standard JPEG 2000. Une amélioration significative a été rapportée pour la compression avec perte par rapport aux standards qui utilisent des transformées par ondelettes discrètes basées sur la décomposition de Mallat. En outre, ils ont proposé un schéma de décomposition de paquets d'ondelettes combinée

avec des transformées en ondelettes directionnelles pour compresser les hologrammes microscopiques hors axe [53]. De plus, la norme JPEG 2000 a été modifiée pour pouvoir compresser des hologrammes en appliquant la nouvelle décomposition en ondelettes avec des transformées en ondelettes directionnelles. La version modifiée du standard JPEG 2000 montre une meilleure efficacité de compression.

Par-dessus de tout, les méthodes basées sur les ondelettes sont considérées comme des méthodes efficaces de compression des données holographiques. Cependant, tous les systèmes de codage décrits ci-dessus codent indépendamment les différentes données holographiques. Il pourrait, ainsi, être plus efficace de combiner les transformée en ondelettes et les méthodes de codage existants pour compresser les données holographiques en déphasage de phase. Cette thèse est axée sur l'élaboration d'un schéma de codage basé sur les ondelettes pour une représentation holographique spécifique.

A.3 Contributions

A.3.1 Analyse de base de données de représentation différente

Avant de concevoir un système de compression, plusieurs problèmes doivent être pris en considération. Afin d'obtenir des images d'objets reconstruits avec une bonne qualité, il faut utiliser l'interférométrie à décalage de phase (PSDH) pour les étapes d'acquisition. La géométrie de base de la PSDH est illustrée dans la Fig. A.1. L'une des deux rayons dont le faisceau laser est divisé éclaire l'objet et interfère avec l'autre rayon (le faisceau de référence) sur le dispositif CCD. Le faisceau de référence est réfléchi sur le miroir du transducteur piézo-électrique qui module en phase le faisceau. En décalant avec une phase constante le faisceau de référence, des différents hologrammes sont obtenus pour calculer l'amplitude complexe de l'onde qui représente l'objet.

Dans la plus simple application de PSDH, la phase ϕ de l'onde de référence est initialisé à zéro et change de $\frac{\pi}{2}$ à chaque itération. L'intensité des motifs d'interférence peut être exprimée comme

$$I_H(x, y; \phi) = |U_R(x, y; \phi) + U_O(x, y)|^2, \quad \phi \in \{0, \frac{\pi}{2}, \pi\} \quad (\text{A.1})$$

où (x, y) est la coordonnée du point sur le plan de l'hologramme. L'amplitude complexe du front d'onde de l'objet sur le plan de l'hologramme peut être calculée directement en

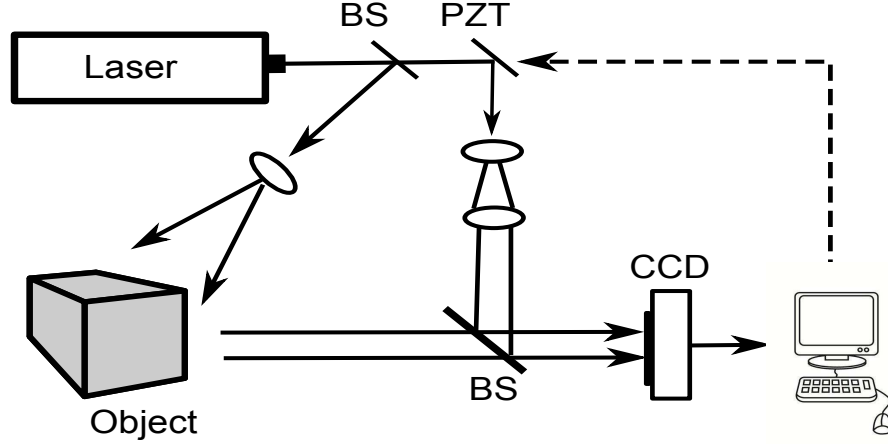


Figure A.1: Setup for phase-shifting digital holography: PZT, piezoelectric transducer mirror.

utilisant des hologrammes enregistrés, avec un algorithme à trois étapes:

$$\widehat{U}_O(x, y) = \frac{1 - \iota}{4U_R^*} \{I_H(x, y; 0) - I_H(x, y; \frac{\pi}{2}) + \iota[I_H(x, y; \frac{\pi}{2}) - I_H(x, y; \pi)]\} \quad (\text{A.2})$$

où U_R^* est le conjugué de l'onde de référence avec $\phi = 0$. Ensuite, l'amplitude complexe dans le plan image peut être reconstruite à travers la formule de la diffraction de Fresnel-Kirchhoff.

Cependant, avoir trois ensembles de données d'intensité à coder n'est pas avantageux en termes de performance de compression, c'est-à-dire, il serait préférable d'utiliser des ensembles de données plus compacts afin de réduire la complexité de computation à partir du début. D'autre part, les données devraient garder aussi toutes les informations utiles pour la reconstruction. Selon l'algorithme de décalage de phase, l'information la plus importante pour la reconstruction est le champ complexe de l'objet dans le plan de l'hologramme. Si ce champ peut être obtenu ou exprimé par une quantité plus faible d'information, cette information peut être considérée comme une représentation de motifs d'interférence. Jusqu'à présent, quelques représentations ont été utilisés principalement en conformité avec l'algorithme de décalage de phase ou les expressions des nombres complexes.

Information d'intensité

L'information d'intensité est la représentation directe, qui a été expliqué dans la section précédente. Comme mentionné plus en haut, compresser trois ensembles de

données n'est pas la solution optimale. Par conséquent, il réaliser la compression directement sur cette information n'est pas envisageable.

Information de distance décalée

À cette fin, nous introduisons les différences $D^{(1)}$ et $D^{(2)}$, définies comme:

$$\begin{cases} D^{(1)}(x, y) = I_H(x, y; 0) - I_H(x, y; \frac{\pi}{2}) \\ D^{(2)}(x, y) = I_H(x, y; \frac{\pi}{2}) - I_H(x, y; \pi), \end{cases} \quad (\text{A.3})$$

C'est suffisant de n'avoir que deux ensembles de données pour reconstruire le domaine complexe. Comme il consomme moins d'espace et est obtenu directement de la différence de l'information d'intensité, la définition de $D^{(1)}$ et $D^{(2)}$ est très efficace en tant que représentation de motifs d'interférence. Puisque cette représentation est définie comme la différence d'hogrammes déphasés, elle est aussi nommé " informations de distance décalé". La Fig. A.2 montre un exemple de la représentation $(D^{(1)}, D^{(2)})$.

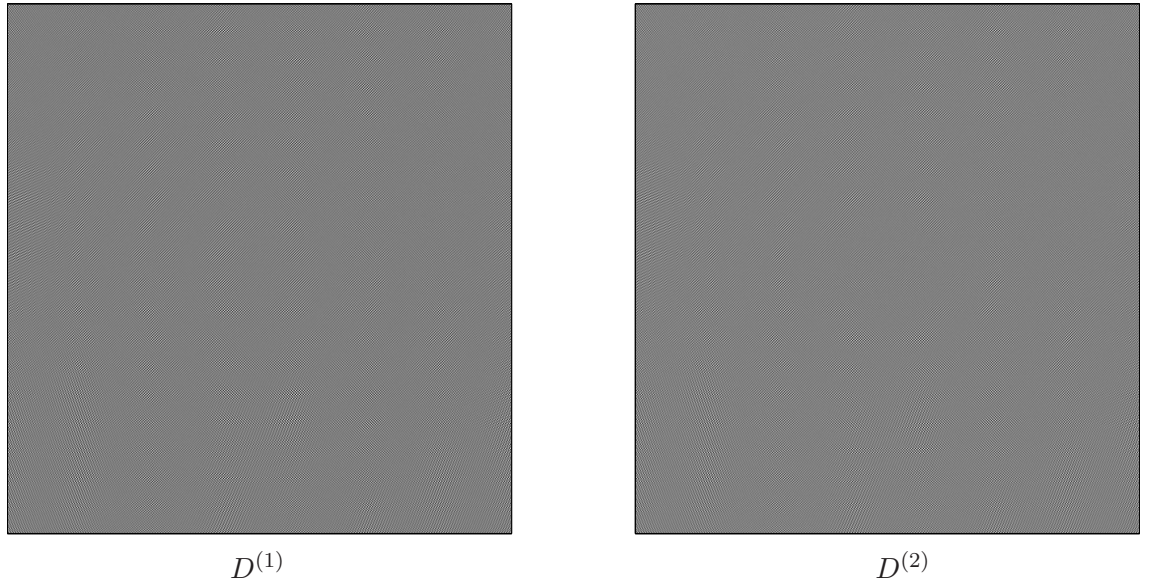


Figure A.2: Exemple de données de distance décalé $D^{(1)}$ and $D^{(2)}$.

Information réelles et imaginaires

Dans les coordonnées cartésiennes, un nombre complexe peut être exprimé sous la

forme $a + bi$, où a et b sont la partie réelle et la partie imaginaire, respectivement. Ainsi, le champ complexe obtenu par l'équation Eq. A.2 peut être exprimé comme suit:

$$\widehat{U}_O(x, y) = \text{real}(\widehat{U}_O(x, y)) + i \cdot \text{imag}(\widehat{U}_O(x, y)), \quad (\text{A.4})$$

où $\text{real}(\widehat{U}_O)$ et $\text{imag}(\widehat{U}_O)$ sont respectivement la distribution de la partie réelle et imaginaire du champ complexe de l'objet dans le plan de l'hologramme. Deux ensembles de données réelles et imaginaires sont aussi une représentation optimale. Fig. A.3 montre un exemple de cette représentation, où l'on voit des formes similaires à ceux montrés dans l'exemple de la figure Fig. A.2.

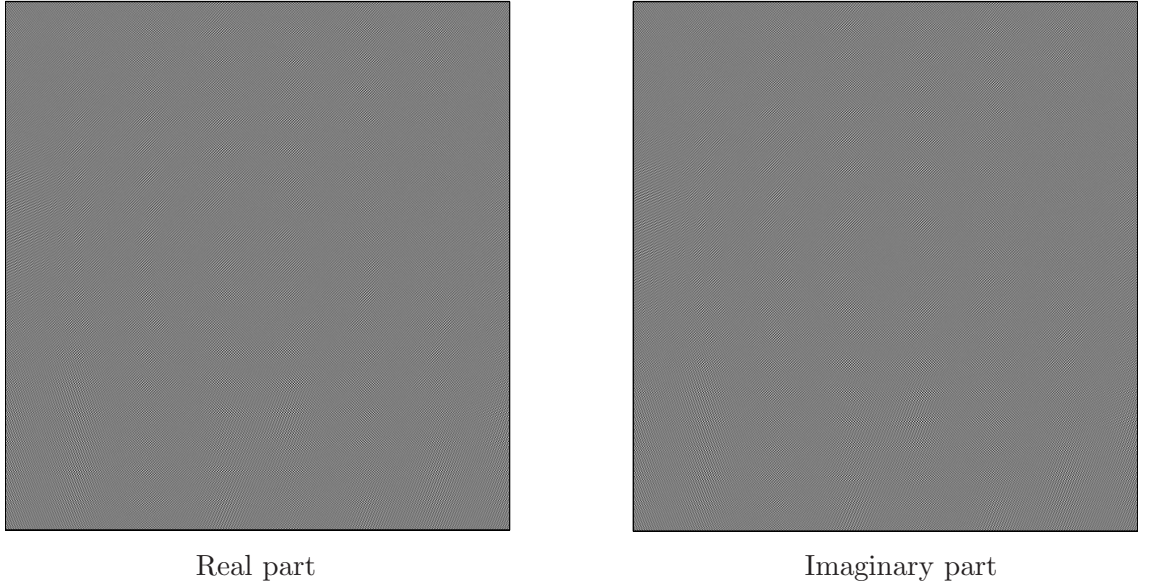


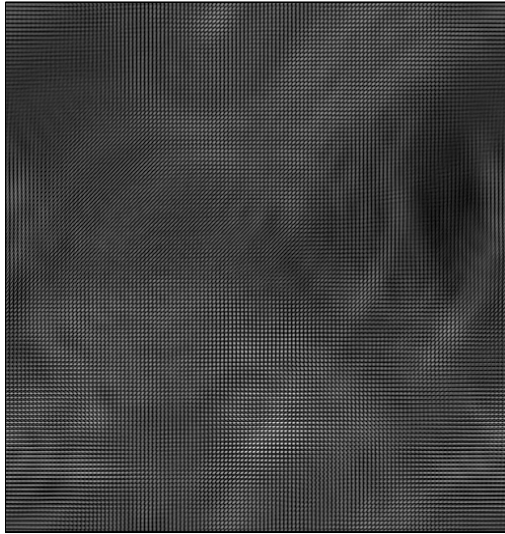
Figure A.3: Exemple de partie réelle et imaginaire distributions partielles.

Information d'amplitude et phase

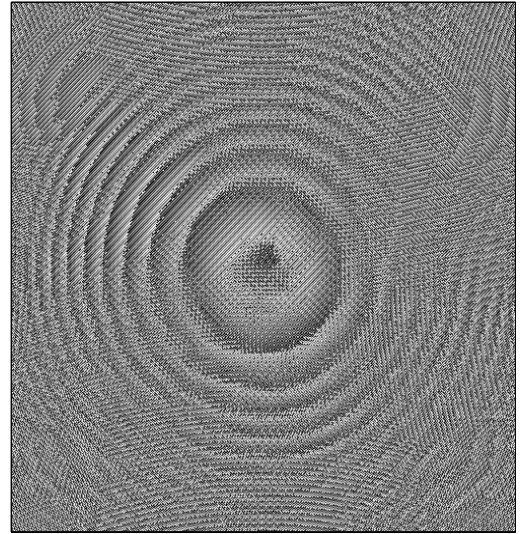
Une autre façon d'exprimer un nombre complexe est par le système de coordonnées polaires, où le champ complexe peut être écrit à travers la formule d'Euler

$$\widehat{U}_O(x, y) = \widehat{A}_O(x, y) \cdot e^{i\widehat{\psi}_O(x, y)}, \quad (\text{A.5})$$

L'information 3D de l'objet enregistré est entièrement contenue dans cette représentation, y compris les informations d'amplitude et de phase. Fig. A.4 montre un exemple.



Amplitude



Phase

Figure A.4: Exemple de distributions d'amplitude et phase.

Il est intéressant de noter que, sur la base des figures A.2, A.3 et A.4, il y a une forte corrélation entre les motifs obtenus avec différents décalages, ainsi qu'entre ceux la partie réelle et celle imaginaire. Toutefois, dans la représentation amplitude-phase, les motifs sont assez différents. On peut en déduire qu'il y a plus de redondance dans la représentation en distance décalée ou réelle-imaginaire, que dans la représentation amplitude-phase. Par conséquent, c'est plus efficace d'appliquer des méthodes de compression qui prennent en compte les dépendances entre représentations là où la redondance est plus élevé.

Sur la base des considérations ci-dessus, une analyse de base des différentes données holographiques est proposée. Les principaux outils d'analyse utilisés pour étudier les caractéristiques des différentes représentations sont des méthodes de quantification assez classiques. Comme l'on sait, la quantification scalaire traite individuellement les valeurs d'entrée, tandis que la quantification vectorielle les traite simultanément. Les différents moyens de traitement permettent l'analyse comparative des données d'entrée. En appliquant différentes méthodes de quantification sur les différentes représentations, on arrive à conclure que: 1) c'est mieux d'encoder séparément la représentation amplitude-phase; 2) en revanche, c'est plus avantageux d'effectuer un codage conjoint là où les méthodes de compression inter peut

apporter plus d'avantages sur les représentations avec une redondance plus élevée, tels que la représentation réelle-imaginaire et la représentation avec distances décalées.

A.3.2 Schéma de lifting vectoriel séparable

Le codage repose principalement sur la réduction de la redondance. Par exemple, cette redondance existe au niveau des similarités intra-image et inter-images dans le cas de différentes données comme la stéréo/multivue et la vidéo. Dans ce contexte, la méthode de codage conjoint, la plus répandue dans la littérature, consiste en deux étapes. En effet, pour coder deux images corrélées $S^{(1)}$ et $S^{(2)}$, la méthode sélectionne une image (par exemple $S^{(1)}$) comme une image de référence, qui sera ensuite codée indépendamment de l'autre. Ensuite, la seconde image $S^{(2)}$, considérée comme une image cible, est prédite à partir de la référence $S^{(1)}$, et la différence entre les deux images, appelée image résiduelle, est codée.

Contrairement à ce schéma standard, la principale caractéristique du schéma de lifting vectoriel est que il ne génère pas une image résiduelle, mais deux représentations multirésolutions compactes des images $S^{(1)}$ et $S^{(2)}$. Le schéma de base de cette structure est fourni par la Fig. A.5.

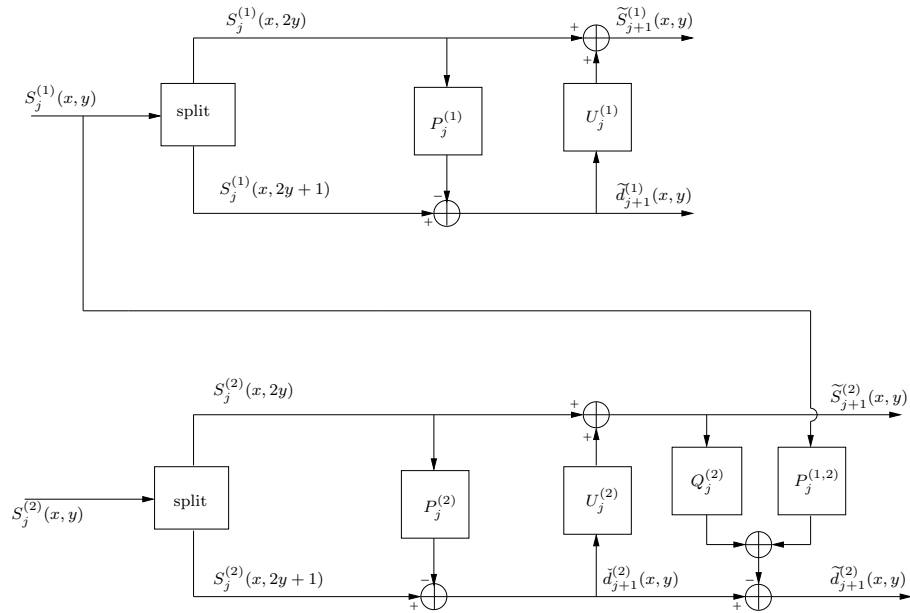


Figure A.5: Principe du schéma de lifting vectoriel séparable.

Par souci de simplicité, le principe de cette décomposition multi-échelle séparable est

décrits pour une ligne donnée x . Dans ce qui suit, $S_j^{(1)}$ et $S_j^{(2)}$ désignent les coefficients d'approximation des images $S^{(1)}$ et $S^{(2)}$ à chaque niveau de résolution j .

Décomposition de l'image de référence

Comme le montre la Fig. A.5, l'image de référence $S^{(1)}$ est d'abord codée en mode intra en utilisant une structure de lifting classique composée d'une étape de prédiction suivie par une étape de mise à jour. Ainsi, pour une ligne donnée x , le signal d'entrée $S_j^{(1)}(x, y)$ est tout d'abord divisé en deux sous-ensembles disjoints formés respectivement par les échantillons d'indices pairs $S_j^{(1)}(x, 2y)$ et impairs $S_j^{(1)}(x, 2y+1)$. Ensuite, chaque échantillon de l'un des deux sous-ensembles (par exemple des échantillons d'indices impairs) est prédite à partir des échantillons voisins d'indices pairs afin de générer le signal de détail $\tilde{d}_{j+1}^{(1)}$:

$$\tilde{d}_{j+1}^{(1)}(x, y) = S_j^{(1)}(x, 2y+1) - \sum_{k \in \mathcal{P}_j^{(1)}} p_{j,k}^{(1)} S_j^{(1)}(x, 2y-2k) \quad (\text{A.6})$$

où $p_{j,k}^{(1)}$ et $\mathcal{P}_j^{(1)}$ représentent respectivement les poids et le support du prédicteur des échantillons impairs $S_j^{(1)}(x, 2y+1)$. Enfin, les échantillons d'indices pairs sont lissés en utilisant les coefficients de détails calculés précédemment, ce qui permet de générer le signal approximation $\tilde{S}_{j+1}^{(1)}$:

$$\tilde{S}_{j+1}^{(1)}(x, y) = S_j^{(1)}(x, 2y) + \sum_{k \in \mathcal{U}_1^{(1)}} u_{j,k}^{(1)} \tilde{d}_{j+1}^{(1)}(x, y-k), \quad (\text{A.7})$$

où $\mathcal{U}_1^{(1)}$ désigne le support spatial de l'opérateur de mise à jour dont les coefficients sont notés par $u_{j,k}^{(1)}$.

Décomposition de l'image cible

Il est important de noter que la principale différence entre un schéma de lifting de base et le schéma de lifting vectoriel utilise une étape de prédiction hybride qui exploite à chaque étage les redondances intra et inter images.

Comme le montre la Fig. A.5, une structure P-U-P est utilisée pour coder l'image cible $S^{(2)}$. Plus précisément, une première étape de prédiction intra est appliquée pour générer un signal de détail intermédiaire $\tilde{d}_{j+1}^{(2)}$, qui sert à calculer le signal d'approximation $\tilde{S}_{j+1}^{(2)}$ à travers l'étape de mise à jour. Par la suite, une prédiction

hybride est effectuée en utilisant les échantillons de $S^{(1)}$ et $S^{(2)}$ afin de calculer le signal de détail final $\tilde{d}_{j+1}^{(2)}$. Ainsi, la décomposition résultante est exprimé par les équations suivantes:

$$\check{d}_{j+1}^{(2)}(x, y) = S_j^{(2)}(x, 2y + 1) - \sum_{k \in \mathcal{P}_j^{(2)}} p_{j,k}^{(2)} S_j^{(2)}(x, 2y - 2k), \quad (\text{A.8})$$

$$\tilde{S}_{j+1}^{(2)}(x, y) = S_j^{(2)}(x, 2y) + \sum_{k \in \mathcal{U}_j^{(2)}} u_{j,k}^{(2)} \check{d}_{j+1}^{(2)}(x, y - k), \quad (\text{A.9})$$

$$\tilde{d}_{j+1}^{(2)}(x, y) = \check{d}_{j+1}^{(2)}(x, y) - \left(\sum_{k \in \mathcal{Q}_j} q_{j,k} \tilde{S}_{j+1}^{(2)}(x, y - k) + \sum_{k \in \mathcal{P}_j^{(1,2)}} p_{j,k}^{(1,2)} S_j^{(1)}(x, 2y + 1 - k) \right) \quad (\text{A.10})$$

où $\mathcal{P}_j^{(2)}$ (resp. $\mathcal{P}_j^{(1,2)}$) est le support spatial du prédicteur utilisé en mode intra (resp. hybride), tandis que ses poids sont désignés par $p_{j,k}^{(2)}$ (resp. $p_{j,k}^{(1,2)}$), et \mathcal{Q}_j (resp. $q_{j,k}$) est le support (resp. poids) du second prédicteur intra.

Comme une décomposition séparable a été considérée, ces étapes sont appliquées sur les colonnes y des sous-bandes résultantes $\tilde{S}_{j+1}^{(1)}$, $\check{d}_{j+1}^{(1)}$, $\tilde{S}_{j+1}^{(2)}$ et $\check{d}_{j+1}^{(2)}$ afin de produire les sous-bandes d'approximation $S_{j+1}^{(1)}$ et $S_{j+1}^{(2)}$ ainsi que trois sous-bandes de détails, pour chaque signal, orientées horizontalement, verticalement et diagonalement. Cette décomposition est de nouveau itérée sur les sous-bandes d'approximation, ce qui produit les représentations multi-résolutions des deux images d'entrées.

Enfin, au dernier niveau de résolution J , au lieu de coder la sous-bande approximation de l'image cible $S_J^{(2)}$, il est proposé de coder la sous-bande résiduelle donnée par:

$$e_J^{(2)}(x, y) = S_J^{(2)}(x, y) - \sum_{k \in \mathcal{P}_J^{(1,2)}} p_{J,k}^{(1,2)} S_J^{(1)}(x, y - k). \quad (\text{A.11})$$

Les résultats expérimentaux ont indiqué la bonne performance de l'approche proposée par rapport aux méthodes conventionnelles en terme de la qualité de reconstruction de l'objet 3D. Un gain important d'environ 2 dB et 0.15 en terme de PSNR et SSIM respectivement, a été réalisé par rapport au codage indépendant de chaque image.

A.3.3 Schéma de lifting vectoriel non séparable

Comme il a été indiqué précédemment, la structure du lifting vectoriel qui a été développé est séparable. Cependant, un tel traitement, suivant les lignes puis les colonnes (ou inversement), rend la décomposition peu efficace dans le cas des images contenant des contours qui ne sont ni horizontaux ni verticaux. En particulier, il a été observé que les hologrammes présentent des structures similaires aux ondes. Pour cette raison, nous avons proposé d'utiliser un schéma de lifting vectoriel non séparable pour coder ces hologrammes. La structure d'analyse de ce schéma est illustré dans Fig. A.6.

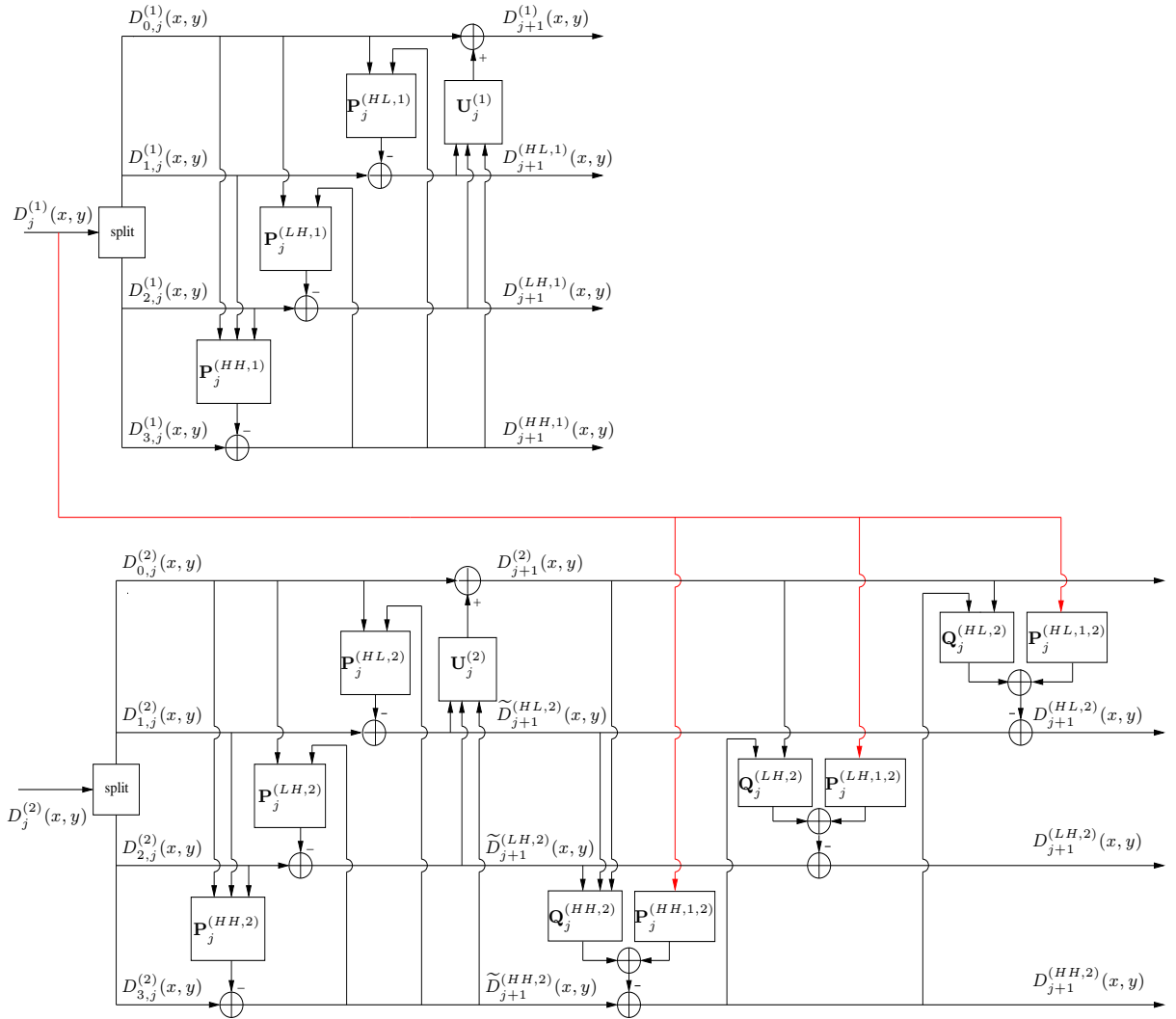


Figure A.6: Principe de la structure d'analyse du schéma de lifting vectoriel non séparable.

Comme le montre la Fig. A.6, l'image $D^{(1)}$, sélectionnée comme une image de référence, est codée on mode intra indépendamment de l'autre image. Pour cela, une structure de lifting non séparable [67], composée de trois étapes de prédiction et une étape de mise à jour, est appliquée à $D_j^{(1)}$ afin de générer les sous bandes de détails orientées diagonalement $D_{j+1}^{(HH,1)}$, verticalement $D_{j+1}^{(LH,1)}$ et horizontalement $D_{j+1}^{(HL,1)}$, et la sous bande approximation $D_{j+1}^{(1)}$. Ainsi, les coefficients d'ondelettes peuvent être exprimés, au niveau de résolution $(j + 1)$, comme suit:

$$D_{j+1}^{(HH,1)}(x, y) = D_{3,j}^{(1)}(x, y) - \left((\mathbf{P}_{0,j}^{(HH,1)})^\top \mathbf{D}_{0,j}^{(HH,1)} + (\mathbf{P}_{1,j}^{(HH,1)})^\top \mathbf{D}_{1,j}^{(HH,1)} + (\mathbf{P}_{2,j}^{(HH,1)})^\top \mathbf{D}_{2,j}^{(HH,1)} \right), \quad (\text{A.12})$$

$$D_{j+1}^{(LH,1)}(x, y) = D_{2,j}^{(1)}(x, y) - \left((\mathbf{P}_{0,j}^{(LH,1)})^\top \mathbf{D}_{0,j}^{(LH,1)} + (\mathbf{P}_{1,j}^{(LH,1)})^\top \underline{\mathbf{D}}_{j+1}^{(HH,1)} \right), \quad (\text{A.13})$$

$$D_{j+1}^{(HL,1)}(x, y) = D_{1,j}^{(1)}(x, y) - \left((\mathbf{P}_{0,j}^{(HL,1)})^\top \mathbf{D}_{0,j}^{(HL,1)} + (\mathbf{P}_{1,j}^{(HL,1)})^\top \overline{\mathbf{D}}_{j+1}^{(HH,1)} \right), \quad (\text{A.14})$$

$$D_{j+1}^{(1)}(x, y) = D_{0,j}^{(1)}(x, y) + \left((\mathbf{U}_{0,j}^{(HL,1)})^\top \mathbf{D}_{j+1}^{(HL,1)} + (\mathbf{U}_{1,j}^{(LH,1)})^\top \mathbf{D}_{j+1}^{(LH,1)} + (\mathbf{U}_{2,j}^{(HH,1)})^\top \mathbf{D}_{j+1}^{(HH,1)} \right), \quad (\text{A.15})$$

où pour chaque $i \in \{0, 1, 2\}$ et $o \in \{HL, LH, HH\}$,

- $\mathbf{P}_{i,j}^{(o,1)} = (p_{i,j}^{(o,1)}(s, t))_{(s,t) \in \mathcal{P}_{i,j}^{(o,1)}}$ représente le vecteur de prédiction dont le support est désigné par $\mathcal{P}_{i,j}^{(o,1)}$.
- $\mathbf{D}_{i,j}^{(o,1)} = (D_{i,j}^{(1)}(x + s, y + t))_{(s,t) \in \mathcal{P}_{i,j}^{(o,1)}}$ est un vecteur de référence utilisé pour calculer $D_{j+1}^{(o,1)}(x, y)$.
- $\underline{\mathbf{D}}_{j+1}^{(HH,1)} = (D_{j+1}^{(HH,1)}(x + s, y + t))_{(s,t) \in \mathcal{P}_{1,j}^{(LH,1)}}$ et $\overline{\mathbf{D}}_{j+1}^{(HH,1)} = (D_{j+1}^{(HH,1)}(x + s, y + t))_{(s,t) \in \mathcal{P}_{1,j}^{(HL,1)}}$ correspondent aux vecteurs de référence utilisés respectivement dans la deuxième et troisième étape de prédiction.
- $\mathbf{U}_{i,j}^{(o,1)} = (u_{i,j}^{(o,1)}(s, t))_{(s,t) \in \mathcal{U}_{i,j}^{(o,1)}}$ est les coefficients du vecteur de mise à jour dont le support est désigné par $\mathcal{U}_{i,j}^{(o,1)}$.
- $\mathbf{D}_{j+1}^{(o,1)} = (D_{j+1}^{(o,1)}(x + s, y + t))_{(s,t) \in \mathcal{U}_{i,j}^{(o,1)}}$ est un vecteur de référence contenant l'ensemble

des échantillons de détails utilisés dans l'étape de mise à jour.

Pour la deuxième image $D_j^{(2)}$, une structure de lifting similaire à celle utilisée avec $D_j^{(1)}$ est d'abord appliquée sur $D_j^{(2)}$ afin de produire trois sous-bandes de détails intermédiaires $\tilde{D}_{j+1}^{(HH,2)}$, $\tilde{D}_{j+1}^{(LH,2)}$ et $\tilde{D}_{j+1}^{(HL,2)}$, qui seront utilisées pour calculer les coefficients d'approximation $D_{j+1}^{(2)}$. Ensuite, un seconde étage de prédiction est ajoutée. Plus précisément, trois étapes de prédiction hybrides, qui visent à exploiter simultanément les redondances intra et inter images, sont appliquées afin de générer les sous-bandes de détails finaux $D_{j+1}^{(HH,2)}$, $D_{j+1}^{(LH,2)}$ and $D_{j+1}^{(HL,2)}$. Ces signaux sont exprimés comme suit:

$$\begin{aligned}
D_{j+1}^{(HH,2)}(x, y) &= \tilde{D}_{j+1}^{(HH,2)}(x, y) - \left((\mathbf{Q}_{0,j}^{(HH,2)})^\top \tilde{\mathbf{D}}_{0,j+1}^{(HH,2)} \right. \\
&\quad + (\mathbf{Q}_{1,j}^{(HH,2)})^\top \tilde{\mathbf{D}}_{1,j+1}^{(HH,2)} + (\mathbf{Q}_{2,j}^{(HH,2)})^\top \tilde{\mathbf{D}}_{2,j+1}^{(HH,2)} \\
&\quad + (\mathbf{P}_{0,j}^{(HH,1,2)})^\top \mathbf{D}_{0,j}^{(HH,1)} + (\mathbf{P}_{1,j}^{(HH,1,2)})^\top \mathbf{D}_{1,j}^{(HH,1)} \\
&\quad \left. + (\mathbf{P}_{2,j}^{(HH,1,2)})^\top \mathbf{D}_{2,j}^{(HH,1)} + (\mathbf{P}_{3,j}^{(HH,1,2)})^\top \mathbf{D}_{3,j}^{(HH,1)} \right), \tag{A.16}
\end{aligned}$$

$$\begin{aligned}
D_{j+1}^{(LH,2)}(x, y) &= \tilde{D}_{j+1}^{(LH,2)}(x, y) - \left((\mathbf{Q}_{0,j}^{(LH,2)})^\top \tilde{\mathbf{D}}_{0,j+1}^{(LH,2)} \right. \\
&\quad + (\mathbf{Q}_{1,j}^{(LH,2)})^\top \tilde{\mathbf{D}}_{1,j+1}^{(LH,2)} + (\mathbf{P}_{0,j}^{(LH,1,2)})^\top \mathbf{D}_{0,j}^{(LH,1)} \\
&\quad \left. + (\mathbf{P}_{2,j}^{(LH,1,2)})^\top \mathbf{D}_{2,j}^{(LH,1)} \right), \tag{A.17}
\end{aligned}$$

$$\begin{aligned}
D_{j+1}^{(HL,2)}(x, y) &= \tilde{D}_{j+1}^{(HL,2)}(x, y) - \left((\mathbf{Q}_{0,j}^{(HL,2)})^\top \tilde{\mathbf{D}}_{0,j+1}^{(HL,2)} \right. \\
&\quad + (\mathbf{Q}_{1,j}^{(HL,2)})^\top \tilde{\mathbf{D}}_{1,j+1}^{(HL,2)} + (\mathbf{P}_{0,j}^{(HL,1,2)})^\top \mathbf{D}_{0,j}^{(HL,1)} \\
&\quad \left. + (\mathbf{P}_{1,j}^{(HL,1,2)})^\top \mathbf{D}_{1,j}^{(HL,1)} \right), \tag{A.18}
\end{aligned}$$

où pour chaque $i \in \{0, 1, 2, 3\}$ et $o \in \{HL, LH, HH\}$,

- $\mathbf{Q}_{i,j}^{(o,2)} = (q_{i,j}^{(o,2)}(s, t))_{(s,t) \in \mathcal{Q}_{i,j}^{(o,2)}}$ est un vecteur de prédiction intra dont le support est désigné par $\mathcal{Q}_{i,j}^{(o,2)}$
- $\mathbf{P}_{i,j}^{(o,1,2)} = (p_{i,j}^{(o,1,2)}(s, t))_{(s,t) \in \mathcal{P}_{i,j}^{(o,1,2)}}$ est le vecteur de prédiction hybride dont le support est noté par $\mathcal{P}_{i,j}^{(o,1,2)}$
- $\tilde{\mathbf{D}}_{0,j+1}^{(o,2)} = (D_{j+1}^{(2)}(x+s, y+t))_{(s,t) \in \mathcal{Q}_{0,j}^{(o,2)}}$ est un vecteur de référence contenant les coefficients d'approximation $D_{j+1}^{(2)}$ utilisés pour calculer les sous-bandes de détails $D_{j+1}^{(o,2)}(x, y)$

- $\tilde{\mathbf{D}}_{1,j+1}^{(HH,2)} = (\tilde{D}_{j+1}^{(HL,2)}(x+s, y+t))_{(s,t) \in \mathcal{Q}_{1,j}^{(HH,2)}}$ et $\tilde{\mathbf{D}}_{2,j+1}^{(HH,2)} = (\tilde{D}_{j+1}^{(LH,2)}(x+s, y+t))_{(s,t) \in \mathcal{Q}_{2,j}^{(HH,2)}}$ sont deux vecteurs de référence, contenant respectivement les coefficients de détail intermédiaires $\tilde{D}_{j+1}^{(HL,2)}$ et $\tilde{D}_{j+1}^{(LH,2)}$, utilisés pour calculer les coefficients de détail finaux $D_{j+1}^{(HH,2)}(x, y)$
- $\underline{\mathbf{D}}_{j+1}^{(HH,2)} = (D_{j+1}^{(HH,2)}(x+s, y+t))_{(s,t) \in \mathcal{Q}_{1,j}^{(LH,2)}}$ et $\overline{\mathbf{D}}_{j+1}^{(HH,2)} = (D_{j+1}^{(HH,2)}(x+s, y+t))_{(s,t) \in \mathcal{Q}_{1,j}^{(HL,2)}}$ sont deux vecteurs de référence contenant les échantillons utilisés pour calculer $D_{j+1}^{(LH,2)}(x, y)$ et $D_{j+1}^{(HL,2)}(x, y)$
- $\mathbf{D}_{i,j}^{(o,1)} = (D_{i,j}^{(1)}(x+s, y+t))_{(s,t) \in \mathcal{P}_{i,j}^{(o,1,2)}}$ est un vecteur de référence contenant des échantillons de l'image de référence $D_j^{(1)}$ afin d'exploiter les corrélations inter-images pendant le calcul des coefficients de détail finaux $D_{j+1}^{(o,2)}(x, y)$.

Enfin, en suivant la même stratégie proposée avec la structure du lifting vectoriel séparable, au lieu de coder la sous-bande approximation de l'image cible $D_J^{(2)}$ au dernier niveau de résolution J , il serait intéressant d'exploiter sa corrélation avec $D_J^{(1)}$, et donc, encoder la sous-bande résiduelle.

Afin de désigner une décomposition en ondelettes bien adaptée au contenu des hologrammes, une importance particulière sera accordée à l'optimisation des différents opérateurs de lifting.

Optimisation des prédicteurs utilisés avec $D^{(1)}$

Pour la première image $D^{(1)}$, les différents filtres prédiction $\mathbf{P}_j^{(o,1)}$ (avec $o \in \{HH, LH, HL\}$), utilisés pour générer les sous-bandes de détails $D_{j+1}^{(o,1)}$, sont optimisés à chaque niveau de résolution j en minimisant la variance des coefficients de détail. Les filtres optimaux vérifient les équations de Yule-Walker.

Optimisation des opérateurs de mise à jour

Le filtre de mise à jour est optimisé à chaque niveau j en minimisant l'erreur entre les coefficients d'approximation $D_{j+1}^{(1)}$ et la version décimée du signal résultant d'un filtrage passe-bas idéal de l'image d'entrée [67].

Optimisation des prédicteurs pour $D^{(2)}$

Comme $D^{(1)}$ et $D^{(2)}$ présentent des contenus similaires, le processus d'optimisation des trois premiers filtres de prédiction $\mathbf{P}_j^{(o,2)}$ et le filtre de mise à jour $\mathbf{U}_j^{(2)}$ peuvent être optimisés en imposant que ces opérateurs soient égaux à ceux obtenus avec $D^{(1)}$.

Ainsi, on a:

$$\begin{aligned}\mathbf{P}_j^{(HH,2)} &= \mathbf{P}_j^{(HH,1)}, \mathbf{P}_j^{(LH,2)} = \mathbf{P}_j^{(LH,1)}, \\ \mathbf{P}_j^{(HL,2)} &= \mathbf{P}_j^{(HL,1)}, \mathbf{U}_j^{(2)} = \mathbf{U}_j^{(1)}.\end{aligned}\tag{A.19}$$

Il est important de noter que cette procédure présente les avantages de simplification la stratégie d'optimisation et de réduire le coût de transmission correspondant aux coefficients du filtre qui doivent être envoyés au décodeur. Enfin, pour les autres filtres de prédiction hybride $\mathbf{P}_j^{(o,1,2)}$ et $\mathbf{Q}_j^{(o,2)}$, ils seront optimisés en minimisant la variance des coefficients de détails $D_{j+1}^{(o,2)}$.

Les résultats expérimentaux obtenus dans cette thèse confirment l'efficacité du schéma de lifting vectoriel non séparable adaptatif pour compression des hologrammes.

A.3.4 Etude de Compression des données holographiques à déphasage à l'aide de schémas de codage vidéo

Nous proposons également d'utiliser deux systèmes de codage vidéo grand public - le codage vidéo avancé et celui à haute efficacité - pour la compression des données holographiques à déphasage. Cette étude préliminaire peut être divisée en deux parties: la comparaison de l'efficacité entre les performances de compression des schémas de codage vidéo sur la séquence d'hologrammes numériques à déphasage générée à partir de séquences d'images 2D et les schémas de codage vidéo sur les informations de distance décalée générée à partir d'une seule image.

La deuxième étude comprend des procédures de génération des séquences d'hologrammes numériques, l'agencement de trames holographique pour former un flux vidéo et sa compression. De même, les séquences d'hologrammes numériques sont également des séquences d'hologrammes générés par ordinateur sur la base de la transformée de Fresnel à partir de trois séquences d'images 2D. Les séquences sont codées et reconstruites pour évaluer la performance des schémas de codage en comparant les reconstructions avec les séquences non compressées.

Le schéma d'ensemble est décrit comme présenté sur la Fig. A.7. Les séquences d'hologrammes numériques sont générées à partir des séquences d'images bitmap. Les modèles sont fournis par une caméra virtuelle qui capte le mouvement des objets virtuels en 3D. Chaque trame 2D donne trois hologrammes numériques par la transformée de Fresnel.

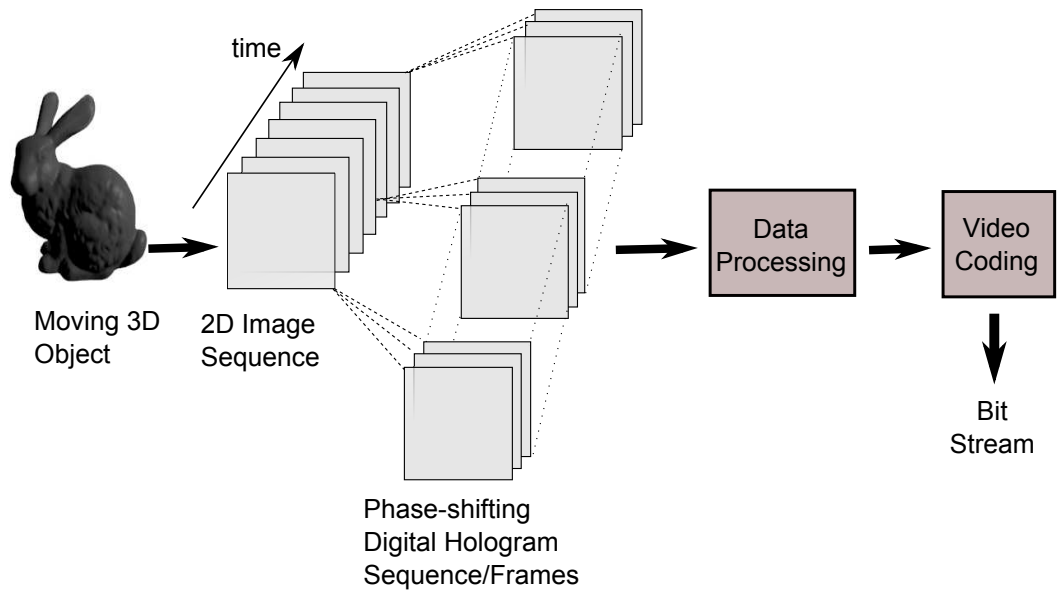


Figure A.7: Over scheme for digital holographic video processing

Normalement, le format YUV est le principal format vidéo brut utilisé dans les logiciels de codage vidéo. En conséquence, avant le codage, les séquences d'hologrammes numériques à déphasage générées doivent être converties au format approprié vidéo YUV pour satisfaire le format d'entrée des logiciels de codage. Après le traitement des séquences d'hologrammes numériques dans le format vidéo approprié, la procédure de codage est effectuée.

Les résultats des expériences numériques de la première étude indiquent que, en comprimant avec le mode inter de AVC et HEVC on peut obtenir de bonnes images de reconstruction avec une bonne qualité, cependant, HEVC surpasse globalement AVC. Dans la seconde étude, les performances du mode inter et intra HEVC sur des données de distance décalés a été étudié. Le mode inter de HEVC surpasse tous les autres régimes. Cependant, les schémas HEVC basés sur une décomposition VLS fonctionnent mieux que l'autre mode intra.

A.4 Conclusion et perspectives

Avec l'intérêt croissant pour l'holographie numérique et l'holographie générée par ordinateur dans de nombreuses applications, cette thèse a été principalement consacrée à concevoir des mécanismes de compression efficaces pour les données holographiques numériques à

déphasage avec une analyse des bases de représentation des différents groupes de données holographiques. Dans la suite, les principaux concepts et contributions de ce travail sont résumées avec quelques extensions futures possibles.

La première contribution est l'analyse de l'algorithme de décalage de phase, une nouvelle représentation de données holographiques à déphasage, appelée information de distance décalée, est introduite. En outre, une classification claire des différentes représentations de données holographique est donnée pour rendre plus compréhensibles les caractéristiques des données. Les représentations d'intensité et amplitude à bases complexes comprennent respectivement des représentations obtenues avant et après l'application de l'algorithme de déphasage. En outre, les motifs dans les différentes représentations de données holographiques à déphasage sont étudiés dans une étude comparative, révélant que plus de motifs existent dans les informations de distance décalée et de l'information réelle-imaginaire que les informations d'amplitude-phase.

La deuxième contribution est que nous proposons une nouvelle décomposition multi-échelle conjointe de données holographiques à déphasage basée sur les VLS. Contrairement aux autres méthodes de l'état de l'art où différentes informations sont encodées séparément, deux ensembles d'information à distance décalée (ou information réelle imaginaire) sont codés conjointement par VLS. Les représentations multi-solution générées de l'information de distance décalée sont plus compactes que celles générées indépendamment. Dans ce contexte, nous avons proposé deux schémas de décomposition sur la base de VLS, un séparable et un non séparable, désignés respectivement SEP-VLS et NS-VLS. Dans SEP-VLS, VLS est effectué d'une manière séparable, en cascade la décomposition 1D le long de la direction horizontale, puis le long de la direction verticale. Toutefois, selon les motifs visuels des données des différences décalées, certaines structures isotropes sont bien présentes. Une décomposition non séparable est donc proposée pour améliorer les performances. Les résultats expérimentaux ont montré la supériorité de la proposition de SEP-VLS et NS-VLS sur les conventionnels, tandis que le NS-VLS est plus adaptatif à nos données en termes de qualité de l'objet 3D reconstruit.

En outre, en raison de la structure particulière de données de distance décalés et l'avantage de VLS qui exploite les motifs inter-images à travers l'étape de prédiction, notre troisième contribution est l'étude de NS-VLS avec différentes longueurs de filtres. Les résultats expérimentaux ont montré des gains significatifs en augmentant la longueur de filtre en matière d'économie débit et de qualité visuelle de la reconstruction. Enfin, afin

d'étudier l'efficacité des schémas de codage vidéo grand public, une étude préliminaire de compression de données holographique numérique à déphasage est fournie par l'application d'AVC et HEVC. La quatrième contribution est divisée en deux parties. Tout d'abord, les séquences d'hologramme déphasage générés par des séquences d'images 2D sont comprimées par mode inter d'AVC et HEVC. La meilleure performance de HEVC a été vérifiée. Deuxièmement, l'effet de la taille TU utilisée dans HEVC est étudiée sur des informations de distance décalée générée par une image. Il se trouve que plus la taille TU est grande, plus elle donne des bonnes performances. En outre, l'application HEVC, après une décomposition VLS séparables, améliore encore les performances, ce qui démontre l'efficacité de l'application de VLS sur les données de distance décalés.

Cependant, notre travail a des limites qui devraient être abordées dans les travaux futurs. Tout d'abord, pendant toute la thèse, des objets 2D d'image sont sélectionnés pour la simplicité de génération des hologrammes. Deuxièmement, contrairement à d'autres techniques 3D, de la partie d'enregistrement à la partie de l'affichage, il y a encore des verrous technologiques à surmonter pour l'holographie numérique. Par conséquent, la recherche sur la compression de données holographiques numériques est également un tout nouveau domaine. Les discussions sur les travaux futurs peuvent être divisées en quatre parties traitant des principales préoccupations dans notre travail.

Tout d'abord, la cible de compression devrait être améliorée. Il y a deux préoccupations principales: (1) les hologrammes d'objets du monde réel peuvent avoir une apparence différente de ceux générés par ordinateur parce que le système d'enregistrement du monde réel est plus complexe, et (2) des modèles d'objets complexes peuvent aussi entraîner différents modèles d'interférence par exemple, le nombre d'objets et leur emplacement. Donc, nos contributions doivent être confirmées soit sur hologrammes enregistrés physiquement ou CGHS avec des modèles d'objets plus complexes. Pour les modèles de calcul pour CGHS, jusqu'ici, nous avons essayé la méthode de traçage par rayon utilisant la dispersion des objets ponctuels et la transformée de Fresnel utilisant des images "bitmap". Afin d'obtenir des hologrammes plus précis contenant profondeur, texture, de l'ombre et de l'angle suffisamment d'informations, d'autres modèles d'objets plus complexes, tels que des objets maillés, pourraient être testés avec quelques algorithmes accélérés.

Deuxièmement, afin de comparer avec certaines méthodes mentionnées dans l'état de l'art, telles que l'application de Fresnelets et ondelettes de Gabor, notre méthode proposée basée sur VLS peut également être étendue au plan de reconstruction. Actuellement, notre

méthode s'applique au plan de compression de la caméra. Son avantage est que le codage est effectué pixel par pixel, et donc l'erreur introduite est minimale contrairement aux méthodes à base de transformation qui induisent généralement de la distorsion. Cependant, comme il y a plus d'informations sur la structure dans le plan de reconstruction dans l'holographie numérique à déphasage, il est attendu un accroissement de l'efficacité de la compression inter. Par conséquent, il devrait être prometteur d'appliquer des régimes inter de compression sur le front d'onde complexe dans le plan de reconstruction. Il serait également intéressant d'étendre l'approche proposée pour le cadre numérique de codage vidéo holographique.

En troisième lieu, on a constaté que la longueur de filtre de l'opérateur de prédiction à VLS et la taille TU peuvent avoir un impact significatif sur l'efficacité de la compression, des procédés pour optimiser la longueur du filtre ou la taille TU devraient être étudiés pour s'adapter à des hologrammes enregistrés différemment.

Enfin, des mesures plus appropriées pour l'évaluation de la qualité pourraient être étudiés. Actuellement, les mesures NRMS et PSNR appliquées sur les hologrammes compressés et les hologrammes originaux sont couramment utilisés pour des hologrammes enregistrés physiquement. Cependant, ces deux paramètres ne prédisent pas toujours la qualité visuelle des objets reconstruits. Dans notre travail, nous avons constaté certaines limites lors de l'application SSIM. Par exemple, parfois à très faible débit binaire, la tendance de la métrique SSIM est contraire à la modification de la qualité visuelle avec l'augmentation du débit. En conclusion, le problème de l'évaluation de la qualité dans le contexte de la compression de l'hologramme reste encore une question ouverte.